

**ENERGETICS
OF THE
AU(110)-SURFACE:**

**ONE REASON
FOR MANY
STRUCTURES**

PROEFSCHRIFT

ter verkrijging van
de graad van Doctor aan de Universiteit Leiden,
op gezag van de Rector Magnificus Dr. D.D. Breimer,
hoogleraar in de faculteit der Wiskunde en
Natuurwetenschappen en die der Geneeskunde,
volgens besluit van het College voor Promoties
te verdedigen op donderdag 15 november 2001
te klokke 14.15 uur

door

Marcel Joachim Rost

geboren te Garmisch-Partenkirchen in 1968

Promotiecommissie

Promotor: Prof. dr. J. W. M. Frenken
Referent: Prof. dr. J. M. van Ruitenbeek
Overige leden: Priv. Doz. Dr. Th. Michely (RWTH Aachen, Germany)
Prof. dr. ir. B. Poelsema (Universiteit Twente)
Prof. dr. E. Vlieg (Katholieke Universiteit Nijmegen)
Prof. dr. H. van Beijeren (Universiteit Utrecht)
Prof. dr. A. W. Kleyn
Prof. dr. P. H. Kes

ISBN: 90-77017-22-4

Graphical design: Marcel J. Rost

Printed by: Optima Grafische Communicatie, Rotterdam

The work described in this thesis was performed at the
Kamerlingh Onnes Laboratorium
Universiteit Leiden, Niels Bohrweg 2, 2333 CA Leiden
and at the
FOM Institute for Atomic and Molecular Physics
Kruislaan 407, 1098 SJ Amsterdam

The work is part of the research program of the
'Stichting voor Fundamenteel Onderzoek der Materie' (FOM)
and was made possible by financial support from the
'Nederlandse Organisatie voor Wetenschappelijk Onderzoek' (NWO).

Cover image created using the original microscopy data of four STM images, all obtained on Au(110): 'almonds' (top), 'crossing sites' in a step network (right), a 'termination site' (left), and various vacancy island structures (bottom).

This thesis is based on the following articles:

Chapter 3:

* *Anomalous shape and decay of islands on Au(110)*

M.J. Rost, R. van Gastel, J.W.M. Frenken; Phys. Rev. Lett. **84**, 1966 (2000)

Chapter 4 & 7:

Asymmetric and symmetric Wulff constructions of island shapes on a missing-row-reconstructed surface

S.B. van Albada, M.J. Rost, J.W.M. Frenken; Phys. Rev. B, submitted

Chapter 5:

Comment on Real space investigation of the roughening and deconstruction transition of Au(110)

M.J. Rost, J.W.M. Frenken; Phys. Rev. Lett. **87**, 039603 (2001)

* *Real space investigation of domain boundary formation on Au(110)*

M.J. Rost, S.B. van Albada, J.W.M. Frenken; Phys. Rev. Lett., submitted

Chapter 6 & 8:

* *How asymmetric islands become symmetric*

M.J. Rost, S.B. van Albada, J.W.M. Frenken; Phys. Rev. Lett. **86**, 5938 (2001)

* a more detailed publication is in preparation

Other publications:

Grain growth in a polycrystalline gold film observed in situ with STM

M.J. Rost, D. Quist, J.W.M. Frenken; in preparation

An STM study of the incorporation of a surfactant: indium on Cu(001)

R. van Gastel, M.F. Roşu, M.J. Rost, L. Niesen, J.W.M. Frenken; in preparation

Dynamiek in een oppervlak

K. Schoots, M.J. Rost, S.B. van Albada, J.W.M. Frenken; *Novacblad* **39**, 59 (2001)

Plug 'n' play scanning probe microscopy

Th. Michely, M. Kaiser, M.J. Rost; *Rev. Sci. Instr.* **71** (12), 4461 (2000)

Mikromanipulator, patent 199 35 570.3 Forschungszentrum Jülich

Th. Michely, M.J. Rost, M. Kaiser; (1999)

Comment on Self-diffusion and dynamic behaviour of atoms at step edges on iridium surfaces

M.J. Rost, Th. Michely, G. Comsa; *Phys. Rev. B* **57**, 1992 (1998)

'The book of Nature is written in Mathematics'

Charles Darwin

Contents

Introduction	7
1 Experimental Setup	9
1.1 Introduction: Scanning Tunnelling Microscope	10
1.2 Present Setup	12
1.2.1 Control Electronics	14
1.3 Design of a new STM	15
1.4 Design of a new UHV-Chamber	18
2 General Background	25
2.1 Terrace-Ledge-Kink Model of Crystal Surfaces	26
2.2 Free Energy: the Role of Entropy	27
2.3 Equilibrium Shape: Wulff Construction	27
2.4 Phase Transitions	29
2.5 Step-Step-Interactions	30
2.6 Surface Diffusion	31
2.7 Coalescence and Ostwald Ripening	32
2.8 Au(110)-Surface	35
2.8.1 Reconstructions	38
2.8.2 Phase Transitions	38
2.8.3 Diffusion on Au(110)	39
2.8.4 Au(110) in Numbers	40
3 Symmetric ‘Almonds’	41
3.1 Equilibrium Shapes with Sharp Corners	42
3.1.1 Observation	42
3.1.2 Termination and Crossing Sites	43
3.1.3 Determination of Absolute Step Energy Values	46
3.2 Dynamics of the Islands and the Networks	52
3.2.1 Network Structure Effects	53
3.2.2 Shape Change	54

3.2.3	Scaling Behaviour of the Island Decay	56
3.3	Summary and Discussion	58
4	Theory for the Symmetric Almonds	61
4.1	Step Free Energy	62
4.1.1	From a Square Lattice to a Rectangular Lattice	62
4.1.2	Energetics of a Missing-Row Surface	63
4.1.3	Separating Energy Contributions from Ground State and Fluctuations	64
4.1.4	Two-Dimensional Ising Model	66
4.1.5	Perpendicular Fluctuation Approximation	67
4.1.6	Parallel Fluctuation Approximation	68
4.2	Equilibrium Island Shape	69
4.2.1	Cusps in the Free Energy Plots	73
4.2.2	Temperature Dependence of the Wulff Construction	73
4.3	Summary	75
	Appendix: Monte Carlo simulation	76
5	Domain Boundaries	77
5.1	Introduction	78
5.2	Observation	79
5.3	Domain Boundaries at Termination Sites	80
5.4	Domain Boundaries at Crossing Sites	82
5.4.1	Simple Boltzmann Distribution	82
5.4.2	Including the Free Energy Change of the Step Network	84
5.4.3	Including also Elastic Step-Step-Interactions	85
5.4.4	Overview of the Three Models	89
5.5	Why only Hollow Walls at Termination Sites?	90
5.6	Result and Consequences	91
5.7	Summary	94
6	(A)symmetric ‘Cigars’	95
6.1	Vacancy Islands with Broken Mirror Symmetry	96
6.2	Asymmetric Equilibrium Shape?	97
6.2.1	Asymmetry due to Difference in Step Energies?	97
6.2.2	Asymmetry due to Difference in Kink Energies?	98
6.3	Determination of the Kink Energies	98
6.4	Summary: Symmetric Averaged Island Shape!	102
6.5	Outlook	102

7	Theory for the (A)symmetric ‘Cigars’	103
7.1	Symmetric Contour of the Asymmetric Islands	104
7.2	Step Free Energy of Asymmetric Islands	107
7.2.1	Two-Dimensional Ising Model	108
7.2.2	Perpendicular Fluctuation Approximation	109
7.2.3	Parallel Fluctuation Approximation	109
7.3	Temperature Dependence of Asymmetric Islands	110
7.4	Summary	110
7.5	Relation between Asymmetric and Symmetric Islands	112
8	Evolution of the (A)symmetric ‘Cigars’	113
8.1	Observations	114
8.2	Microscopic Mechanisms and Resulting Time Scales	116
8.2.1	Normal Coalescence	116
8.2.2	Slow Coalescence	117
8.3	Bound-Pair Formation	120
8.4	‘Bound Line Pairs’	121
8.4.1	Length Constraints on the ‘Bound Line Pairs’	125
8.5	One-Dimensional Diffusion	127
8.6	Summary	129
	Appendix A: Sample Preparation and Tunneling Conditions	131
	Summary	133
	Samenvatting voor de leek	137
	Nawoord	139
	Curriculum Vitae	140

Introduction

Since ancient times, people are fascinated by the shapes of crystals, such as natural gemstones and frost patterns. One of the beauties of crystals lies in the regularity of their appearance, with flat facets, straight edges, and sharp corners. Due to its ability to observe surface structures down to the atomic scale, the ‘scanning tunnelling microscope’ (STM) has renewed this fascination, by enabling observations of two-dimensional crystal shapes of adatom and vacancy islands on single-crystal surfaces.

Usually, the equilibrium shapes of three- or two-dimensional crystal structures are the same on both small and large length scales. The shapes are determined by the energetics of the surfaces or the steps that form the 3- or 2-D crystal’s contour.

This thesis describes a variety of different types of island and step structures that, surprisingly, all appear on the same surface: Au(110). A detailed understanding of this variety is reached by studying the atomic-scale energetics of these structures.

The Au(110)-surface is expected to undergo two different phase transitions at elevated temperatures. In the ‘deconstruction transition’, the order of the so-called ‘missing-row’ structure of Au(110) is gradually lost. In the ‘roughening transition’ the long-range flatness of the surface is destroyed. Attempts to observe these transitions directly in real space with an intrinsically slow instrument, such as the STM, have been unsuccessful, due to the high atomic mobility on Au(110) at the temperatures of interest. In this thesis, we follow an alternative approach.

By combining the formation energies of steps, kinks, and other relevant structures, which we obtain from our STM measurements, with appropriate theories, we calculate the transition temperatures, and predict that the Au(110)-surface indeed undergoes two separate phase transitions. The predicted transition temperatures are in reasonable agreement with those observed in other experiments. In our STM-images, we find evidence for an atomic-scale structure, which is involved in the onset of the deconstruction transition.

An important additional conclusion from our study is that the appearance of symmetrically shaped crystals does not necessarily imply a symmetric underlying structure. This stands in contrast to usual observations, where the symmetry of the internal structure is reflected in the crystal shape.

This thesis is organised as follows. Chapter 1 describes several improvements that have been designed for the STM setup. Although they have not yet been used in the

experiments described in this thesis, they are expected to greatly improve the imaging quality, versatility, and ease of use of the instrument. In chapter 2 an overview is provided of the surface energetics, diffusion dynamics, phase transitions, and the specific details of interest of the Au(110)-surface, which form the subject of the STM observations. Chapters 3, 5, 6, and 8 describe the results of STM experiments on Au(110). The experimental findings are complemented by theoretical descriptions of the two-dimensional island structures on this surface, which form the subject of chapters 4 and 7.

Together, the experimental and theoretical results, presented in this thesis, provide a close to complete picture of the atomic-scale energetics of Au(110).

Chapter 1

Experimental Setup

This chapter describes the technique and instrumentation used for the experiments in this thesis, and introduces the construction of the most important modifications and additions made to the equipment. Firstly, a short introduction to scanning tunnelling microscopes (STMs) is given, using the example of a so-called 'Beetle'-STM. This is followed by the description of the Leiden-STM, and the improvements which were necessary for the experiments of this thesis. The Leiden-STM and the 'Beetle' each have their own advantages and disadvantages. A new microscope is under development that combines the advantages of both types in one design. This project is still in the construction and testing phase and only the working principle and first test results are reported. In addition, a new ultrahigh vacuum system is under construction. In comparison with the existing set-up, it allows new types of measurements, under a wider range of conditions, at lower pressures, in the low 10^{-11} mbar regime, and with better vibration isolation.

1.1 Introduction: Scanning Tunnelling Microscope

Inspired by the pioneering work by Young et. al. [1] on scanning probe microscopy, the scanning tunnelling microscope (STM) was invented by Binnig and Rohrer in 1981 [2, 3]. This instrument has revolutionised surface science research. The STM has made it possible to observe surfaces in real space with atomic resolution. A good introduction to scanning tunnelling microscopy can be found in [4].

The operation of this type of microscope is explained via the specific example of a so-called ‘Beetle’-STM [5, 6] (see fig. 1.1), which consists of three main parts:

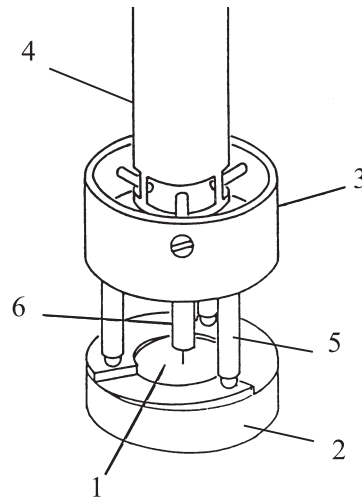


Figure 1.1: *Scheme of a Beetle-STM (reprinted [7]): (1) sample; (2) sample holder with three ramps; (3) scanner body; (4) mount; (5) piezo-tube leg; (6) z-piezo-tube.*

the sample (1), the sample-holder (2) and the scanning unit or scanner (3) with its mount (4). The sample is clamped in the sample holder, which also supports the scanner. The scanner consists of a body and four piezo-tubes: three of these are used as legs (5) and the fourth, central tube (6) is used to hold the STM-tip. The outer electrodes of the piezo-tubes are all segmented in four sections. When a voltage is applied to these segments, the tubes can be changed in length (z-direction) and bent in any lateral direction (x, y).

The principle of the STM is based on the quantum-mechanical tunnelling effect of electrons between two conductors in very close physical proximity; here, these are the imaging sensor (tip) and the sample. Usually, one uses a sharp, wet-etched tungsten tip. A sensitive measure for the distance between the tip and the sample is the tunnelling current that flows, if a voltage is applied between them. Typical values are 1 nA current at a voltage of 0.2 V at a short distance of ~ 8 Å. The tunnelling current depends exponentially on the distance.

When recording a topographical surface image, the tip is moved by the central piezo-tube along the horizontal x- and y-directions, building up the image line by line. Imaging is usually carried out in constant-current mode, i.e., the tip height is continually adjusted in order to keep the tunnelling current constant at a given, fixed tunnelling voltage. This forces the tip to follow the height contour of the surface at a constant distance. If the tip is sharp and one atom at the end sticks out further than the rest, it is possible to image the atomic corrugation of a sample.

Since the total length variation of the piezo-legs is limited ($< 1\mu\text{m}$), an additional mechanism is needed to bring the tip-sample distance into the piezo range. The three piezo legs are used for the coarse approach mechanism that allows the tunnelling regime to be reached without the tip crashing into the surface. For such an approach, the scanner is initially set with its legs at the highest positions on the three ramps, as shown in fig. 1.1. First, all three legs are slowly bent counterclockwise, tangentially to the circle of the scanner. This results in a clockwise rotation of the scanner body, which remains in this new position, when the tubes are forced straight very quickly. The repetition of this *slip-stick* motion makes the scanner *walk* down (or up) the ramps and smoothly reach (or leave) the tunnelling regime. On the basis of the same principle, it is also possible to move the scanner along the x- and y-directions, e.g., to find or track a particular point of interest on the surface.

A feedback-electronics system, with adjustable proportional and integral gains, controls the height of the tip and is used to keep the tip-surface distance constant. It converts the detected difference between the requested and the actual tunnelling current into a voltage that is returned to the z-piezo element after amplification. Obviously, the design and quality of this electronics determines to a large extent the performance of the STM: currents in the nA-range have to be amplified and converted into low-noise voltages in the $\pm 200\text{V}$ range, at a high bandwidth.

Another crucial aspect of the instrument is the mechanical loop between the tip and the sample. Any mechanical vibration that couples into this loop shows up in the tunnelling current and usually prevents atomic resolution. Recently, on the basis of this coupling, an apparatus has been designed [8] that measures very small-amplitude vibrations of resonating objects. But for STM purposes, vibrations should be avoided, and mechanical low-pass filters are usually used to decouple the STM from the surrounding background vibrations. In addition, the ‘ideal’ STM is designed such that it has the highest possible resonance frequencies. This makes the STM relatively insensitive to external vibrations and it allows high speed measurements without the introduction of vibrations by the movement of the scan-piezo itself, especially at each turning point at the end of a scan line. The following length comparison illustrates the difficult task of the STM: obtaining atomic resolution with the STM sensor (piezo-tube including the tip) is equivalent to the task of measuring (height and lateral variations) of micrometers with the Eiffel-tower turned upside down.

1.2 Present Setup

The STM setup, used for all experiments in this thesis, is a home-built microscope, developed by Kuipers et al. [9] and further improved by Hoogeman et al. [10]. In the design of this STM, great care was taken to optimise two properties: thermal stability and speed. Figure 1.2 shows a cross section of the scanner, the sample holder and the support block. The scanner (1) is built on the basis of the thermal-drift compensated

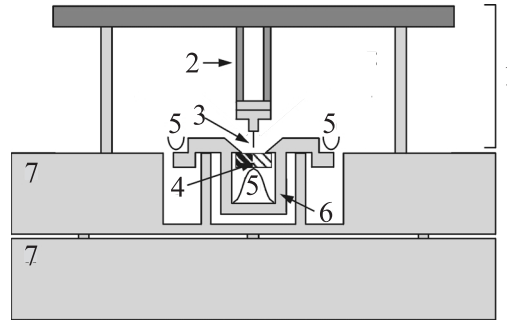


Figure 1.2: Scheme of the present STM: (1) scanner; (2) piezo-tube; (3) tip; (4) sample; (5) leaf springs; (6) sample-holder; (7) support block (reprinted with permission [10]).

design of Kuipers et al. [9], who used finite-element calculations to match the vertical thermal expansion of the legs with that of the assembly of the piezo-tube (2), the tip holder and the tip (3). As the scanner stands on the support block, the upper surface of this block simultaneously serves as a reference plane. At any temperature, the end of the tip remains precisely located in this reference plane. In addition, the calculations had been used to match the horizontal thermal expansion of the scanner with that of the support block (7), thus reducing the lateral drift of the scanner to very low values.

The sample (4) is clamped by a leaf spring (5) against two ledges of the sample-holder (6) (see fig. 1.2). The sample holder has two arms, with which it rests on its support. The design is such that the sample surface, the ledges and the arms all lie in the reference plane, defined above as the surface of the support block. This ensures that the sample surface is held in this plane, whatever the material and thickness of the sample, and whatever the temperature of the sample and its holder. Thanks to a similar type of configuration of the sample holder and its support in the horizontal plane, the lateral drift of the sample is minimised, too.

The combination of the thermally compensated scanner and the drift-compensated sample holder makes this microscope extremely insensitive to temperature variation compared with other STMs. With hardly any drift in the z -direction and very low lateral drift, this microscope makes it possible to image a selected atomic location on a surface *during* a temperature change of more than 270 K. For comparison, if the temperature is changed by ~ 50 K during imaging, traditional STMs either crash the

tip into the surface, or drift out of tunnelling range, which makes *in-situ* temperature-variation experiments very difficult for such instruments.

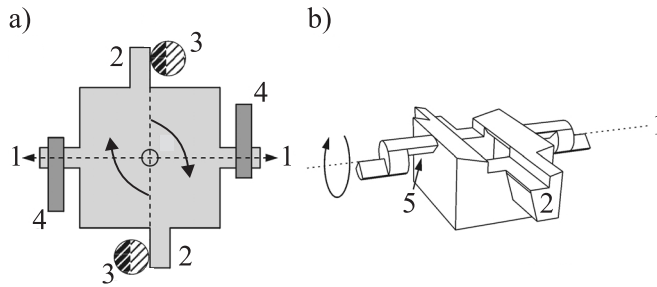


Figure 1.3: Scheme of the sample-holder body: (1) axis of rotation; (2) arm; (3) post; (4) leaf spring; (5) knife edge (reprinted with permission [10]).

In order to bring the tip into tunnelling range, the drift-compensated STM required a special approach mechanism. The solution was found in a rotation of the sample-holder body around axis (1) in fig. 1.3. The tip is positioned about 1 mm from this rotation axis. If the body is fully rotated, so that the distance between the tip and the sample is at its maximum, the scanner can be placed on the support block without the risk of a tip crash. The tunnelling distance range can be reached by rotating the holder through small rotation steps, by means of a piezo-motor. When the sample holder is pushed down into the STM position, it makes an additional clockwise rotation (indicated by the curled arrows in fig. 1.3a) until its two arms (2) make contact with posts (3) of the support block; this ensures a defined position at any angle of the above described vertical rotation. The sample holder is clamped down by leaf springs (4), so that it rests on its knife edges (5), which define the rotation axis (1).

A major disadvantage of this approach mechanism is that only a small part of the whole sample can be imaged. Scanner displacements are allowed only parallel to the rotation axis. In contrast with the Beetle-STM, a point of interest on the surface cannot be chosen freely, nor can it be followed after it has drifted out of the maximum scan range.

For small images of 100 times 100 pixels, the STM is capable of measuring at an image rate of 5 Hz. One reason for this high rate is the STM's mechanical stability: the solid legs are made of molybdenum. It has been shown that the low resonance frequencies of the Beetle-scanner [11, 12] are an effect of the piezo-tube legs, whose resonance frequencies are lowered dramatically even by small mass loads [11]. A second reason for the high-speed is the very fast data acquisition and control electronics of the STM. Two tunnelling current pre-amplifiers are available: one with a bandwidth of 100 kHz, and the other with a bandwidth that can be switched optically between 1 kHz and 40 kHz.

1.2.1 Control Electronics

The original electronics were optimised for high-speed imaging. To reach maximum bandwidth, only linear amplifiers were used in the original feedback electronics. This allowed fast measurements on relatively smooth surfaces [13], but also introduced the disadvantage that it was very difficult, and sometimes even impossible, to image surfaces with large height variations, or to image under ‘noisy’ tunnelling conditions, e.g. as a result of the presence of (mobile) adsorbates.

The problem was in the gain characteristics of the feedback electronics. Fast measurements and good resolution (sharp images) require the gain to be set high. If the gain is too high, the lowest mechanical resonance frequency is amplified, and the system becomes unstable. The ‘ideal’ gain is a little lower than that at which the STM resonates. With linear amplifiers, the total loop gain depends on the distance between the tip and the surface, because the tunnelling current is exponentially dependent on this distance. This means that the gain increases exponentially, whilst the error in height increases only linearly, if the tip is moved towards the surface. If the STM is confronted with a sudden increase in height, the gain increases dramatically and the system overreacts with a strong retraction¹. This may lead to an overshoot, with the tip retracting too much. When this happens, the tunnelling current is too low and the gain is much reduced. This results in a very slow reapproach of the proper height. In this way, very rough surfaces and adsorbates caused instabilities of the linear electronics. On such surfaces, the tip was frequently launched away from the surface, after which it needed a long time to recover. This resulted in very *sparky* images with poor resolution.

The solution to this problem is to use an operational amplifier with a logarithmic characteristic. This makes the gain independent of the error in the distance. The response time of the feedback-electronics is equal for approaching and retracting corrections, leading to more stable tunnelling without ‘spikes’. In addition, the gain can easily be maximised to a value just below resonance. But, as a disadvantage, we forfeit speed, because the bandwidth of a logarithmic amplifier is narrower than that of a comparable linear one. The bandwidth dramatically decreases the more decades are needed and the higher the amplification. The output of the pre-amplifier is 1 V/nA with a maximum of $\pm 10 \text{ V}$. Allowing for the amplification of currents as small as 1 pA , we need a dynamic range of 4 decades. With the logarithmic amplifier Log100 from *Burr Brown* we still obtain an average bandwidth of $\sim 20 \text{ kHz}$, albeit with a lower bandwidth for lower currents. After this modification, extremely rough surfaces were easily imaged.

In addition, in order to display even very rough surfaces with atomic step resolution, the measurement software was modified to show the height derivative rather than the height itself.

¹The amplification can also become so large that the system is transiently set into resonance.

The measurements in chapter 3 would have been impossible without both modifications.

1.3 Design of a new STM

As already mentioned in section 1.2, the Leiden high-speed, variable-temperature STM has one major disadvantage with respect to a 'Beetle'-STM. The present approach system limits not only the total imaging area of the sample but prevents also the free tracking of a selected part of the surface, which drifts out of the maximum scan range. We summarise the advantages of both types of STM. The molybdenum legs make the Leiden-STM more stable, because the resonance frequencies are higher than those of the Beetle-STM [11]. The thermal drift compensation of the Leiden-STM allows a temperature sweep of more than 270 K *during* imaging of a selected region on the surface. In addition, the design is such that both the sample and the scanner can be introduced/removed via a load-lock system to/from the UHV-chamber, without breaking the vacuum. Due to its mount, this is very difficult with the 'Beetle'-STM. On the other hand, the great advantage of the Beetle-STM is that it can *walk* by itself to reach or track any region on the surface. Is it possible to combine all these advantages in one design?

The solution is given by a new positioning and approach mechanism for the Leiden-STM, which enables the movement of the scanner in all directions. This mechanism combines three Beetle-like ramps and a piezo-motor, which is similar to that of the piezoelectrically driven rotary stage, described in [14]. The idea is to position the scanner by pushing against its legs with a thin metal or quartz ring. For this purpose, the scanner legs run through holes in the ring and rest on the three parts of the support block, which now serve as three Beetle-like ramps.

Figure 1.4 shows a schematic topview of the support block (1), the ring (2) with its holes (3), the ramps (4), the piezo-motor units (5) and the sample holder containing the sample (6). In order to maintain the thermal stability and to ensure the compatibility between the *old* and this *new* STM, the sample holder and its support were kept exactly the same as described above. The only change was that posts were added from below to limit the rotation of the sample holder and keep the surface more or less horizontal. Each of the thread-like formed ramps spans an angle of 105 degrees and a height change of 0.74 mm. The height in the middle of the ramp, at 52.5 degrees, lies exactly in the plane of the surface. This still acts as the reference plane, as described above. Without any changes having been made to the scanner, the sample holder and its support, the thermal stability is expected to equal that of the original design. In one respect we expect a noticeable improvement in the lateral drift performance, when we use the x-, y-positioning capabilities of the new system to place the tip precisely above the location on the sample surface, which remains stationary during temperature changes. The residual lateral drift in the old STM, 169

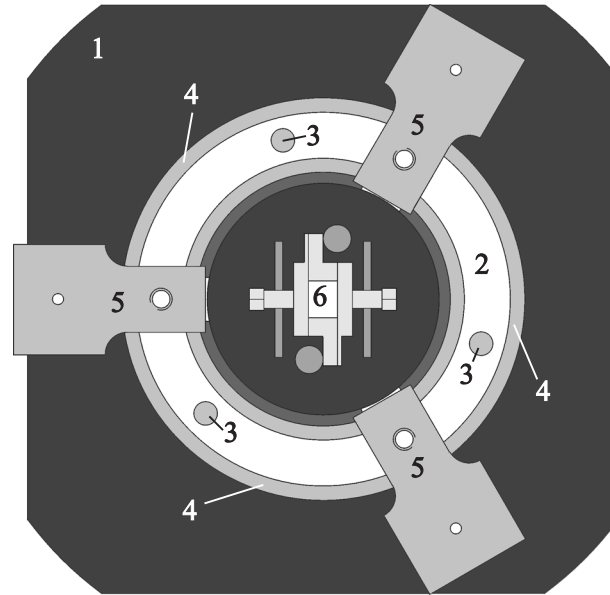


Figure 1.4: Schematic topview of the new positioning system: (1) support block; (2) bronze ring; (3) hole for scanner leg; (4) ramp; (5) piezo motor unit (6) sample holder containing the sample.

Å/K for samples with a high expansion coefficient [10], stems from the difference in expansion between the sample and its holder over the distance between the clamping points and the tip location.

Figure 1.5 shows a cross section of the STM with the new positioning system. The key elements in the piezo motors are piezo elements, flexure hinges and adjustment screws. The working range of the decoupling piezos and the preload of the flexure hinges can be adjusted by screws. The three motors are mounted on the support block, which contains also the three ramps. The surface of one ramp that supports the scanner is indicated in the figure. The working principle is that the *closed* flexure hinge exerts a sufficiently high force on the contacts between the ball segments and the ring, to allow the ring to push the scanner sideways without slipping of the ball-ring contacts. In that case the scanner can be translated in a single step over the lateral range of the (shear) piezo stacks. After this displacement, the decoupling piezo *opens* the flexure hinge, and the ring rests on the lower piezo stack. A fast backwards motion of the stacks results in slip: the ring stays in place, because of its inertia. After this, the flexure hinge is closed again, and the process can be repeated. This results in a step-wise controlled displacement of the scanner. The flexure hinge has been designed with a spring constant of $k = 3.2$ N/degree. The setpoint was chosen such that each *closed* flexure hinge exerts a force of 3.3 N to the contacts of the balls and the ring. This ensures, under the assumption of a friction coefficient of 1

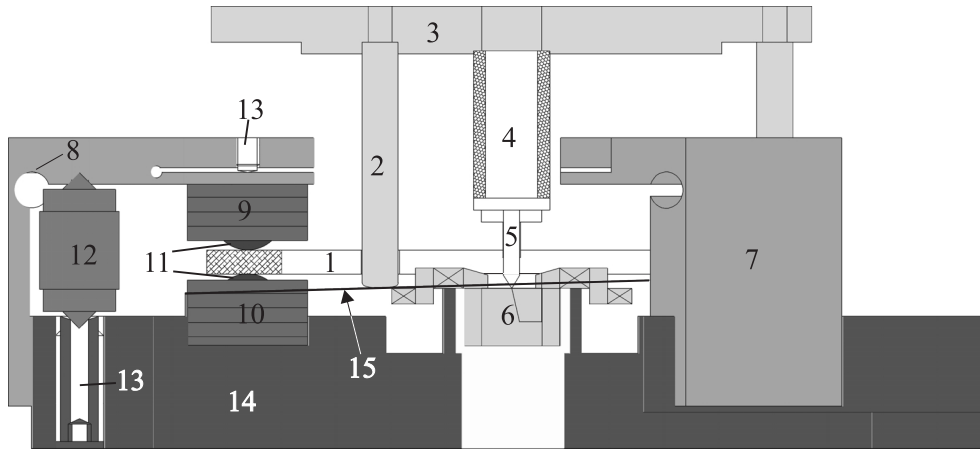


Figure 1.5: STM with new positioning system in cross section (right-hand part in side view): (1) bronze ring; (2) scanner leg; (3) scanner body; (4) scan piezo; (5) tip; (6) sample holder (7) piezo motor unit (side view); (8) flexure hinge; (9) upper piezo stack; (10) lower piezo stack; (11) sapphire ball segment; (12) decoupling piezo; (13) adjustment screw; (14) support block and (15) contour of one ramp.

for both the ball-ring and the leg-ramp contacts, firstly, that a scanner of ~ 1 kg still can be moved, and secondly that the decoupling piezos (with a spring constant of $20 \text{ N}/\mu\text{m}$) extend by 99.9 % of their full range. This corresponds to a maximum opening of the flexure hinge by $11.5 \mu\text{m}$ at the position of the ball-ring contacts.

For the decoupling piezo we have chosen the P249.10 of PI-Ceramics. The piezo stacks are home-built and each stack consists of 3 shear piezos: one for the x-movement, one for the y-movement and one for a tangential movement (rotation). This allows full displacement control: the scanner cannot only be rotated for approach or retracting of the tip, but also be moved along any horizontal direction.

The procedure to reach the tunnelling regime is as follows. Initially, the tip is fully retracted. The scanner is rotated over one or a few rotation steps and the scan piezo is elongated to check whether the tip can be brought into tunnelling range. Then, if the distance between the sample and the tip is still too large, the scan piezo is retracted and the whole process is repeated. Great care was taken in machining the ramps, since the successful operation of the approach crucially depends on their flatness. To prevent a tip crash during approach, the average flatness of the ramps has to be better than $1.2 \mu\text{m}$, since this is the maximum length variation of the scan piezo in z-direction.

The first tests of the assembled positioning system showed that the motor worked and moved the scanner. However, over time, the ring was damaged by the hammering, which was caused by the *opening* and *closing* of the flexure hinges. This led to failure of the setup. In a second round of tests, the system was operated completely

without opening and closing of the flexure hinges. The adjustment screws were set such that the ball-ring contacts were under a preload of 0.8 N. Under these conditions, the motor could easily translate and rotate the 90 g scanner, and the ring was no longer damaged. We have found the motor to be very robust. It operates for various waveforms, e.g. saw tooth and parabolic, at a wide range of frequencies, e.g. 400 Hz, and is rather insensitive to changes in the preload settings of the ball-ring contacts. The step size is reduced by only a modest fraction of typically 15% when the scanner is added to the freely running motor, and also the mass of the scanner is not critical. At 400 Hz, the scanner *walks* down 45° degrees of the ramp within 3 min. This allows not only a short time for approaching the tunnelling regime (about 5 min), but also ensures that the approach takes place without a tip crash, since the average height change per rotational step is only ~ 5 nm.

Once the tunnelling regime is reached, it is possible to decouple the ring from the scanner by a backwards motion of the ring. The holes in the ring are 0.2 mm larger in diameter than the legs, which have a diameter of 3.0 mm.

In a future design, we intend to operate the motor in both possible modes: the ‘coupling/decoupling’ and the ‘constant preload’ mode. For this, we need to overcome the problem of damaging of the ring, e.g. by surface hardening. We expect the ‘coupling/decoupling’ mode to result in higher forces, which may be useful if the motor would get stuck during ‘constant preload’ operation in vacuum.

1.4 Design of a new UHV-Chamber

There were two reasons for designing a new UHV-chamber: firstly to fit the larger size of the new generation STM, which will include also an eddy-current damping stageⁱⁱ, and secondly to add new capabilities with respect to the present setup, extending the range of possible experiments.

For the eddy-current damping, the support block is mounted on a plateau that is suspended on four springs. The spring constant is chosen such that the system has a resonance frequency of 1.5 Hz. The eddy-current damping is attached to this plateau. The present setup allows cooling of the sample to 40 K only at the STM position, where a copper claw that is thermally connected to a He-cryostat can be clamped around the support block. This claw has to be disconnected when the sample is moved to other positions, such as LEED, AES and sputter cleaning. As a consequence, the range of possible experiments is limited, e.g. structures cannot be observed that are only stable at low temperature and have to be created by ion bombardement. The new design is equipped with a permanent coupling of the sample-holder block to a cryostat. This allows a controlled temperature (as low as 20 K) of the sample at all available positions in the chamber. The ion gun used for sputter cleaning in the present setup requires the flooding of the whole chamber with the sputter gas (Ar,

ⁱⁱThis makes it too large for the old STM chamber.

Kr,..). The new chamber is equipped with a differentially pumped sputter gun, thus reducing the gas load in the UHV-chamber during sputtering. Like the old setup, also the new setup allows the transfer of samples as well as scanners into and out of the chamber without breaking the vacuum. In the design of the new chamber and the selection of pumps (see list at the end of this section), extra attention has been given to the vacuum. The system is expected to reach an operating pressure in the low 10^{-11} mbar range and a base pressure of $1 \cdot 10^{-11}$ or lower.

Figure 1.6 shows the ‘new’ vacuum chamber (1), which is coupled via a transfer chamber (2) to the ‘old’ chamber (3). In this way samples can be cleaned and inspected with the ‘old’ STM in the ‘old’ chamber, while actual STM measurements take place primarily in the new chamber.

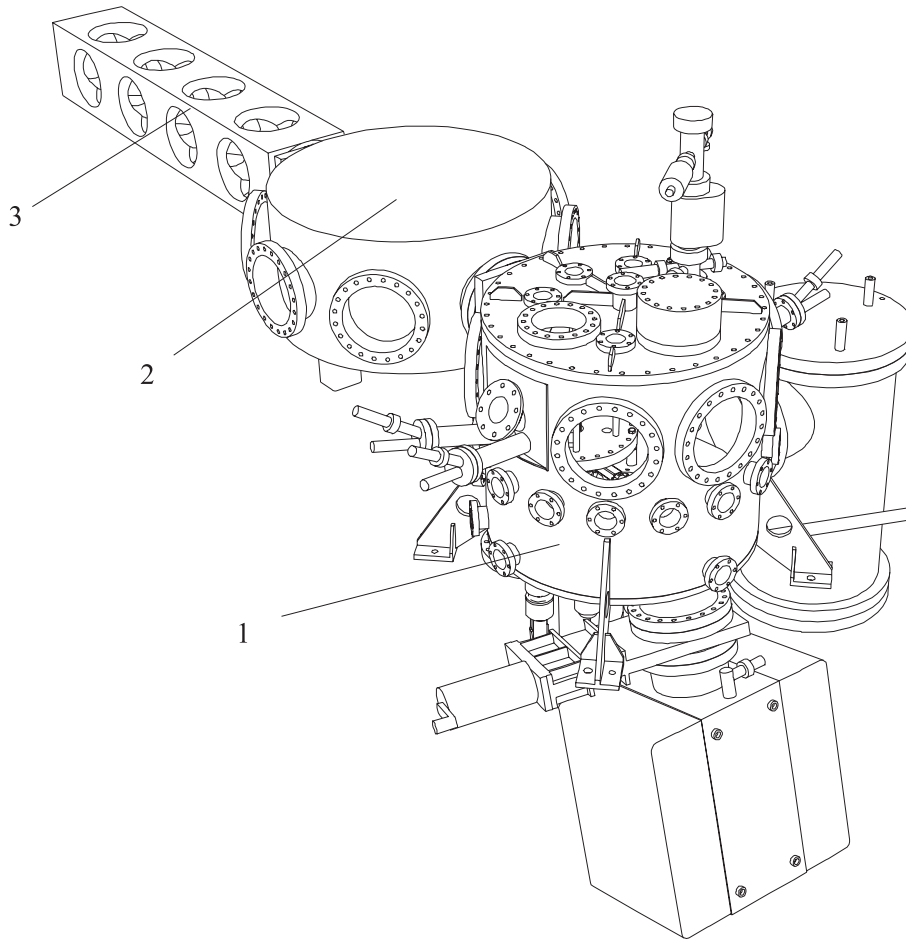


Figure 1.6: *The new UHV-setup consists of (1) the ‘new’ STM-chamber, (2) a transfer chamber and (3) the ‘old’ chamber.*

Connected to the transfer chamber are several other units (not shown in fig. 1.6), such as a scanner/sample storage chamber, designed to store up to 8 samples and 2 scanners, a large-thickness deposition chamber, and a load lock chamber. Inside the

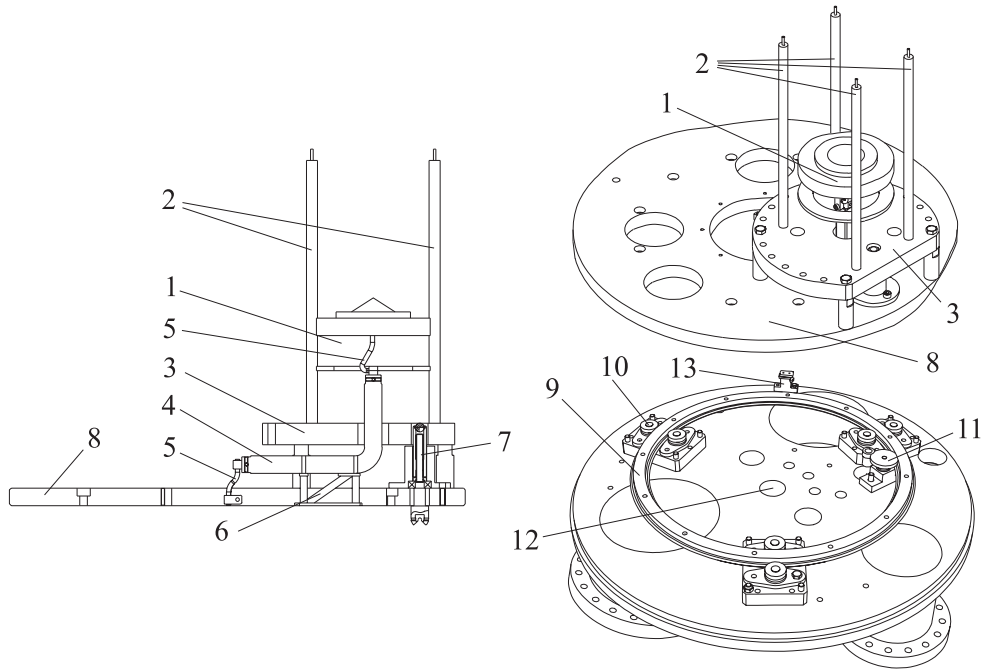


Figure 1.7: *The carousel consists of a top-part, which is shown in cross section (left panel) and in perspective (upper right panel), and a bottom-part (lower right panel).*

new chamber, the STM support block with the sample is placed on top of a carousel. The top part of this carousel is shown in cross section in the left panel and in perspective view in the upper right panel in fig. 1.7. It carries the eddy-current damped support block of the STM (1), hanging on springs (2), a support flange (3), a copper rod (4) that thermally connects the sample holder via two copper braids (5) to a cryostat, a thermally insulating support for the copper rod (6), a spindle nut (7) that can lock or unlock the spring suspension, and a big, supporting copper plate (8). This plate acts as a ‘thermal anchor’ for the support block of the STM, via additional copper braids. The purpose is to keep the temperature of the scanner approximately at room temperature, whilst the sample holder is either hot (1000 K) or cold (20 K).

This assembly is mounted on top of a sprocket (9) that is supported by UHV-compatible bearings (10). The sprocket is rotated by means of two cogwheels (11), of which one is mounted on a rotary feed through driven by a stepping motor. Since the gear ratio of the sprocket and the two cogwheels equals 1 : 23.4, the Cu-plate can be positioned with an average accuracy better than 0.005 degrees. Theoretically, this allows a controlled positioning of the sample within 20 μm . The cryostat is

mounted at the middle flange (12) of the base of the chamber. To prevent damage to the copper braids, which connects the cryostat with the copper rod and the carousel, an electrical end-switch (13) allows the sprocket to rotate only 360 degrees.

Figure 1.8 shows the new chamber in top view (a), in bottom view (b), and in cross section view: (c) and (d). The rotation of the carousel with the sample defines a circle: several flanges are placed on the lid of the chamber in such a way that their middles directly point to the middle of the sample, when it is positioned below them. There are four special positions. At the imaging position (3), the STM-support block can be locked or released for imaging, in which case it hangs from the spring suspension system. For this purpose, a self-designed rotatable linear feedthrough (4), positioned at the bottom of the chamber, can be coupled to the spindle nut (see above). The sample holder can be inserted into or removed from the block with a wobble stick at the transfer position (5). The STM scanner can be placed over the sample on the support block with the same wobble stick. If the gate-valve (6) is open, either the sample holder or the scanner can be moved by means of a home-built transfer system to/from the transfer chamber. The sample can be cleaned at the position of the differentially pumped sputter gun (7). Both the structure and the cleanliness of the surface can be measured with the combined LEED-AES system at position (8). The chamber is equipped with a mass-spectrometer (9) and a pressure gauge (10). Material evaporation onto the sample is possible at two positions with three Knudsen cells (11). The cryostat (12) is mounted at the middle of the bottom flange. Three pumps are attached at the STM-chamber: a magnetically levitated turbomolecular pump (13) that is coupled via a bellows (14) to the chamber, an ionisation pump (15), and a titanium sublimation pump (16) that is mounted inside a home-built cryo-pump (17). Several further flanges at the bottom of the chamber are used for electrical feedthroughs.

We summarise the components and their specifications in the following list:

The sputter ion gun is an IQE 12/38 from Specs. The differentially pumped gun is equipped with a Wien-filter to mass-select the proper ions. The FWHM of the beam is $\sim 120 \mu\text{m}$ at full focus. The beam can be scanned over an area of $10 \times 10 \text{ mm}^2$ with an accuracy of $100 \mu\text{m}$. This allows the bombardment of only the sample, which was not possible in the old setup. There, sometimes, the sample holder had to be covered with the same kind of material as the sample in order to prevent contamination.

The pressure gauge is a UHV-24 from Varian. Its special design gives accurate pressure measurements from $1.3 \cdot 10^{-3}$ mbar down to its x-ray limit, corresponding to a pressure indication of about $2.6 \cdot 10^{-11}$ mbar.

The LEED-AES system is a BDL 600 from OCI Vacuum Microengineering. The very small unit with a width of only 141 mm is mounted on a 8" flange, and fits between the four posts of the spring suspension system. AES is possible up

to 3000 V. This setup can easily separate the Ag-351 eV from the Ag-356 eV peak. It is equipped with a Lock-In SR810 from Stanford Research Systems.

The ionisation pump is a VacIon Plus 500 Star Cell from Varian. It has a pumping speed of 410 l/s and reaches an ultimate pressure lower than 10^{-11} mbar. It can handle a high throughput of noble gases and hydrogen and is ideal for applications requiring a constant vacuum of 10^{-8} mbar or below.

The titanium sublimation cartridge is a 916-0017 from Varian, which is equipped with 3 filaments.

The home-built cryo-pump has a capacity of 12.5 liter. First tests showed that it holds the low temperature for more than 15 hours after filling with liquid nitrogen.

The Knudsen cells are KC3s from Oxford Instruments. This water-cooled cell can operate up to 1500°C . The crucible is made from fine grain graphite, and contains a liner of PBN.

The turbo-molecular pump is a TPU180Hm from Pfeiffer Vacuum. This 170 l/s magnetically levitated pump has a base pressure below $5 \cdot 10^{-11}$ mbar. Remarkable are its compression ratios: more than 10^{12} for N_2 , $4 \cdot 10^7$ for He and $2.5 \cdot 10^5$ for H_2 .

The stepping motor is a ZRD6MGI from Vacuum Generators. With 400 half steps per revolution and a gear box ratio of 9:1, the resolution is 0.1 degrees. It is mounted on a rotary drive that can be baked up to 230°C , if the motor and the gear box are removed. We use the ZSMC1 electronics from Vacuum Generators to control the stepping motor.

The mass spectrometer is a Prisma QMS 200 of Pfeiffer Vacuum. Equipped with both a Faraday cup and a channeltron, it can be used from on $1 \cdot 10^{-4}$ mbar down to its detection limit of 10^{-14} mbar.

The cryostat is from Oxford Instruments and was delivered as a standard component of the STM assembly.

All components of the new setup have been purchased or manufactured, and large parts of the setup have been assembled already. The system is expected to be operational in 2002.

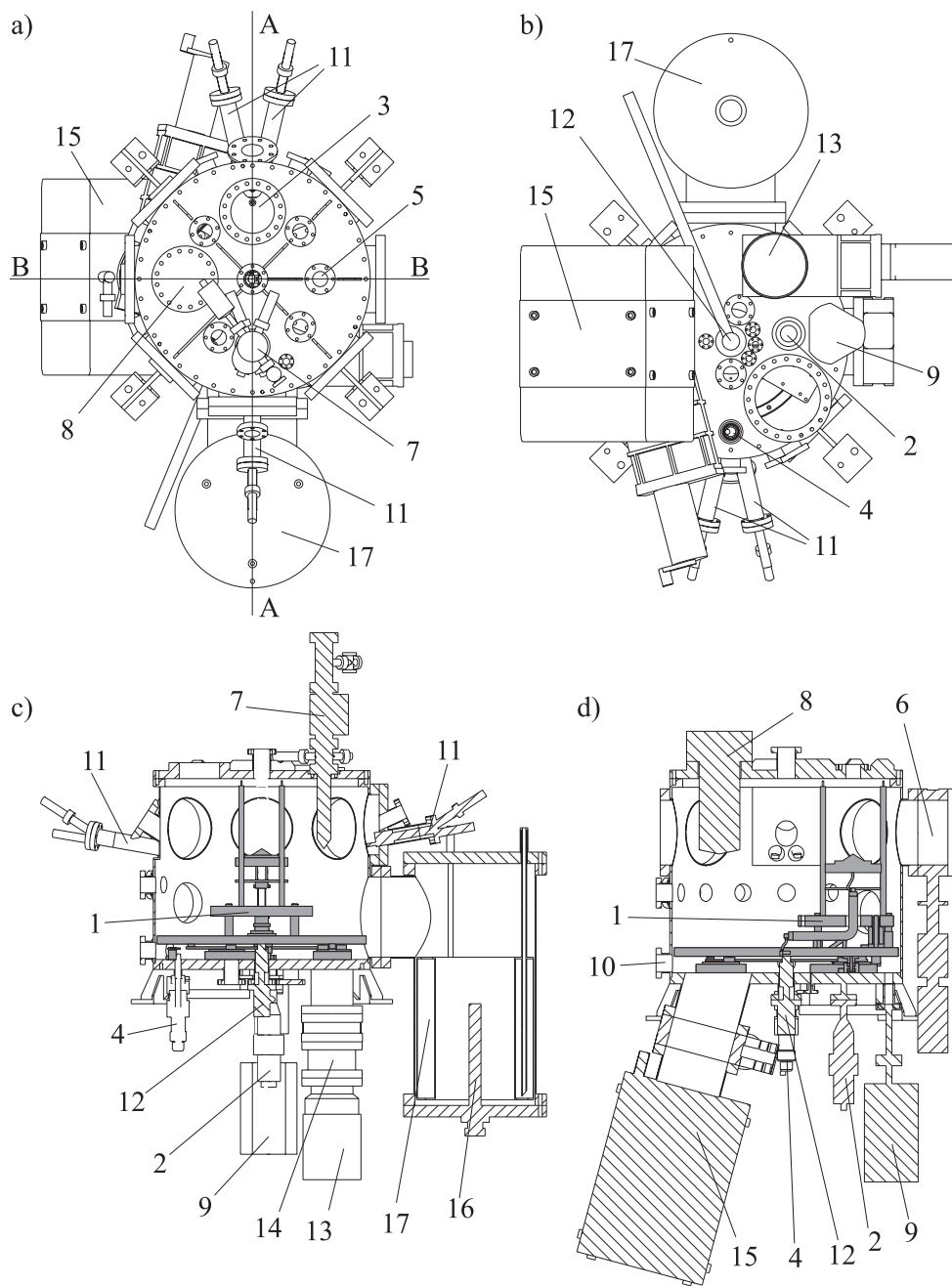


Figure 1.8: The 'new' STM-chamber in (a) top view, (b) bottom view, (c) cross section along line A in panel a, and (d) cross section along line B in panel a.

Chapter 2

General Background

In this chapter the concepts and phenomena on crystal surfaces are introduced that play a role in the rest of this thesis. They include structure, interactions, phase transitions, and diffusion dynamics. At the end of this chapter the specific case of the Au(110)-surface is discussed.

2.1 Terrace-Ledge-Kink Model of Crystal Surfaces

In general, a surface can be seen as the result of a cleavage of a single crystal along some crystallographic plane. The energy which one has to pay for this cleaving process is due to the breaking of atomic bonds. Therefore the surface energy can be viewed as half the energy, needed for cleaving. In reality, surfaces are almost

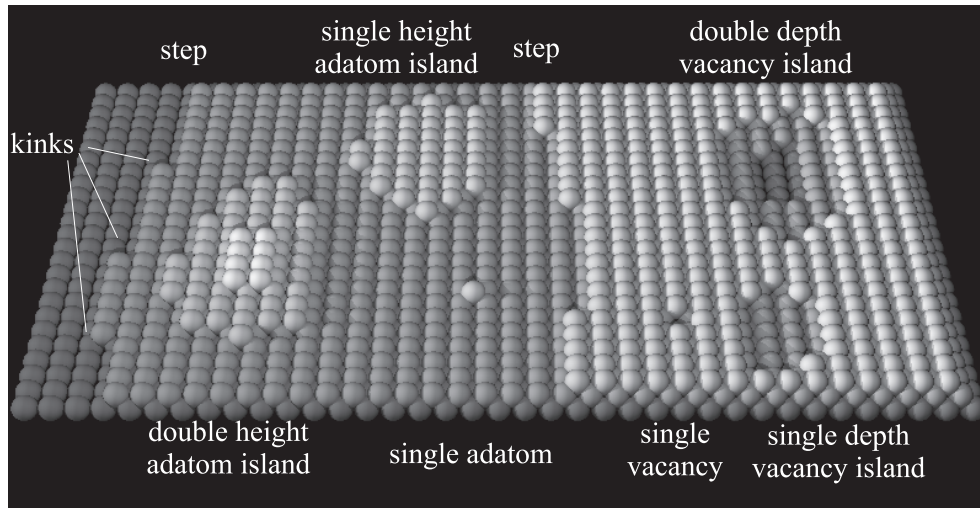


Figure 2.1: Schematic ball model of a fcc (110)-surface showing several defects.

never perfect; several types of defects can be found (see fig. 2.1). Cutting a crystal perfectly along a crystallographic plane is usually not possible. As a consequence of the miscut, monatomic height steps are unavoidable. The perfectly oriented regions between two such steps are called terraces.

Creating a step on the surface costs energy, which is referred to as the step formation energy. This is because atoms at the step edge are less bound than atoms in the perfectly flat terrace, where they have more neighbours.

Steps contain point defects, called kinks, at which they are displaced by one atomic spacing perpendicular to a main step direction. The energy, which has to be paid for the introduction of such a kink, is defined as the kink formation energy. The description of surfaces in terms of terraces, steps and kinks was already introduced in the late twenties by Kossel [15] and is known as the Terrace Ledge Kink (TLK) model.

Adatom or vacancy islands are the result of the formation of a closed step contour. The formation energy of these islands can simply be calculated by adding the energies of all steps and kinks, which are introduced in the island. The smallest possible structures, a missing atom in a flat terrace or an extra atom on top of a terrace, are called vacancy or adatom, respectively. On their small size scale, the description

of the formation energy as a sum of the step energies breaks down. Therefore, we introduce separate vacancy and adatom formation energies.

2.2 Free Energy: the Role of Entropy

At all temperatures other than $T = 0$ K each structure, such as a step or a surface, is characterised better by the free energy than by only the formation energy. This is because the free energy takes the entropy into account involved in the allowed variety of configurations.

Imagine, for example, a perfectly straight step (n atomic spacings long), without any kinks, aligned along a main direction of the surface. For the formation of this step we have to pay the step formation energy. The additional introduction of one kink in this step costs extra energy, the kink formation energy. Since we can place this kink anywhere along the step, we also increase the entropy, S , which lowers the free energy, $F = n \cdot E_{step} + E_{kink} - TS$, of the step at $T \neq 0$ K. Therefore, at each temperature, a different density of kinks will be generated thermally in the step in order to reach the minimum in the free energy. The presence of the kinks causes the meandering of a step. The same considerations are also valid for a surface, which minimises its free energy by introducing height differences, in the form of islands.

Within the framework of the terrace-ledge-kink description of surfaces, the statistical mechanics of structures (such as facets, steps, and islands) can often be treated analytically to yield the temperature dependent free energies of the structures, from which their densities can be obtained. A well-known example of the natural result of the free energy minimisation is that of the equilibrium shapes of three-dimensional crystals or two-dimensional structures, such as adatom and vacancy islands.

2.3 Equilibrium Shape: Wulff Construction

Let us consider an adatom or a vacancy island on a flat terrace, as is shown e.g. in fig. 2.1. In order to minimise its free energy, the island reduces its total step length via diffusion of atoms along the steps. This leads to a more compact shape, for example a circle for isotropic media. Since the step free energy strongly depends on the orientation of the step (i.e. the surface is strongly non-isotropic), the minimum free energy island shape usually differs significantly from a circle.

The equilibrium shape of a two-dimensional island on a flat crystal surface can be constructed from the polar plot of the step free energy $f(\phi)$, by applying the two-dimensional version of the well-known Wulff construction [16, 17]. As an example, fig. 2.2 shows the construction for the case of Cu(110) at 400 K. To every point of the polar plot, a line is drawn from the origin W (Wulff point), such as the one in the upper left quadrant. Perpendicular to this line at its intersection with the polar plot, a line is drawn. When all the latter lines are combined, as in the upper right quadrant,

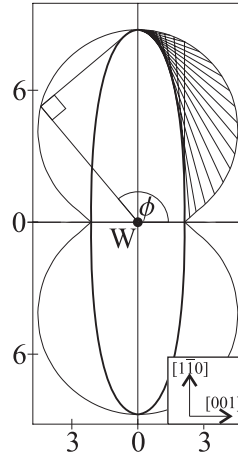


Figure 2.2: Polar plot of the free energy $f(\phi)$ of steps on $\text{Cu}(110)$ at 400 K (thin curve). Energies are expressed in $\text{meV}/\text{\AA}$. The Wulff construction is used to determine the equilibrium shape of islands on this surface (thick curve). The step free energy at each angle ϕ has been calculated under the assumption that the formation energy for each step configuration is a simple sum of formation energies of atomic step segments along the two symmetry directions, $[001]$ and $[1\bar{1}0]$. For these we used values of $\epsilon_{[001]} = 102 \text{ meV per lattice spacing along } [001]$, of 3.61\AA , and $\epsilon_{[1\bar{1}0]} = 9 \text{ meV per atomic spacing along } [1\bar{1}0]$, of 2.55\AA , obtained from Effective-Medium-Theory calculations [18]. The directions of the $[1\bar{1}0]$ - and $[001]$ -steps are indicated by the arrows.

the interior contour has the shape which minimises the total free energy of the island for a fixed total island area. This graphical construction is equivalent to applying a Legendre transform to the polar free energy plot [19, 20].

A popular method to determine ratios between step free energies is to apply the inverse Wulff construction to images of two-dimensional islands. One identifies the Wulff point as the center of mass of an island, and then applies the Wulff construction in reverse order to obtain the step free energy plot to within a constant scale factor [21, 22]. In addition, the temperature dependence of the island shape can be used to obtain an absolute scale for the step free energies [23, 24]. It will be argued in chapter 7 that this method is *not always* correct. In some cases the Wulff point does not coincide with the center of the island.

Since the equilibrium shape of an island is only determined by the free energy of the steps at its perimeter, each level in a multilayer island can independently adopt the equilibrium shape, provided that the distances between the steps are all sufficiently large. This ‘independent-layer’ picture breaks down, when the density of steps is so high that step-interactions no longer can be neglected. Multilayer islands for which this is the case, should be regarded as a portion of a three-dimensional crystal.

The equilibrium shape of a three-dimensional crystal can be obtained by the use of the three-dimensional generalisation of the described two-dimensional Wulff-construction, in which the step free energy is replaced with the surface free energy, and the perpendicular (Wulff) lines are replaced with perpendicular Wulff planes.

2.4 Phase Transitions

Crystal surfaces can undergo various order-disorder phase transitions. At the transition temperature, the entropy gain outweighs the formation energy for creating new structures. The examples discussed in this thesis are the *roughening* and the *deconstruction* transition. The deconstruction transition will be introduced in section 2.8. At the critical temperatures of both phase transitions, the free energy of a particular structure vanishes.

At the roughening transition, T_r , the free energy of a step vanishes. At and above T_r the surface is free to form an unlimited number of steps as the original reference plane becomes lost. The width of the interface diverges with increasing lateral distance on the surface, which can be quantified by means of the height-height correlation function, which is the mean-square height difference between different points on the surface, as a function of the lateral distance. For a rough surface, this function is proportional to the logarithm of the distance, whereas it remains finite below T_r [25, 26]. This transition is in the Kosterlitz-Thouless universality class [27], which makes it a phase transition of infinite order.

Due to presence of sharp cusps in the anisotropic surface free energy polar plot, the equilibrium shape of a crystal shows facets at low temperatures. At the roughening transition of a facet, the corresponding cusp changes into a smooth minimum, leading to the disappearance of this surface orientation in form of a facet with a finite area from the equilibrium shape of the crystal [28]. Recently, it has been shown theoretically that some crystals may undergo an ‘inverse’ roughening transition [29]. This means that the considered crystal facet occurs *above* a certain transition temperature.

For completeness, it is important to consider the roughening transition of a step. Each step is rough at any temperature $T \neq 0$ K. This is because at each non-zero temperature the step contains a finite, non-zero density of kinks, irrespective of the kink formation energy. Looking along the step direction one will find a random sequence of kinks, some to the left, others to the right. This sequence can be regarded as a random walk of the step itself perpendicular to its main direction. After N kinks the mean square change in position of the step is proportional to N . This corresponds to a linear divergence of the step position correlation function (mean-square displacement as a function of position along the step) for any $T \neq 0$ K. As a consequence, at all orientations for which there are cusps in the step free energy plot at $T = 0$ K, one finds only smooth minima at $T > 0$ K. This implies that the two-dimensional equilibrium shape of islands never contains straight sections.

This argumentation does not hold for the facets on a three-dimensional shape, because there we have to introduce infinitely long steps or, equivalently, infinitely large numbers of islands to loose the height correlation. This is because it would otherwise always remain possible to stay on the same height by going around an island. Infinitely long steps cost an infinitely large amount of energy. Only when the temperature is so high that the configurational entropy reduces the step free energy to zero, the surface can generate the large structures that make the height-height-correlation function diverge.

2.5 Step-Step-Interactions

Neighbouring steps on a surface interact [30, 31]. One can distinguish several sources for this interaction. The first is an elastic interaction based on the deformation of the lattice in the vicinity of a step. Steps are thought to carry an electrostatic dipole moment, through which they also exert forces on each other. Finally, there is a purely statistical interaction based on entropy. The origin of the latter interaction is the condition that steps usually cannot cross (see chapter 3 for an exception). This reduces the freedom for two nearby steps to meander and thereby reduces their configurational entropy. Let us focus here on the elastic interaction, which has been treated in the framework of continuum elasticity theory [32, 33, 34]. The step atoms relax away from lattice positions, which results in an elastic displacement field in the nearby bulk¹. The displacement field of a step interacts with the elastic forces from other steps, which causes the elastic contribution to the surface free energy.

If two interacting steps are of the same type, both ‘up’ or ‘down’, they repel each other, whereas if they are of opposite types, one ‘up’ and one ‘down’, they can either repel or attract each other. Figure 2.3a shows the displacement field of a periodic

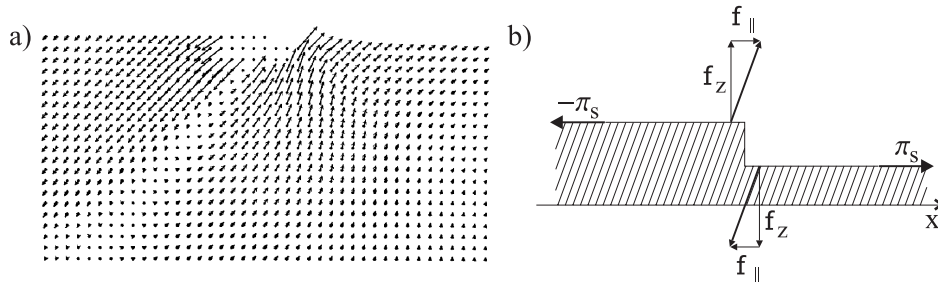


Figure 2.3: (a) Displacement field of a step calculated for Ni(001), using the embedded atom model [35] (reproduced with permission). The displacement vectors have been exaggerated, and are not shown around the core region. (b) Representation of the counter forces which cancel the displacements.

¹The field decays with the distance from the step.

array of ‘down’-steps along the [001]-direction on a nickel (001)-surface. Although the pattern of the displacements seems very complicated, it is important to realise that at a macroscopic scale the entire displacement field can in principle be cancelled by external forces, which can be approximated by a force doublet, $\pm F_i$, as sketched in fig. 2.3b:

$$F_i(x) = \mathbf{f} \delta'(x) \quad (2.1)$$

\mathbf{f}_{\parallel} describes the local stretch term of the surface, which is the same for ‘up’ and ‘down’ steps, and $\mathbf{f}_z \sim \pi_S a$ is a local torque term, which tends to twist the crystal around the step direction; $\pm \pi_S$ is the surface stress and a the step height. The interaction energy, E_{step} , between two steps can be derived by multiplying the displacement field produced by one step at the position of the other step with the cancellation forces of the latter. For two parallel running steps, which are a distance d apart, one obtains [30, 31, 34]:

$$E_{step} = \frac{2(1 - \sigma^2)}{\pi Y} \frac{\mathbf{f}_{\parallel}^2 \pm \mathbf{f}_z^2}{d^2} \quad (2.2)$$

per unit of step length, where Y and σ are the Young’s modulus and the Poisson’s ratio, respectively. Since the contribution of the stretch term is always positive, this term is always repulsive. The contribution of the torque term, on the other hand, can be either positive or negative, since they cause displacements in the same direction for the same kind of steps ($+\mathbf{f}_z^2$) and in opposite direction for different kind of steps ($-\mathbf{f}_z^2$). Whether the total interaction will be attractive or repulsive in the latter case depends, therefore, on the ratio of \mathbf{f}_{\parallel} and \mathbf{f}_z (see eq. 2.2).

Interestingly, also the two other interactions, entropic forces and electrostatic dipole forces, decay proportionally to the inverse step distance d^{-2} . Elastic and entropic effects are the major contributions to the step-step-interaction.

2.6 Surface Diffusion

At most temperatures, surfaces are far from static and diffusion of objects and structures (such as islands, steps, and kinks) can be recognised. Figure 2.4a shows the energy landscape for an adatom on two terraces that are connected via a step. Imagine the adatom on top of the higher terrace as sketched in the cross section in fig. 2.4b. Sitting in the energy minimum between two atoms of the terrace, the adatom can hop to a neighbouring position by overcoming the energy barrier E_d . This process is thermally activated and therefore, within transition state theory, the diffusion constant, which is proportional to the average number of successful hops per unit time, is proportional to $e^{-E_d/k_B T}$ (k_B : Boltzmann constant, T : temperature). After randomly hopping on the higher terrace, the atom may encounter the step. On some surfaces, steps introduce an additional energy barrier, the so-called Ehrlich-Schwoebel barrier

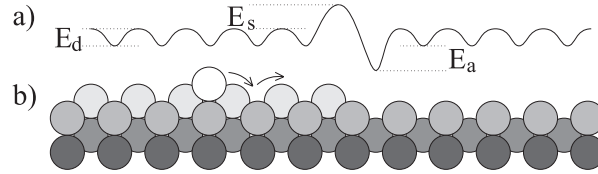


Figure 2.4: Schematic cross section of a step: (a) energy landscape (b) ball model.

E_s [36, 37, 38]. If the atom succeeds in overcoming this barrier, it descends to the lower terrace, where it becomes more tightly bound at the position next to the step, the minimum is reduced by an additional energy, E_a . The probability that the atom will diffuse away from this position onto the flat terrace is low. On the other hand it can, usually, move relatively easily along the step, because of the low energy barrier typically encountered along that direction. Therefore the atom may be expected to perform a random walk along the step edge, until it encounters a kink, where it becomes more tightly bound again. Only a small fraction of the atoms that diffuse along the steps manages to jump onto the terrace before being recaptured by the kinks. In this way the steps serve as sources of adatoms.

But, adatoms are not the only diffusing species on a surface. Single vacancies diffuse through the terraces, and shuffle around the atoms [39, 40, 41, 42]. Since both the formation energies and the diffusion barriers on/in a terrace are of the same order of magnitude for adatoms and vacancies on fcc metal (100)- and (110)-surfaces [18], mass transport is expected to take place via both types of diffusion. On metal fcc (111)-surfaces, the adatom diffusion barrier on a terrace is usually one order of magnitude lower than the barrier for the vacancies. There, we expect adatom diffusion to dominate the mass transport.

2.7 Coalescence and Ostwald Ripening

There are two different evolution processes, by which surfaces with vacancy or adatom islands can lower their total free energy. The first process is coalescence, and involves islands encountering each other and fusing together to form larger islands. The second process, called Ostwald ripening [43], involves individual atoms (or vacancies) being exchanged between the islands via the terrace. The frequency of coalescence events strongly depends on the density of islands, whereas Ostwald-ripening can be independent of island density. Without loss of generality we restrict our discussion to the case of adatom islands.

Coalescence occurs when islands diffuse as a whole, which is possible via, e.g., atom diffusion along the step edges [44, 45, 46, 47]. If two islands encounter each other during their random walks, they lower their free energy by fusing together, thereby reducing the total step length for the same number of atoms.

diffusion limited	attachment limited
$\frac{dr}{dt} \sim -\frac{1}{r} \left(\frac{1}{r} - \frac{1}{r_0} \right)$	$\frac{dr}{dt} \sim - \left(\frac{1}{r} - \frac{1}{r_0} \right)$
$\frac{d\tilde{A}}{dt} \sim -\frac{1}{r}, (r \ll r_0)$	$\frac{d\tilde{A}}{dt} \sim -\text{const}, (r \ll r_0)$
$\tilde{A}(t) \sim (t_0 - t)^{2/3}$	$\tilde{A}(t) \sim t_0 - t$

Table 2.1: *Scaling laws for diffusion limited and attachment limited ripening of circular islands [49, 50, 51]. The expressions have been derived in the mean-field approximation, and with a linear approximation to eq. 2.3. The radius r_0 corresponds to the island size for which the arrival and departure rates of atoms are precisely balanced. This equilibrium size is, of course, also a function of time. The time at which the area of the (small) island becomes zero is t_0 .*

Ostwald ripening is an effect of single atom diffusion. The random walks of atoms, which detach from and attach to each island make the islands ‘communicate’ with each other. As the detachment rate per unit step length is higher for smaller islands, bigger islands grow on average at the expense of smaller ones [40, 43, 48]. Usually, two different limiting cases are discussed: *diffusion* limited and *attachment* limited ripening. The first is characterised by gradients in the adatom density in the neighbourhood of the islands, and is treated under the assumption of an equilibrium adatom density directly next to the island and characteristic for the island itself, as described by the Gibbs-Thomson equation. This equation can be written for a two-dimensional system as:

$$\rho_{eq}(r) = \rho_{\infty} e^{\gamma/k_B T n_s r} \quad (2.3)$$

where $\rho_{eq}(r)$ is the adatom equilibrium concentration of a cluster with radius r , ρ_{∞} the adatom equilibrium concentration of a straight step, i.e. of an island with an infinitely large radius, γ the step free energy, k_B the Boltzmann constant, T the temperature and n_s the density of atoms on the surface. The attachment limited case refers to a mechanism in which the rate limiting step is the incorporation of atoms into the island edge. In the case of diffusion limitation the ripening velocity is limited by the detachment of atoms from islands, whereas in the attachment limited case, the velocity is determined by the attachment of diffusing atoms to the islands. The time dependence for a circular island with an area \tilde{A} is solved under the assumption of small island density: the distance between the islands is so large that the two-dimensional adatom pressure in between them reaches the mean-field value. Since

$\frac{d\tilde{A}}{dt} = \frac{\delta\tilde{A}}{\delta r} \frac{dr}{dt}$ we can write

$$t \sim \int \frac{\delta\tilde{A}}{\delta r} \left(\frac{d\tilde{A}}{dt} \right)^{-1} dr \quad (2.4)$$

and one obtains with $\tilde{A} \sim r^2$ the scaling laws written in table 2.1 [49, 50, 51]. These scaling laws have been verified experimentally for a variety of systems, as is illustrated in fig. 2.5, which has been taken from [52].

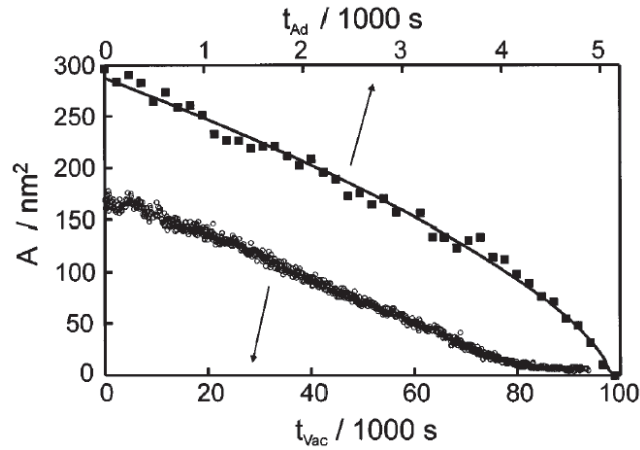


Figure 2.5: Two typical forms of island decay behaviour, demonstrating the two regimes of table 2.1. Both curves are area versus time plots measured at 300K for Ag(111). Open circles: vacancy island decay (bottom time axis) showing the linear behaviour characteristic for attachment-limited Ostwald ripening; solid squares: adatom island decay (top time axis), with a $(t_0 - t)^{2/3}$ fit, for diffusion-limited Ostwald ripening. Reproduced with permission, from [52]

2.8 Au(110)-Surface

The structure of a gold single crystal is face centered cubic (fcc) with a lattice constant (l.c.) of 4.08 \AA . The simple cleavage picture, presented in section 2.1, is not adequate for the three low-index surfaces of this material. Whereas many low-index surfaces have a bulk-terminated structure, with modest, vertical lattice relaxations that decay in magnitude with increasing depth, the (111), (100), and (110) surfaces of Au exhibit structures that differ from a simple bulk termination. The alternative structures (superstructures) repeat themselves with a larger period, which is a multiple of the naively expected surface lattice distances. In the cases of Au(111) and Au(100), the surface structures are quasi-hexagonal with average interatomic spacings, which are smaller than the normal repeat distance in a bulk (111)-plane. At the expense of the mismatch between these quasi-hexagonal surface layers and the underlying bulk, Au(111) and Au(100) thus maximise their atomic density in the surface. The response of the Au(110) surface is, in a sense, similar. The open structure of the

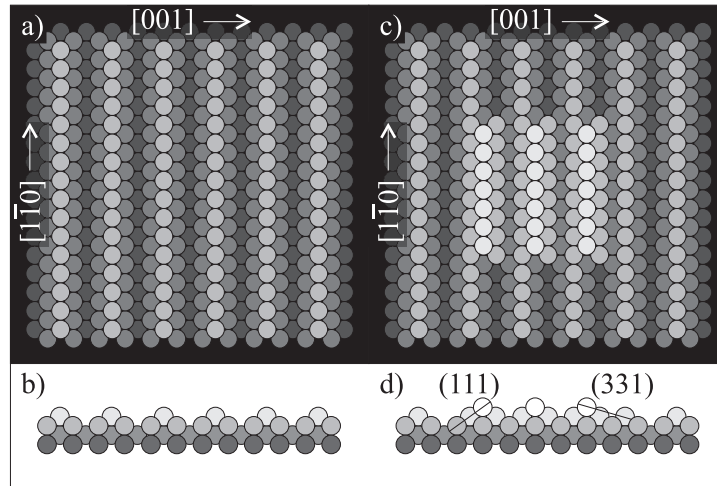


Figure 2.6: *Perfectly flat Au(110)-surface: (a) schematic topview (b) schematic cross section. Adatom island in topview (c) and in cross section (d), showing two different types of $[1\bar{1}0]$ -steps: a (111)-step and a (331)-step.*

bulk-like (110)-surface is replaced by a regular pattern of narrow (111)-microfacets, even though this seems to increase the total area. Along the [001]-direction every second atom row is missing, doubling the repeat distance along this direction, while keeping the repeat distance along the $[1\bar{1}0]$ -direction unchanged. Hence the name: (1x2) missing-row-reconstruction (MRR); see fig. 2.6 a, b. Figures 2.6 c,d show an adatom island, which is constructed under the assumption that the island also adopts the MRR-structure. As a consequence, this island has two different types of steps along the $[1\bar{1}0]$ -direction, which we will refer to as a (111)-step and a (331)-step, to

indicate the orientations of the microfacets formed by these steps.

Figure 2.7a shows a typical STM-image of Au(110) with atomic row resolution on the MRR. In the lower part of the image we notice terraces, which are placed on top of each other to form an inclined part of the surface (miscut). In contrast to the usual situation that each level adopts the equilibrium shape independently, as discussed in section 2.3, it appears that the steps cross each other on the Au(110)-surface, as indicated by the white lines in the image. This unusual behaviour is emphasised by the comparison between the large-scale appearance of the Au(110)-surface and that of a more typical surface, such as Cu(001). Figure 2.7b shows a large-scale image of a relatively rough Cu(001)-surface [53]. The image has been differentiated along the horizontal direction, to enhance the contrast of the steps; the differentiation appears as a ‘light source’ placed to the right of the image that throws leftward shadows on the surface. Crossing steps are never found on Cu(001), even though the surface was not given sufficient mobility to let each island relax to its equilibrium, square-like shape. All height differences are overcome by placing islands on top of each other. In contradiction, figure 2.7c shows that the Au(110)-surface overcomes height differences by introducing crossing steps. The depicted surface is higher in the lower right corner than in the upper left corner. Together, all the crossing steps form a network structure (indicated by the white solid lines), which is often referred to as a *fish scale pattern*.

If we follow a step at constant height in the network structure, we see that it follows a zig-zag pattern, which is indicated by the thin black line. The origin of the fish scale pattern lies in the answer to the important question: why do the steps prefer a zig-zag structure and crossing geometry over a simple straight geometry, as indicated by the white, dotted lines in fig. 2.7c? Obviously, the surface ‘chooses’ for a solution with much longer step length. Why is this so?

The reason for this unusual behaviour requires a new understanding of these step networks and of the connection between the flat, perfectly oriented Au(110) MRR-parts and the misoriented network structures. This is discussed in chapter 3.

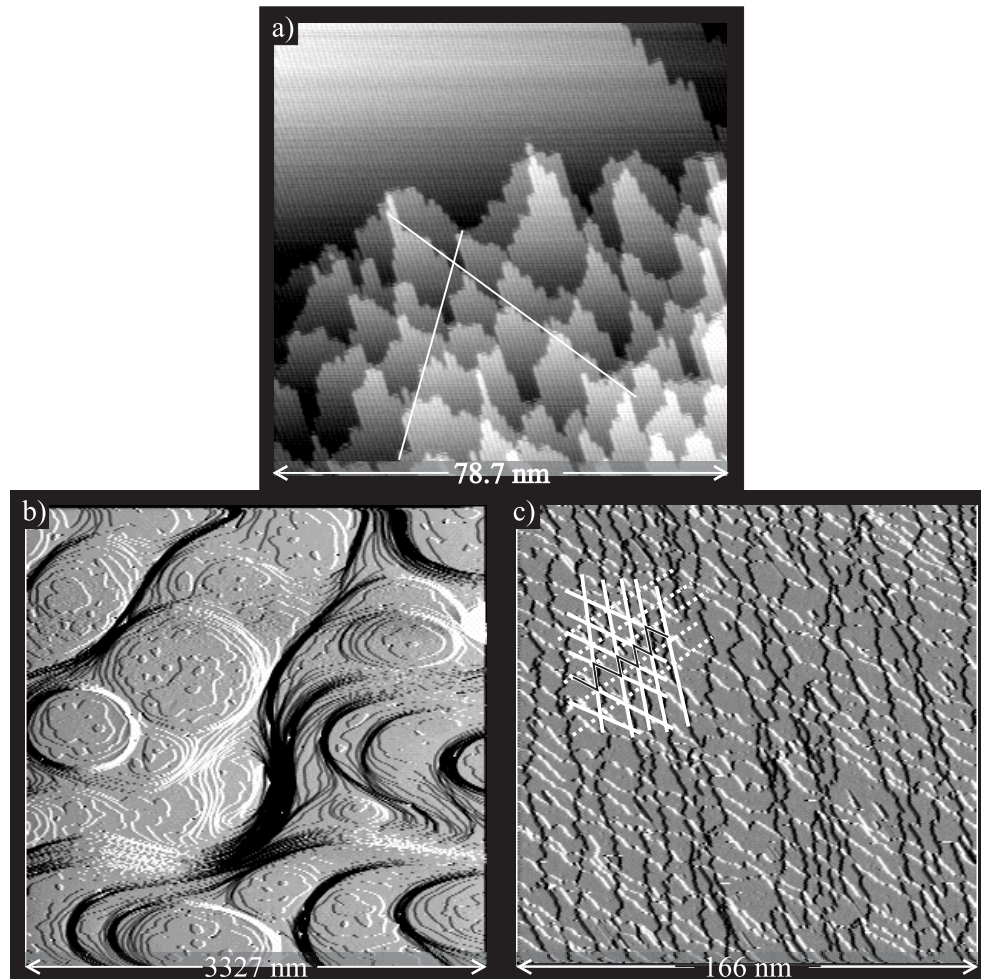


Figure 2.7: (a) STM-image of Au(110) at $T=326$ K. Single atom rows of the MRR are resolved. Notice the perfectly flat part in the upper part of the image and the network structure, which is built up of crossing steps in the lower part. In order to emphasise the difference between the steps on Au(110) and those on other surfaces, panels (b) and (c) compare two larger-area images on Cu(001) [53] and Au(110). These STM-images were taken at room temperature, they were both differentiated to enhance the step contrast: (b) Cu(001) and (c) Au(110). Notice the formation of compact islands on top of each other in b and the crossing of steps in c.

2.8.1 Reconstructions

The Au(110)-surface was one of the first surfaces that was studied with STM [2]. During the early studies of the Au(110)-surface there has been a discussion about its structure, which is nowadays well known as the 1x2 missing-row reconstruction. Low energy electron diffraction (LEED) observations, some showing (1x2)- and some showing (1x3)-spots, raised questions about the equilibrium atomic structure of the surface [54, 55]. Calculations for Au(1xN) reconstructions, constructed from (111)-

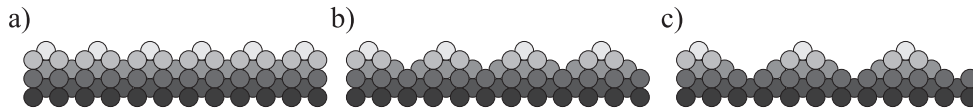


Figure 2.8: *Schematic cross sections of (a) (1x2)- (b) (1x3)- and (c) (1x4)-reconstructions, which are all constructed from (111)-microfacets.*

microfacets as illustrated in fig. 2.8, showed only small differences in their formation energies [56]. In chapter 6, the energy of one period of the (1x3)-reconstruction is determined and shown to be only slightly higher than the corresponding energy for the (1x2)-reconstruction, in accordance with the calculations.

2.8.2 Phase Transitions

In section 2.4, we have already introduced the roughening transition, which occurs when the step free energy on an otherwise flat surface vanishes. Observations with LEED have indicated the presence of a second phase transition on Au(110) at elevated temperatures. The MRR gives rise to additional (1x2)-spots in surface diffraction patterns. Wolf et al. [57] were the first to notice the weakening and disappearance of these spots in the LEED-pattern, indicating a disordering transition of the reconstruction.

The origin of this so-called ‘deconstruction’ transition is easy to understand. The equilibrium structure of the Au(110)-surface is formed by a (1x2) missing-row reconstruction. There are two possible phases (domains) of the MRR. In one phase the *even* atom rows are missing while in the other one the *odd* atom rows are missing. Whenever both phases are present, the surface has to form a domain boundary between them. The domain boundary free energy can be lowered via the introduction of kinks, in a manner similar to that discussed for steps (see 2.4). This means that also the free energy of such a domain boundary decreases as a function of temperature. When it becomes zero, the surface can freely form domain boundaries, which leads to a complete disorder of the (1x2) periodicity of the Au(110) reconstruction. This is why this transition is called deconstruction. Since the resulting surface is still flat, it is referred to as being in the disordered flat phase.

As there are two possible MRR phases, Bak [58] predicted this transition to show typical Ising-type behaviour. Campuzano et al. [59] were the first to report experimental evidence for this Ising character. On the other hand the roughening transition, which is also expected to occur on Au(110), is of the Kosterlitz-Thouless type [27]. Villain and Vilfan [60] proposed the possible coupling of these two transitions, which they [61] as well as den Nijs [62] investigated theoretically. Whether both transitions are realised independently, and if so, to what extent the transitions influence each other, depends on the ratio of the formation energies of domain boundaries and steps. Sprösser et al. found the two transitions to occur on Au(110) at separate temperatures in a thermal energy atom scattering (TEAS) experiment [63]. A similar conclusion was reached in medium-energy ion scattering (MEIS) experiments by Romahn et al. [64]. Mazzeo et al. [65] and Barbier et al. [66] also found separate transitions in Monte Carlo simulation studies. Sturmat et al. have attempted to observe the two transitions with STM [67, 68].

In this thesis the relevant formation energy values of a step (chapter 3), a domain boundary (chapter 5) and a kink (chapter 6) are determined. The theories in refs. [61, 62] allow us to make accurate statements about the nature of the coupled deconstruction and roughening transitions (chapter 5).

2.8.3 Diffusion on Au(110)

There are two primary diffusion directions for Au adatoms on this surface. One is along the $[1\bar{1}0]$ -troughs and is called *in-channel* diffusion, whereas the other one is perpendicular to the troughs and is called *cross-channel* diffusion. Beautiful STM observations of in-channel diffusion of Pt adatoms on the MR reconstructed Pt(110)-surface can be found in ref. [69]. In the cross-channel case atoms must either jump over the atom rows of the MRR, or push out an atom of a row and simultaneously take over the empty position. The latter is called *cross-channel exchange*. Cross-channel diffusion is expected to have a significantly higher activation energy than in-channel diffusion, which is consistent with the observations for Pt(110) [69].

2.8.4 Au(110) in Numbers

Table 2.2 summarises the quantities, characteristic for the Au(110) surface, as known prior to the present investigation. At the end of this thesis the table is repeated, complemented with the information obtained from our STM-studies on Au(110). The formation energies are given per atom spacing (a.s.) along the $[1\bar{1}0]$ -direction of 2.88 Å.

structure or parameter	energy	or	temp.	ref.	method
single atom row energy	$E_{[1\bar{1}0]}^{331} + E_{[1\bar{1}0]}^{111}$	=	19 meV	[70]	STM
(111)-step energy	$E_{[1\bar{1}0]}^{111}$	=	1.8 meV	[71]	EAM
(331)-step energy	$E_{[1\bar{1}0]}^{331}$	=	9.5 meV	[71]	EAM
deconstruction transition	T_d	\simeq	[650, 765] K	[72]	LEED
roughening transition	T_r	\simeq	$T_d + 50$ K	[64]	LEED
in-channel jump	barrier: E_{icj}	=	0.31 eV	[73]	MD
cross-channel jump	barrier: E_{ccj}	=	0.63 eV	[73]	MD
cross-channel exchange	barrier: E_{cce}	=	0.66 eV	[73]	MD

Table 2.2: Characteristic quantities for Au(110). EAM stands for Embedded Atom Model calculation and MD for Molecular Dynamics simulation.

Chapter 3

Symmetric ‘Almonds’

Anomalous shape and decay of islands

We observe an extraordinary equilibrium shape, almond-like, of adatom and vacancy islands on the Au(110)-surface: each island contains two smoothly curved steps, joined at two sharp corners. Two different types of corners can be found: corners where two steps seem to cross and corners where two pairs of steps reach the corner from the same side and end there. We refer to these as crossing and termination sites. We point out the importance of these two types of sites and show that combinations of them allow the formation of network structures to accommodate any height variation at low energy cost. We will see that networks of steps with crossing and termination sites provide the means to connect the perfectly oriented parts of the Au(110)-surface, which are at different heights. The precise equilibrium, almond island shape is completely determined by two different step energies. These energies also determine an equilibrium angle, under which the four steps end at a termination site. By measuring this angle at different temperatures we determine the two step energies. Finally, we concentrate on the spontaneous decay of the almond-shape islands at elevated temperatures. We observe that the disappearance of the top level of a mound is accompanied by an unusual splitting of the underlying terrace into two separate parts. An explanation for this behaviour is found in the structure of the networks. A quantitative analysis of the decay of islands suggests a breakdown of the ‘independent’ layer picture of multilayer structures, mentioned in section 2.3.

3.1 Equilibrium Shapes with Sharp Corners

The equilibrium shape of a three-dimensional crystal can be predicted via the well-known Wulff construction on the basis of the orientation-dependent surface free energy [74]. Similarly, one can obtain the two-dimensional equilibrium shape of an adatom or vacancy island on a flat surface from the step free energies (see also section 2.3 and chapter 4) [21, 75]. Usually, such a two-dimensional equilibrium shape contains neither straight sections nor sharp corners at any non-zero temperature (see section 2.4) [76, 77]. Even when an island shrinks in size, due to Ostwald ripening, it normally keeps the same equilibrium shape, and simply decreases in area [40, 52] (see section 2.3 and section 2.7).

The observations of islands presented in this chapter confirm the recent prediction of a peculiar island shape on the Au(110)-surface, which features two sharp corners at non-zero temperature [78]. The origin of the sharp corners lies in the fact that certain step orientations are expelled from the surface and replaced by linear combinations of other ones. We show that the MRR, which is responsible for this shape, also influences the decay of the islands, making the layer below a disappearing island break up into two separate regions. Finally, we show that the islands go through a dramatic change in shape during their decay, which is reflected also in the islands' decay dynamics.

3.1.1 Observation

Despite a large number of STM studies on Au(110), the shapes of compact adatom or vacancy islands have not been investigated on this surface. Most of the equilibrium island shapes that are studied in this chapter have been observed on larger, three-dimensional mounds and valleys. As will become clear in this chapter, this is, in fact, the only way for islands to occur on a surface with the MRR, such as Au(110). The typical sizes of the three-dimensional structures are so large, both in the lateral direction (micrometers) and in height (tens of nanometers), that it is very difficult for most STMs to capture the complete equilibrium island shape within one image. Although we successfully created and observed these larger structures, we have not succeeded in the formation of similar islands on a nanometer scale by using ion-bombardment, since this led to metastable islands, which we will discuss in chapters 6 and 8.

After the preparation of a sufficiently flat and clean surface (see appendix A), mounds and pits were created by several cycles of sputtering (dose of ~ 5 ML equivalent of Ar^+ ions of 600 eV) at room temperature and subsequent annealing for 10 min to 523 K. At this low annealing temperature, the surface had sufficient mobility for the mounds and pits to reach their equilibrium shape but insufficient mobility for these structures to completely decay, thus restoring the flat surface. In fig. 3.1a several mountains and valleys can be seen, each of them several tens of monolay-

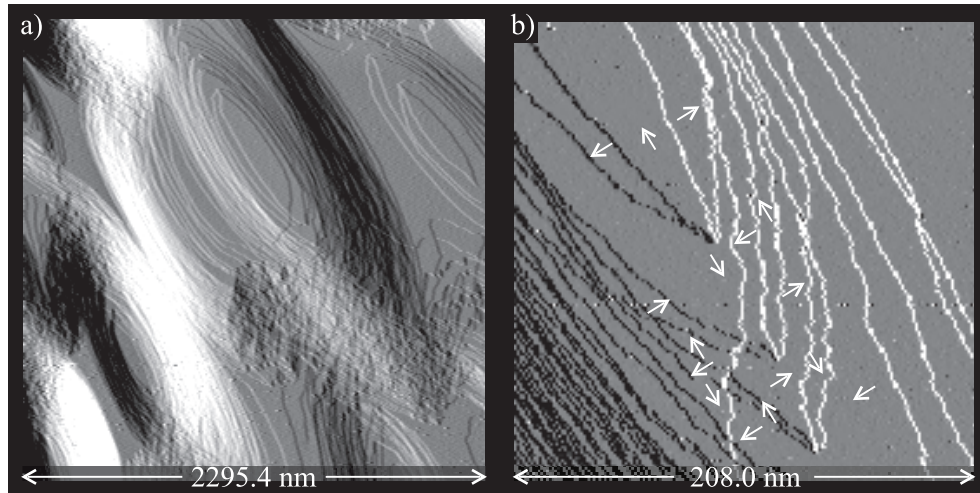


Figure 3.1: STM images (differentiated) of the artificially roughened Au(110) surface. (a) Mounds and pits have almond-like shapes with two sharp corners. (b) Illustration of the two possible corner configurations: crossing sites and termination sites. Arrows denote the four possible phases of the MRR (see text and fig. 3.2).

ers high/deep. All islands have an almond-like shape: curved sides joined at sharp corners.

3.1.2 Termination and Crossing Sites

Fig. 3.1b is an enlarged view of the corners at one side of a mound. Two different types of corners can be found. The first, where two steps seem to cross, we will refer to as *crossing sites*. The other type of corner is the location, where two pairs of steps reach the corner from the same side and end there; we call these *termination sites*. For an STM image of these two types of sites, in which the individual atom rows are resolved, see also fig. 2.7a. We find that on a misoriented (part of the) Au(110) surface the steps are organised in a *fish-scale* type network, consisting of crossing sites [79]. Termination sites accommodate the surface curvature. At each termination site, four steps are either introduced or removed, thereby allowing arbitrary changes in the misorientation.

The origin of the almond shape, the corner configurations, and the network structures lies in the (1x2) missing-row reconstruction of Au(110). Figure 3.2a shows a schematic cross-section of the reconstructed Au(110) surface. Along the [001]-direction every second surface atom row is missing (see also the top view in fig 2.6a). The simplest way to create an island on this surface would be to place extra Au atoms directly on the MRR surface. After filling the troughs, atom rows have to be added on top, whilst maintaining the MRR structure in the higher level. This naturally results in

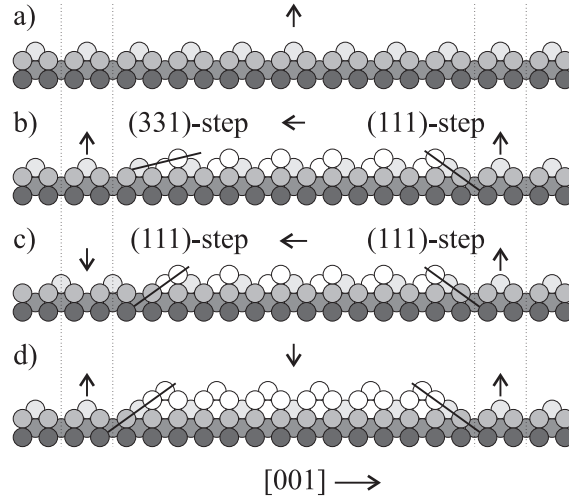


Figure 3.2: Schematic cross sections perpendicular to the MRR: (a) terrace; (b) adatom island with different steps on its two sides; (c) adatom island with only (111)-steps and a phase difference between left and right; (d) double-height island. The arrows denote the four possible phases of the MRR (see text).

non-equivalent steps on the two sides of the island parallel to the $[\bar{1}\bar{1}0]$ MR direction, which we denote as (111)- and (331)-steps, indicating the orientation of the two corresponding nanofacets (see fig. 3.2b). Unless the annealed surface is strongly pinned by defects, we never observe (331)-steps at room temperature. Artificial creation of (331)-steps is possible, as can be seen in chapter 6, but this results in metastable island structures. We conclude that the formation energy $E_{[\bar{1}\bar{1}0]}^{331}$ of (331)-steps is significantly higher than that of the (111)-steps, $E_{[\bar{1}\bar{1}0]}^{111}$.

We find that the surface resorts to an alternative island structure without (331)-steps. There are several ways for the surface to achieve islands with only (111)-type edges. One is to introduce a ‘phase shift’ in the reconstruction of the substrate. The mismatch between the positions of the atom rows of the MRR to the left and the right of an island with (111)-steps on both sides is shown in fig. 3.2c. The phase difference can easily be seen by comparing the atom row positions between the vertical lines in figs. 3.2 b and c. The missing row pattern on the left hand side of the island has been shifted by half of the missing-row period, equivalent to a 180° phase shift. At each (111)-step the missing row pattern shifts by one quarter of the regular missing row spacing, corresponding to a phase change of 90° . The four resulting phases [62] are indicated with arrows, see e.g. parts \downarrow , \leftarrow and \uparrow in fig. 3.2c. Descending a (111)-step from left to right, we rotate the arrow 90° clockwise, and descending a (111)-step from right to left, we rotate it 90° anti-clockwise.

An alternative way to accommodate islands without (331)-steps is to make all mounds and pits an even number of monolayers high or deep, as can be seen in

fig. 3.2d. However, we observe that Au(110) invariably chooses single-height island configurations with (111)-steps and a 180° phase shift in the lower layer (fig. 3.2c).

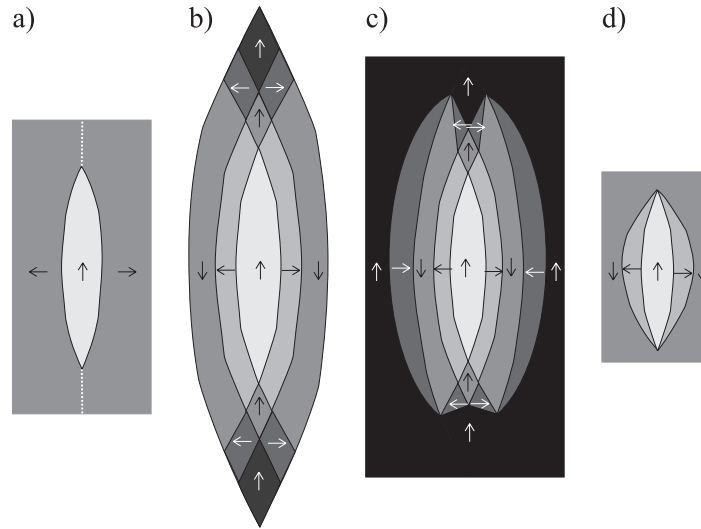


Figure 3.3: *Schematic top views: (a) single adatom island with domain boundary in the layer below (dotted line) (b) multilevel island without domain boundaries. (c,d) alternative multilevel islands without domain boundaries. Note that the steps always meet each other in groups of four. The arrows denote the four phases of the MRR (see text and fig. 3.2).*

One might expect that the island configuration discussed above would unavoidably lead to situations as sketched in fig. 3.3a, with domain boundaries between the phase shifted parts of the substrate. However, such configurations are *not* observed at room temperature. Instead, the steps always meet at crossing or termination sites, effectively reducing all domain boundary lengths to zeroⁱ. The ideal solution to avoid domain boundaries as well as high energy (331)-steps is to interconnect the islands in network structures (see fig. 3.3b). The phase changes in the network can be read off from the arrow rotations, introduced above. The combination of crossing sites that form the network, and termination sites that initiate, end or change the slope of the network (see figs. 3.3 c, d), provides the lowest-energy means to connect perfectly oriented parts of the Au(110)-surface, which are at different heights.

ⁱThis is not entirely true; small domain boundaries can be recognised at these sites, even at room temperature. In chapter 5 we will determine the creation energy of a domain boundary from their length distributions at such sites.

3.1.3 Determination of Absolute Step Energy Values

The shape of a two-dimensional island on a surface is completely determined by the orientation-dependent step free energy, as described in section 2.3, and from the island shape, usually, the (relative) step free energy can be deduced. To obtain information on the step formation energies from the shape of an island, one needs a description that relates the step free energy to the step formation energies.

The step edge of any island with the MRR can be built up as a combination of atomic length step segments (see also section 2.8). The three types of step segments on Au(110) are the [001]-step segment along the [001]-direction perpendicular to the MR structure, and the (111)-step segment as well as the (331)-step segment, both along the $[1\bar{1}0]$ -direction parallel to the missing rows. Their energies are denoted in this thesis by $E_{[001]}$, $E_{[1\bar{1}0]}^{111}$, and $E_{[1\bar{1}0]}^{331}$, and they are expressed per appropriate length units. For the [001]-direction this is the period of the MRR, which is twice the lattice parameter of gold, i.e. 8.16 Å. For the two step segments along $[1\bar{1}0]$, the length unit is the atomic spacing, of 2.88 Å. In our description, the energy of a step configuration is treated as a simple sum of step segment energies. We have ignored the possible contribution of *corner energies* [80]. Such additional energy terms may be expected to accompany each corner between a [001]-segment and a (111)- or (331)-segment. However, in chapter 6, we will show that corner energies are zero for the Au(110)-surface, and therefore we will neglect them here. Assuming further that step or kink interactions are negligible, it is possible to derive the step free energy for any step orientation by calculating the partition sum over all step configurations with that orientation, as will be done in chapter 4. Carlon and Van Beijeren (CB) [78] approximated the step free energy by allowing only step configurations with fluctuations in one direction, perpendicular to the MR direction, as outlined below. We will call this the *perpendicular fluctuation approximation*.

The high formation energy of the (331)-step has a major effect on the free energy of a step oriented along the [001]-direction, i.e. perpendicular to the MRR-direction. Such a step has a high free energy, even at high temperature, since it has great difficulty meandering. Meandering introduces both (111)- and (331)-regions along the [001]-step (see fig. 3.4), and the latter are high in energy. Assuming that (331)-step segments cannot be formed, so that steps along the [001]-direction can only be straight, CB computed the orientation-dependent, free energy of steps on Au(110) [78]. They found that the steps exhibit a distinct maximum in the free energy along [001]. This orientation plus a (temperature-dependent) range of step orientations around it, is expelled from the equilibrium island shape (see Wulff construction in fig. 3.5a). Consequently, the equilibrium island shape looks like an almond: each island contains two sharp corners where two (111)-type steps (with kinks) are joined under a well-defined angle, 2Φ . The angle, Φ , is determined by $E_{[1\bar{1}0]}^{111}$, $E_{[001]}$ and temperature. The two step energies can be obtained directly (see below) from a measurement of Φ versus temperature.

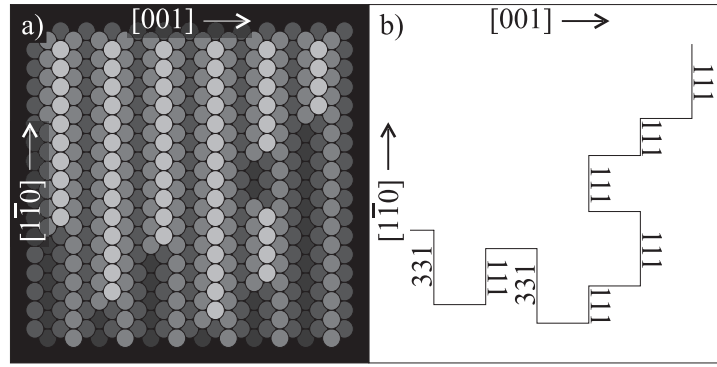


Figure 3.4: Two schematic representations of a step, showing that (331)-step segments are introduced when the [001]-part of the step is meandering along the $[1\bar{1}0]$ -direction: (a) atomic ball model (b) line model

An alternative to the perpendicular-fluctuation approximation is introduced in detail in chapter 4. Precisely the opposite assumption is made in this model, which we call the parallel-fluctuation approximation: the $[1\bar{1}0]$ -fluctuations perpendicular to the [001]-step are allowed explicitly whereas the [001]-fluctuations perpendicular to the $[1\bar{1}0]$ -step are ‘forbidden’. Chapter 4 shows that both approximations have a range of step orientations for which they are most appropriate; the perpendicular-fluctuation approximation is optimal for steps close to the perfect $[1\bar{1}0]$ -orientation, while the parallel-fluctuation approximation is best for steps close to the [001]-orientation. Given the step energy values $E_{[1\bar{1}0]}^{111}$, $E_{[1\bar{1}0]}^{331}$ and $E_{[001]}$ for Au(110), determined in this thesis [81], the parallel-fluctuation approximation best describes the step free energy over almost the entire angular range from [001] to $[1\bar{1}0]$. In chapter 4 we demonstrate that it is possible to apply the step free energy results of the anisotropic 2-dimensional Ising model to the specific case of Au(110). This model accounts for fluctuations in both directions. The calculations confirm the validity of the parallel-fluctuation approximation for almost the entire range of step orientations. Figure 3.5b shows that the equilibrium shape calculated for the parallel-fluctuation approximation can be made very similar to that for the perpendicular-fluctuation approximation, albeit for different step energies.

The step energies, $E_{[1\bar{1}0]}^{111}$ and $E_{[001]}$, used for the calculations in figs. 3.5 a and b correspond to the best fits for each of the applied approximations to the observed shapes. In particular, we have tried to make use of the measured angles, Φ at *crossing sites*, found in mounds and pits, imaged at temperatures ranging from 300 to 394 K. However, the angles were measured to range from 8° to 32° . This large variation in Φ is not due to measurement errors or random statistical variations in the island shape. It reflects the fact that islands with crossing sites at both sharp corners do not exhibit one unique, size-independent, equilibrium shape, because each individual

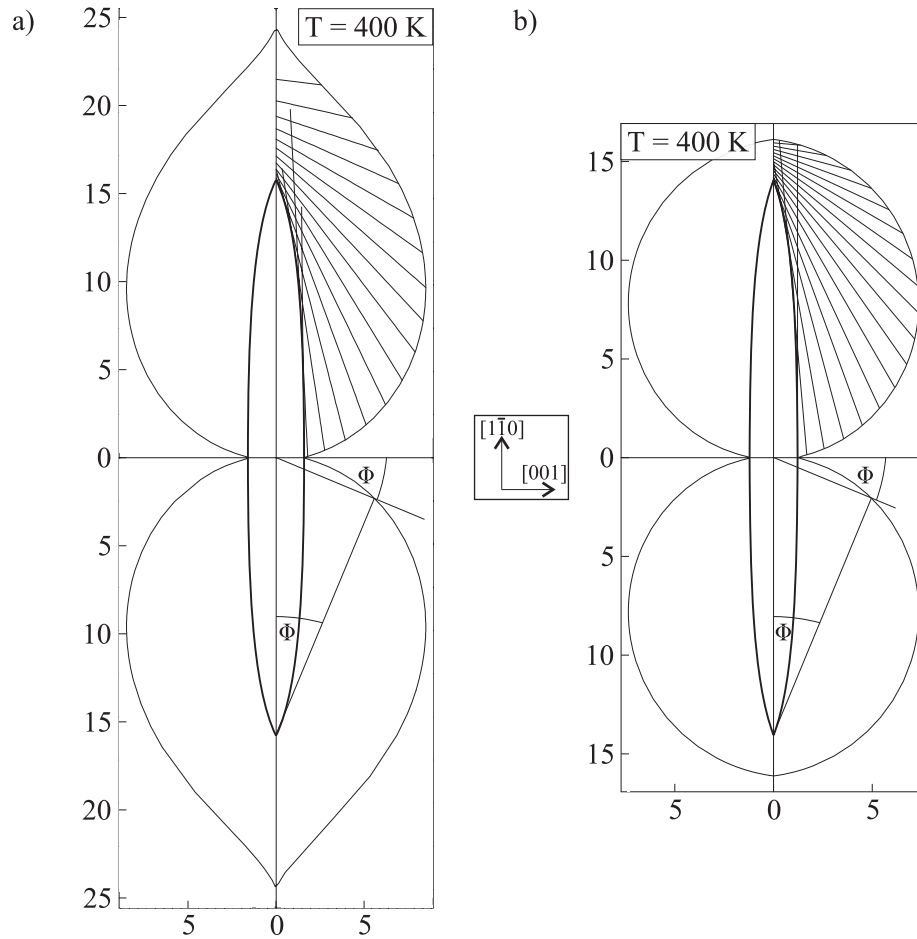


Figure 3.5: Two-dimensional Wulff constructions based on the step free energy (thin line) of an adatom or vacancy island (thick line). $E_{[001]}$ has been set to 200 meV per MRR period in both calculations. Steps with angles larger than $\Phi = 22.6^\circ$ are expelled from the equilibrium shape: (a) calculated via Carlon et al. [78] for $E_{[1\bar{1}0]}^{111} = 4.7$ meV per atom spacing; (b) calculated via the parallel-fluctuation approximation of chapter 4 for $E_{[1\bar{1}0]}^{111} = 3.7$ meV per atom spacing. The step free energies in both figures are expressed in eV/Å. The directions of the $[1\bar{1}0]$ and the $[001]$ steps are indicated by the arrows.

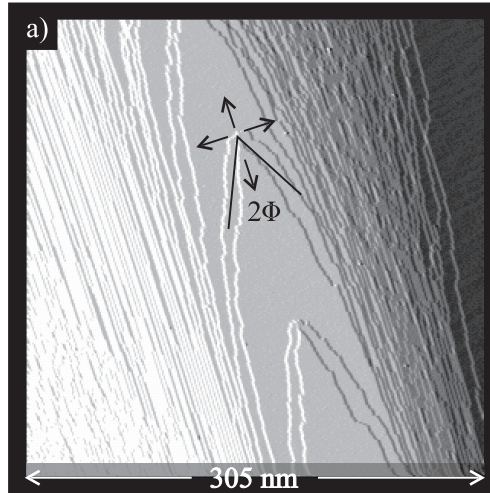


Figure 3.6: Large scale STM image of a termination site at 343 K. The arrows denote the freedom of this site to move in any direction, in order to adopt the lowest free energy configuration.

almond cannot optimise its shape independently from the network. We will return to this point in section 3.2.

Fortunately, a termination site has the freedom to move in all directions (see fig. 3.6), so it can easily adjust itself to minimise the total free energy. Generally, two steps of the same type (up/down) placed next to each other repel, whereas opposite type steps placed next to each other can either attract or repel (see section 2.5). Almost all step combinations on Au(110) repel each other (chapter 5), so we expect the angle Φ to be slightly too large in comparison with the equilibrium angle calculated without such repulsion. However, the average angle formed by all 4 steps should be close to the value without step interaction, because of the partial cancellation of the different repulsive forces. We have measured the average angle at *termination sites* between 345 and 470 K. Below 345 K, the surface mobility was too low to allow equilibration of the angle within half a day. Above 470 K, the thermal fluctuations were too large to allow reliable STM measurements of the step angles. Between these temperatures, the measured angles did not exhibit the large variation found for the crossing sites. The measured angles, Φ , are shown in fig. 3.7.

The angles were initially analysed by fitting the perpendicular-fluctuation approximation to these measurements (fig. 3.7a), with $E_{[1\bar{1}0]}^{111}$ and $E_{[001]}$ as fitting parameters. We obtain $E_{[1\bar{1}0]}^{111} = 4.7 \pm 0.5 \text{ meV/atomic spacing}$ for almost all choices of $E_{[001]}$.ⁱⁱ The average value of the angle over the accessible temperature range is almost exclusively determined by the (111)-step energy. From the best-fit results we obtain

ⁱⁱCB express all step energies per lattice constant (l.c. = 4.08 Å): $E_{[1\bar{1}0]}^{111} = 6.7 \pm 0.7 \text{ meV/l.c.}$.

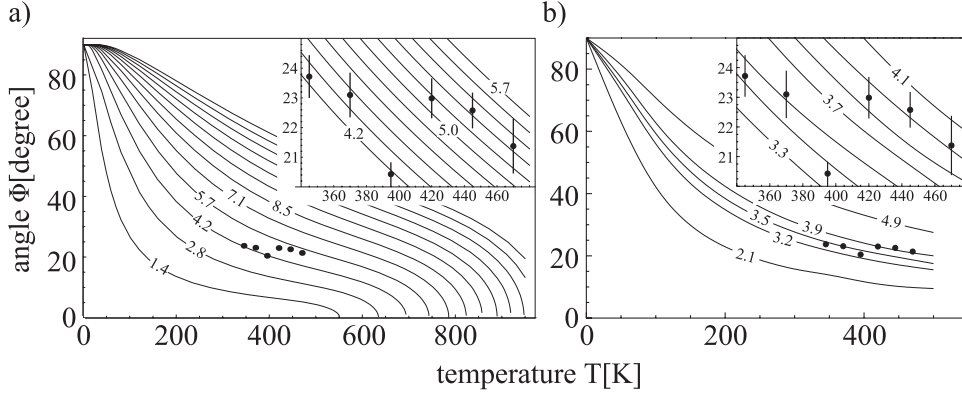


Figure 3.7: Angles, Φ , of termination sites (circles). Curves are calculated for the best-fit value $E_{[100]} = 200 \text{ meV/MRR period}$ and different values for $E_{[1\bar{1}0]}^{111}$ in $\text{meV/atomic spacing}$ (see numbers on the curves): (a) using the perpendicular-fluctuation approximation (b) using the parallel-fluctuation approximation.

$E_{[001]} = 200 \text{ meV/MRR period}$, which is only a rough estimate, since variations in the [001]-step energy only result in minor slope variations of the curves in fig. 3.7a around 400 K. To derive an error margin for the [001]-step energy, we plot the equilibrium angle, Φ , as a function of temperature (fig. 3.8a) for different $E_{[001]}$ energies (and a fixed (111)-step energy of $E_{[1\bar{1}0]}^{111} = 4.7 \text{ meV}$). From this we obtain a lower estimate: $E_{[001]} \geq 140 \text{ meV}$. As the aspect ratio of the almonds (defined as the length between the crossing sites along the $[1\bar{1}0]$ -direction divided by the maximum width measured along the [001]-direction) depends strongly on the [001]-step energy, we can also obtain an (upper) estimate for $E_{[001]}$ from the aspect ratio. But, we are faced with the problem that the islands in the networks show a substantial variation in shape, which we already saw in the variation in crossing angles. Here, we circumvent this difficulty by analysing those top-level islands whose crossing angle, Φ , was approximately equal to the value measured for the termination sites. For those top-level islands, the aspect ratio was found to be 8.5 ± 1.5 . This range is indicated by the shaded band in fig. 3.8b together with the calculated aspect ratios for different $E_{[001]}$ as a function of temperature. From this we obtain an upper limit $E_{[001]} \leq 220 \text{ meV/MRR period}$. We combine the two estimates to a final best fit value of $E_{[001]} = 200 \pm 60 \text{ meV/MRR period}$.

We are left with a dilemma: the step energies obtained by the perpendicular-fluctuation approximation fit lie outside the range, over which the perpendicular-fluctuation approximation is valid. In the perpendicular-fluctuation approximation the lowest formation energy for an (allowed) fluctuation perpendicular to a $[1\bar{1}0]$ -step is equal to $2E_{[001]}$, i.e. 400 meV, whereas the lowest energy for a (prohibited) fluctuation perpendicular to a [001]-step would be $E_{[1\bar{1}0]}^{111} + E_{[1\bar{1}0]}^{331} = 19 \text{ meV}$ (see

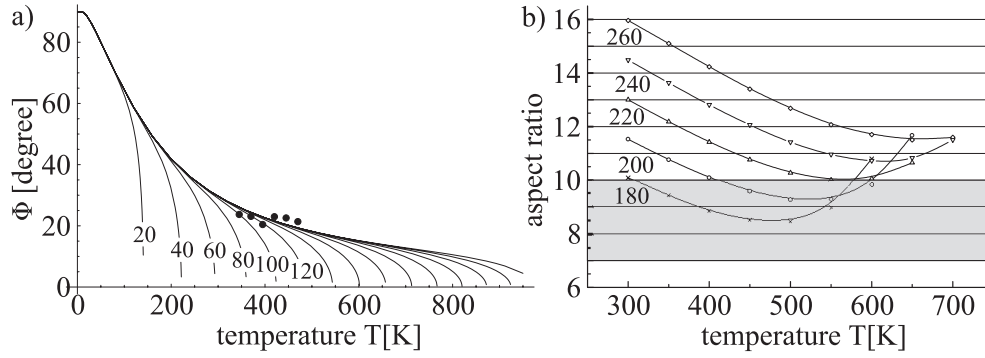


Figure 3.8: Graphs of (a) the equilibrium angle Φ and (b) the aspect ratio of the almonds as a function of temperature for different $E_{[001]}$ -step energies as indicated on the curves (meV/MRR period). For all curves $E_{[1\bar{1}0]}^{111} = 4.7$ meV/atomic spacing. The shaded band in (b) indicates the aspect ratio measured from (selected) almonds (see text).

table 2.2, [70]). From these numbers it is evident that precisely the opposite approximation would be more appropriate: i.e. $[1\bar{1}0]$ -steps are ‘always’ straight and fluctuations are allowed only in the $[001]$ -steps. This is precisely the situation described by our parallel-fluctuation approximation. Figure 3.7b shows the Φ -measurements with fits from the parallel-fluctuation approximation. Again, we find that the (111) -step energy can be fitted almost independently from $E_{[001]}$. The best fit result from this approximation is $E_{[1\bar{1}0]}^{111} = 3.7 \pm 0.5$ meV/atomic spacing and $E_{[001]} = 200$ meV/MRR period.

Also within the parallel-fluctuation approximation, we cannot derive a lower estimate for the $[001]$ -step energy similar to the situation encountered for the perpendicular-fluctuation approximation. This is because the equilibrium shape (see fig. 3.5b) is dominated by the step orientations around $[1\bar{1}0]$, and in this model the $[1\bar{1}0]$ -step has no entropy. Once again, we use the measured aspect ratio (shaded band in fig. 3.9) to obtain an upper estimate of $E_{[001]}$. The curves in fig. 3.9 represent calculated equilibrium aspect ratios for islands with different $E_{[001]}$ values. The length of the islands was obtained from the parallel-fluctuation approximation, whereas the width of the islands was calculated using the $[1\bar{1}0]$ -step free energy from the perpendicular-fluctuation approximation. In chapter 4 we verify that this approach represents the true equilibrium aspect ratio by calculating the exact step free energy via the two-dimensional Ising model. From this we obtain an upper estimate for $E_{[001]}$ of 200 meV/MRR period. The vertical lines indicate the temperatures where the (111) -step free energy vanishes in the perpendicular-fluctuation approximation. These temperatures can also be calculated directly via

$$f = -kT \cdot \ln Z$$

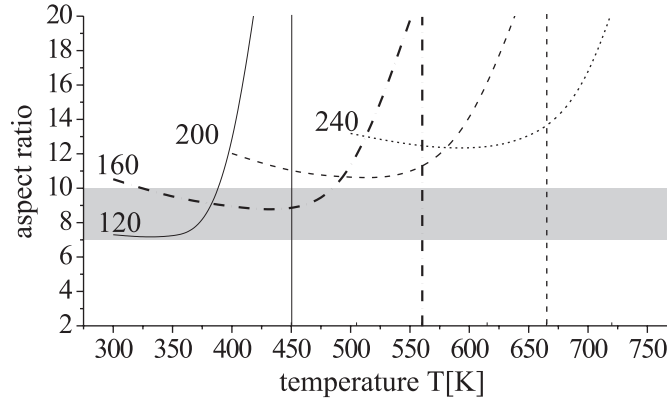


Figure 3.9: Aspect ratio (calculated by the proper combination of the two approximations, see text) as a function of temperature. For all curves, $E_{[1\bar{1}0]}^{111} = 3.7$ meV/atomic spacing. The $E_{[001]}$ values in the figure are expressed in meV/MRR period. The vertical lines denote the temperatures where the (111)-step free energy vanishes for each curve. The shaded band indicates the experimental aspect ratio.

$$= -kT \cdot \ln \left(e^{-E_{[1\bar{1}0]}^{111}/kT} \left(1 + 2e^{-E_{[001]}/kT} \right) \right) = 0 \quad (3.1)$$

The temperature at which the (111)-step free energy vanishes should be comparable to the roughening temperature (see section 2.4). As we raise the temperature to this point, the equilibrium value of the aspect ratio increases rapidly. From the experimental transition temperature, $T_r = 815 \pm 50$ K (see table 2.2 and [64, 82]), we can obtain a lower estimate for $E_{[001]}$ of 240 meV/MRR periodⁱⁱⁱ. Since 200 meV/MRR period was the best fit value for fig. 3.7b, we obtain a final value for $E_{[001]}$ of 200 ± 60 meV/MRR period.^{iv} Combining the fitting result for $E_{[1\bar{1}0]}^{111}$ with $E_{[1\bar{1}0]}^{111} + E_{[1\bar{1}0]}^{331} = 19$ meV, we calculate $E_{[1\bar{1}0]}^{331} = 15.3 \pm 1.5$ meV/atomic spacing. The large energy difference between $E_{[1\bar{1}0]}^{331}$ and $E_{[1\bar{1}0]}^{111}$ explains, why the surface avoids (331)-step configurations.

3.2 Dynamics of the Islands and the Networks

At all elevated temperatures, at which there was sufficient mobility, we observed a gradual, layer-by-layer removal of the artificially created mounds and pits on Au(110). The smoothening process revealed two anomalous phenomena. Each island undergoes a dramatic shape change while shrinking in size, which is very different from the

ⁱⁱⁱThe possible influence of the deconstruction transition is neglected.

^{iv}This error margin ensures that $T_r = 815$ K can be reached.

usual observation of size-independent equilibrium shapes (section 2.3). During the disappearance of the topmost atomic layer, the layer below splits into two separate parts. Both effects can be seen in fig. 3.10a, which shows the topmost three atomic

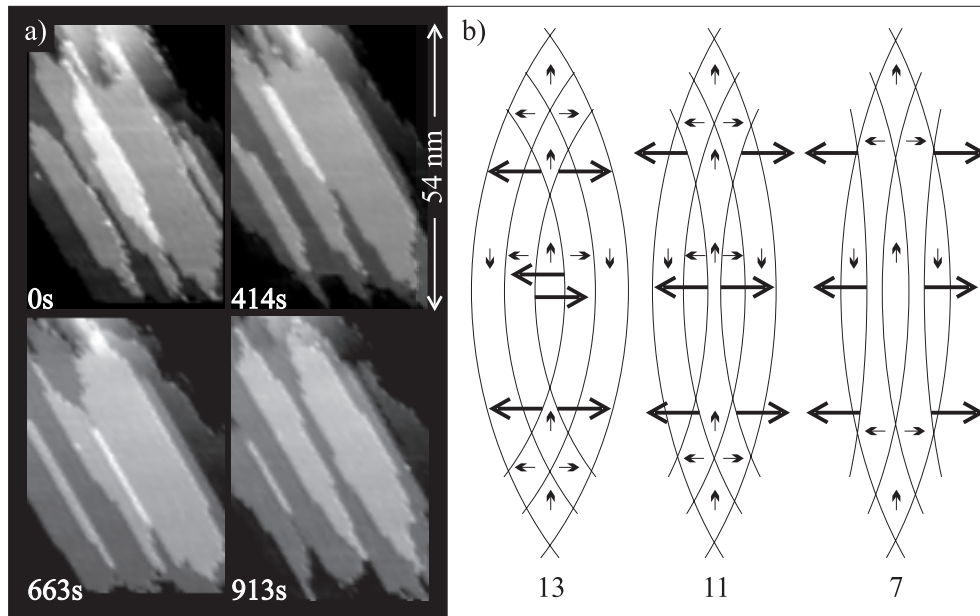


Figure 3.10: *Disappearance of the topmost level of a mound. (a) STM images at 394 K. The island narrows and when it disappears the layer below splits into 2 parts. (b) Schematic representation of the process. The steps recede in the directions indicated by the bold arrows, thereby reducing the area of the topmost terrace (left). When the topmost terrace has disappeared, the terrace below divides in two (middle). As this second level disappears the process repeats itself (right). The number of terraces is indicated below each configuration.*

levels of a mound at 394 K at four stages in its evolution. Between the third and the fourth image the topmost terrace disappears completely. We will discuss the unusual decay behaviour in the following subsections.

3.2.1 Network Structure Effects

We observe the unusual lower layer splitting for every terrace that disappears on Au(110). Once again, the explanation lies in the MRR. As was illustrated in figs. 3.2c and 3.3a, a phase difference exists between the regions on the left and the right of the layer below the disappearing island.

When the upper terrace decreases, the newly exposed terrace has to split in two, forming two new (111)-steps, to prevent a domain boundary from being left behind. This process is illustrated in fig. 3.10b. After the top level island has disappeared, the

step configuration still satisfies the ‘rules’ discussed before for the crossing sites, as can be verified by the arrow rotations in fig. 3.10 (compare with fig. 3.3). At first sight it might seem that subsequent splitting of lower and lower levels would increase the density of steps and terraces on the surface. However, as a terrace disappears, two terraces (one at each apex of the disappearing island) merge with the layer below the island, reducing the total number of terraces by 2 (see fig. 3.10b). This intricate configuration also maintains the correct MRR phases across the whole mound. The network can be described as a *set of extended, curved steps that cross* at the crossing sites. The removal of the topmost terrace can be regarded as a decrease in curvature of the steps and/or an outward motion of the two steps that define that terrace. It is clear that this description completely invalidates the independent-layer description of multilayer structures, mentioned in section 2.3, but to what extent this is reflected in the decay of the islands has not been pursued in the present study.

3.2.2 Shape Change

In addition to the layer splitting, the topmost islands undergo a dramatic change in shape during their evolution (see fig. 3.10a). First the islands become increasingly narrow, and finally they lose their almond shape completely, forming a narrow strip of one or a few close-packed atom rows that reduces in length until the island is completely removed. This behavior was observed for all disappearing islands on Au(110).

The shape change was quantified by measuring the island’s aspect ratio. Figure

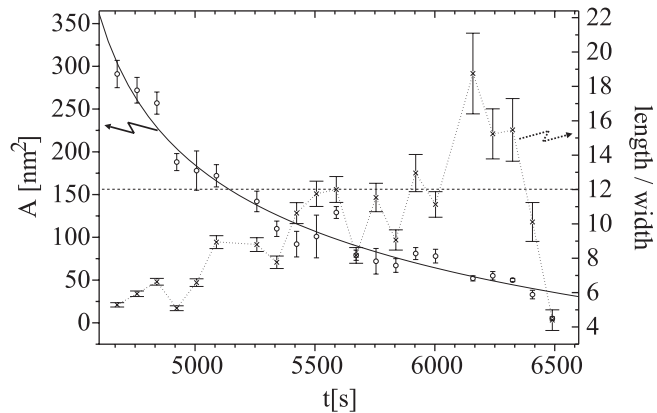


Figure 3.11: *Measured evolution of the upper terrace of a mound. The terrace area (left axis) is indicated by circles, and the aspect ratio (right axis) by crosses. The solid curve shows a power law fit with a time exponent of $-1/2$. The dotted horizontal line indicates the equilibrium angle of $\Phi = 12^\circ$ at $T = 394$ K.*

3.11 shows the typical evolution of the area and the aspect ratio of a terrace, from the

point of its formation (i.e. the time when it becomes the topmost terrace as a higher terrace disappears) to the point of its own disappearance. As the island reduces in size, the aspect ratio increases from an initial value of 5.5 to a maximum of 19 at $t \simeq 6200$ s. The trend deviates from a smooth curve every time that the loss of a complete atom row results in an abrupt change of the aspect ratio. Beyond 6200 s, the aspect ratio quickly drops and the island disappears.

The (calculated) equilibrium aspect ratio for islands at 394 K is 12 (see fig. 3.9), which has been indicated by the dotted line in fig. 3.11. At times between 5000 and 6000 s, the aspect ratio of the decaying island lies very close to this equilibrium value. However, there is no clear indication, during the total evolution period, that the island adopts the equilibrium almond shape, characteristic of an isolated, infinitely large island in equilibrium with a reservoir of Au adatoms. This probably explains the large spread of corner angle measurements, 2Φ , in the network structure, described in subsection 3.1.3, and makes an analysis of the network angles (in terms of step free energies) impossible. Probably, only islands with termination sites at *both* sharp corners show the proper aspect ratio, irrespective of their size.

We observe that during the mound evolution (see fig. 3.10b) there is a preference for the formation of two new steps instead of one domain boundary. This would suggest that $2E_{[110]}^{111} < E_{DB}$, where E_{DB} is the domain boundary energy per atomic spacing. However, in chapter 5 we prove that this inequality is invalid. Why, then, do the islands split?

We can explain the step formation and the variation in shape qualitatively by the use of the description introduced in the previous subsection. We start by recognising that the steps organise in networks in which they (appear to) cross each other. If the elastic and entropic forces between steps, close to the point where they cross, are not too high, we should expect the steps to cross without slope discontinuities. This inescapably implies that none of the levels in a mound, not even the topmost one, is free to optimise its own shape independently of the other levels with which it is connected via its own two steps. Within this framework, the decay of a mound should indeed proceed as sketched in fig. 3.10b. The two subsets of steps, those curved to the left and those curved to the right, slowly translate in opposite directions. In addition, there can be gradual changes in the step curvature, but we will ignore this possibility for the moment.

Let us now consider the topmost level of a decaying mound. If both steps, enclosing that level, have a more or less constant radius of curvature r , the aspect ratio, length l over width b , is given by $\frac{l}{b} = 2\sqrt{\frac{r}{b} - \frac{1}{4}}$, which monotonically increases as b is reduced, and diverges for vanishing b . Although this correctly predicts the observed trend, it leaves several questions unanswered. For example, the initial value of l/b is smaller than the equilibrium value for an isolated island, indicated by the horizontal, dotted line in fig. 3.11. Furthermore the aspect ratio does not diverge, but it reduces to zero during the final stage of the island's decay. We can understand both

observations on the basis of $E_{DB} < 2 \cdot E_{[1\bar{1}0]}^{111}$.

During the final stage of the island decay, the long island is bounded by two steps, of which the orientations are closer and closer to $[1\bar{1}0]$ over the entire length of the island. When the average width of the island reduces to small values, between one and two MRR periods, the island can reduce its free energy by narrowing down to a single atom row (fig. 3.10a), which makes it a domain boundary (‘solid wall’, see chapter 5).^v The domain boundary is removed by splitting the lower layer and creating two new (111)-steps, but, as this splitting is an endothermic process, an additional driving force is required. This probably results in a temporary, extra high curvature of the in the step network extended two steps. Consequently, the aspect ratios of the two newly formed islands, immediately after their formation, are expected to be lower than the equilibrium value.

In the description of the mound configuration as a network of curved lines that cross each other without slope discontinuity, the maximum angle at which each line is allowed to run, anywhere on the mound, should be equal to Φ (see section 3.1.3). All step directions with higher angles are expelled from the equilibrium shape. This maximum angle can occur only at the base of the mound, rather than at the top or at intermediate positions in the network (cf. figs. 3.3 and 3.10).

3.2.3 Scaling Behaviour of the Island Decay

We investigated the relationship between the shape and the time dependence of the island decay. Figure 3.11 shows that the island area, A , decays more slowly than linearly in time until the island reaches its maximum aspect ratio, when the decay rate speeds up. This behavior differs from the typical forms of island decay [49, 51], discussed in section 2.7 (see fig. 2.5).

It has been shown that differences in diffusion barriers, e.g., on Ag(110) can lead to an anisotropic, and even one-dimensional island decay [83] at low temperatures. On the Ag surface the activation barriers for all processes along the $[1\bar{1}0]$ -direction are lower than their counterparts along the $[001]$ -direction. Therefore the Ag islands decrease in length along $[1\bar{1}0]$ whilst maintaining their width along $[001]$. On Au(110) the fast diffusion direction is also $[1\bar{1}0]$, but the islands on Au(110) decrease predominantly in width, which shows that the mobilities are high enough also in the $[001]$ -direction not to limit the shape of the island.

As the observed length changes are almost always much smaller than the width changes on Au(110) (see fig. 3.10a), we model the decay as follows. The island shape is again described as the area, A , enclosed between two equally large, intersecting circles with a fixed distance, L , between the intersection points (see fig. 3.12). For large r it can be shown that $A \sim r^{-1}$. To model the decay, we increase the circle

^vOnce the island has reached this stage, it can lose atoms only by reducing its length. This is why the aspect ratio decreases prior to the disappearance of the island.

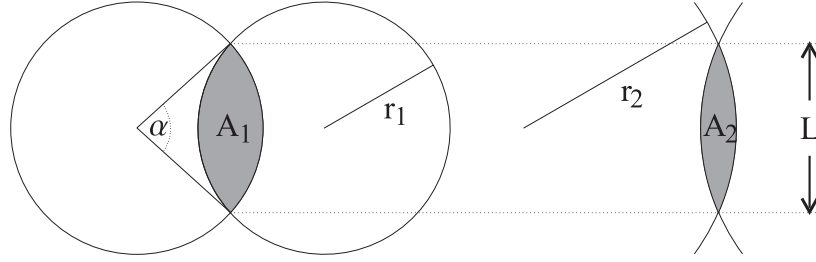


Figure 3.12: Schematic representation of our model: the area A of an island is defined by the intersection of two equally large circles. We describe the decay of A as an increase in the radii (from r_1 to r_2), assuming that the length L of the almonds remains unchanged.

radii. The corresponding reduction in step curvature causes a lowering of the two-dimensional adatom equilibrium pressure of the islands, i.e. the density of atoms on the surrounding terraces for which the island size would remain constant. As a result the decay rate of the island slows down, as it shrinks.

The time dependence of the decay was calculated directly, using the method described in section 2.7. For this purpose an additional geometrical factor must be introduced in eq. 2.4: $\frac{\alpha}{2\pi} = \frac{1}{\pi} \arcsin\left(\frac{L}{2r}\right)$, which describes the difference between a complete circle and the circle section subtended by an angle α (fig. 3.12). The evolution of the model islands with time is therefore given by:

$$t - t_0 \sim \int \left(4r \arcsin\left(\frac{L}{2r}\right) - \frac{2L}{\sqrt{1 - \left(\frac{L}{2r}\right)^2}} \right) \frac{\lambda(r)}{\arcsin\left(\frac{L}{2r}\right)} dr \quad (3.2)$$

Here, t_0 is *not* the time at which the island disappears but rather the time at which it starts its decay. The variable λ reflects the active transport mechanism: $\lambda = r$ in the diffusion limited case, and $\lambda = 1$ in the attachment limited case. By solving this equation for $L \ll r$ (corresponding to an almond shape) the *dominating* term at large r becomes r^5 in the diffusion limited case and r^2 in the attachment limited case. When we fit the models for these two limiting cases to the first part of the decay in the experimental data, we obtain fits with ‘no’ significant difference in quality and appearance: the normalised goodness of the fit are $\chi^2(\text{diffusion limited}) = 3.00$ and $\chi^2(\text{attachment limited}) = 2.95$. Figure 3.11 only shows the attachment limited curve, with $r \sim (t - t_0)^{1/2}$ and $A \sim (t - t_0)^{-1/2}$. On the basis of these results, no further conclusion can be drawn on whether the decay is diffusion or attachment limited.

Beyond the point where the island reaches its maximum aspect ratio, our model breaks down. This is because the island length can no longer be treated as constant. Instead, the step curvature increases rapidly, and therefore the decay rate should increase dramatically, as indeed is observed in fig. 3.11.

Now we can understand the observation (made during the sample preparation in appendix A) that it takes such a long time to smoothen a Au(110)-surface and that, once it has been made rough, we had to mechanically repolish it after the initial sputtering and annealing cycles. This is because the time dependence deviates from the usual linear or $(t_0 - t)^{2/3}$ time dependence (section 2.7), due to the decrease in step curvature of the islands.

Recent STM observations of Pt(110), which also has a (1x2) MRR allow us to speculate on an additional energy lowering effect for the almond mounds and pits. Pt(110) shows a large-scale corrugated-iron structure [84, 85, 86, 87], consisting of quasi one-dimensional islands with a length of more than $5\mu\text{m}$ in the $[\bar{1}\bar{1}0]$ -direction. These are formed by many, almost perfectly straight (111)-steps. This structure is believed to be stable, because the energy gain that is involved in the release of surface stress outweighs the step formation energy. Since the almonds spontaneously decay, we know that the formation energy of the steps is too high for this on Au(110). However, the formation energy of the almonds may be reduced somewhat due to stress relaxations, thereby reducing the rate of the spontaneous almond decay even further.

3.3 Summary and Discussion

We have seen that the equilibrium shape of islands and pits on the Au(110)-surface is almond-like: each island contains two smoothly curved steps joined at two sharp corners. This originates from the MRR, as had been theoretically predicted prior to this work. The network structure (the so called *fish-scale-pattern*) is the ideal way to connect all the perfectly oriented parts of the Au(110)-surface to each other (see fig 3.13). This is because it makes the surface avoid creating high energy (331)-steps and domain boundaries. In particular, the combination of termination sites and crossing sites in the network structure allows the surface to overcome any height variation. The decay behaviour of such islands revealed that neither the almonds nor the networks connecting them have to exhibit the equilibrium angle Φ expected for an isolated island, which is not connected to a network. The usual *independent layer* behaviour cannot take place on this surface, as the terraces on Au(110) cannot adopt their shape *independently*. The crossing sites naturally connect individual layers even when they are separated by large distances. Therefore we never can treat the individual levels as two-dimensional independent islands placed on top of each other; they always represent part of a three-dimensional object. Since a termination site can move freely on the surface to its lowest (free) energy position, it is the only candidate structure whose angle is free to become equal to the theoretical equilibrium value Φ . By measuring this angle at different temperatures we determined the step formation energy of a (111)-step as $E_{[\bar{1}\bar{1}0]}^{111} = 3.7 \pm 0.5\text{meV}/\text{atomic spacing}$ and of a [001]-step as $E_{[001]} = 200 \pm 60\text{meV}/\text{MRR period}$. Combining our results with those from Hoogeman et al. [70] we calculated the (331)-step energy to be $E_{[\bar{1}\bar{1}0]}^{331} =$

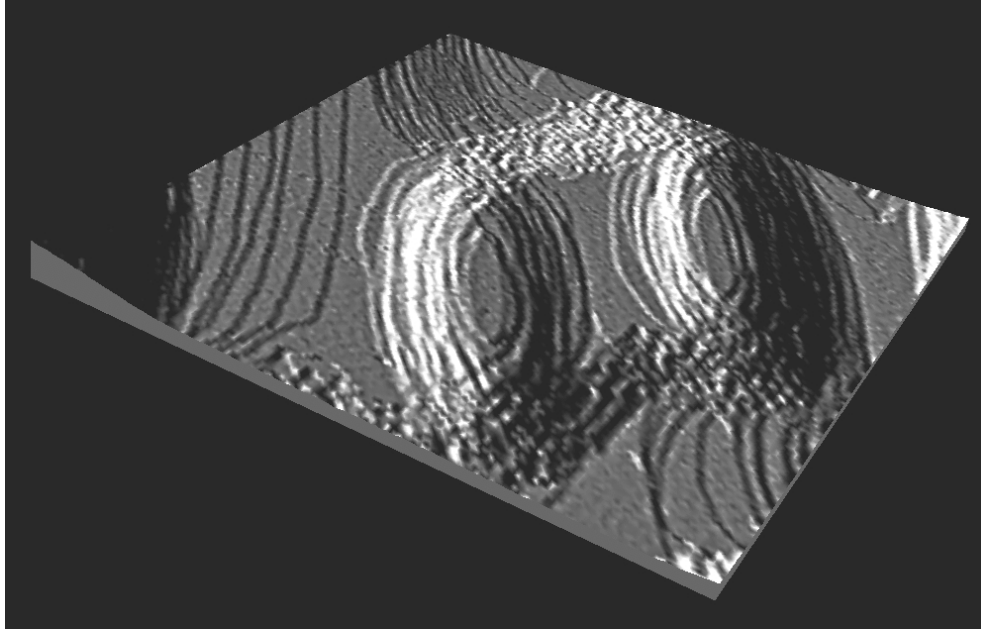


Figure 3.13: *STM image (perspective view combined with artificial illumination) illustrating the connection between different perfectly oriented parts of the Au(110)-surface via the network structures (size: $0.96\mu\text{m} \cdot 0.96\mu\text{m}$).*

15.3 ± 1.5 meV/atomic spacing.

In addition we found that an island undergoes a dramatic shape change during its decay and that the layer below the disappearing island splits into two disconnected regions. The shape change of the disappearing island leads to a slowed down decay dynamics. This has dramatic consequences for the time needed for a Au(110)-surface to smoothen out height differences.

Table 3.1 compares the (111)-step and (331)-step energies determined in this experiment with the values calculated with the embedded atom method (EAM) [71]. Although the order of magnitude of these numbers are similar, and the ratios

method	$E_{[1\bar{1}0]}^{111}$	$E_{[1\bar{1}0]}^{331}$
Exp.	3.7 ± 0.5 meV/a.s.	15.3 ± 1.5 meV/a.s.
EAM	1.8 meV/a.s.	9.5 meV/a.s.

Table 3.1: *Comparison of the (111)-step and (331)-step energy values obtained from this experiment and from the embedded atom method [71].*

$E_{[1\bar{1}0]}^{111} / E_{[1\bar{1}0]}^{331}$ are approximately equal, the EAM values are almost a factor two below the experimental ones. One debatable step in the analysis leading to the experimental

value for $E_{[1\bar{1}0]}^{331}$ was implicit in the assumption that the adatom row energy, measured by Hoogeman et al. [70], can be equated to the sum $E_{[1\bar{1}0]}^{111} + E_{[1\bar{1}0]}^{331}$ (see table 2.2). We may expect that the adatom row energy is in fact different than the sum of the two step energies, since extra relaxations, and step-step interactions have to be taken into account.

As mentioned in subsection 3.1.3 we would have to choose the [001]-step energy higher than 240 meV/MRR period, in order to predict the proper roughening transition temperature, while we would have to choose it below 200 meV/MRR period, in order to predict the proper island aspect ratios. However, since our model does not include the possibility for the surface to deconstruct (subsection 2.8.2), the prediction for the roughening transition temperature should be taken with caution, and more weight should be given to the aspect ratios.

Given our understanding of crossing sites, the breakdown of the ‘independent’ terrace description, and the observed (slowed down) annealing behaviour of the almonds, we treated a step, such as those shown in fig 3.13, which e.g. runs along the right side of one almond (mountain) through the network structure to become a step on the left side of another almond (valley), as a macroscopic structure. In comparison with the usual step dynamics on normal surfaces, the question arises whether similar dynamics should still be expected for the steps on Au(110) on a macroscopic scale. Can we treat them as independent, freely moving, one-dimensional objects? Or, is their diffusion strongly influenced by the crossing sites? Observations of the dynamic behaviour of the network structures on a large length scale should give the answer.

We expect that the phenomena reported here are not exclusive to Au(110), but that they also occur on (110) surfaces of other *fcc* materials that exhibit a missing-row reconstruction. Examples of these are clean Pt(110) and Ir(110).

It is known that CO-adsorption on Pt(110) lifts the MRR [88] and that H-adsorption on Cu(110) forces a MRR [89]. These two systems could enable a study of the formation and disappearance of networks and almonds induced by changes in the gas pressure or composition.

Finally, our findings for the shapes of islands on Au(110) raise questions concerning the three-dimensional equilibrium shape of a gold crystal. The perfect (110)-facet is connected at two sharp corners with two step networks. At these points the steps cross each other and the *individual terrace* description is no longer valid. If we move away from the (110)-surface, by rotating around [001], into the direction of a (100)-surface, the region of crossing steps has to be connected somehow to an ‘individual-layer’ surface without crossing steps. Since the three-dimensional crystal contains only one almond shaped mountain per (110)-orientation and since the density of crossing steps has to be increased the more we approach the (100)-surface, it is impossible to terminate the steps with termination sites, as described in subsection 3.1.2. Therefore, we expect interesting, structural transition regions between (110) and other surface orientations.

Chapter 4

Theory for the Symmetric Almonds

Step free energy and Wulff construction

In this chapter, we use a simple terrace-ledge-kink description, adapted to the specific case of the missing-row reconstruction of Au(110), to calculate the orientation dependent step free energy on this surface. We show that it is possible to perform this calculation exactly, in the framework of the two-dimensional Ising model. In addition, we treat two simplifying approximations, namely the so-called parallel fluctuation model, which allows steps to contain shape fluctuations only parallel to the missing rows, and the perpendicular fluctuation model, previously introduced by Carlon and van Beijeren [78], which allows only shape fluctuations in the direction perpendicular to the missing rows.

Equipped with these three formalisms for the step free energy, we perform the Wulff construction and discuss the resulting, temperature-dependent equilibrium shape of the almond-shaped islands on Au(110). Finally, we compare the analytically obtained step free energies with those obtained by Monte-Carlo simulations.

4.1 Step Free Energy

In chapter 3, we have used two different models for the step free energy on Au(110) to compute the shape characteristics of almond-shape island structures on this surface and to fit these to the shapes that we observed experimentally. The step energies that we obtained from these fits were found to lie outside the range for which one of these models, the perpendicular fluctuation approximation, is valid. The other model, the parallel fluctuation approximation, was concluded to be much more appropriate.

To calculate the equilibrium shape of islands on Au(110) we have to know the free energy, f , per unit length of an infinitely long step, for all step directions. In this chapter we derive expressions for the orientation-dependent step free energy $f(\phi)$ for a simple model of the Au(110)-surface, in which the formation energy of every step configuration is a simple sum of energies of individual step segments along the [001] and $[1\bar{1}0]$ directions.

We first describe how to obtain $f(\phi)$ for a surface with rectangular symmetry from the step free energy for square symmetry. By applying the result to the special case of Au(110), which has two different types of steps along $[1\bar{1}0]$, we separate f into the ground state energy and the free energy contribution stemming from fluctuations in the step position. Finally, we derive an explicit expression for $f(\phi)$ within the two-dimensional Ising model as well as the two different approximations mentioned above, each of which ignores fluctuations along one particular direction.

4.1.1 From a Square Lattice to a Rectangular Lattice

It is straightforward to derive an expression for the free energy per unit length of a step on a rectangular surface, $f_{rect}(\epsilon_x, \epsilon_y, \phi, T)$, starting from a model that describes the step free energy $f_{sq}(\epsilon_x, \epsilon_y, \phi, T)$ on a square surface, on the basis of the formation energies of individual step segments (e.g. lattice units) along the x-direction, ϵ_x , and along the y-direction, ϵ_y . Compare the square and rectangular geometries in fig. 4.1. The step on the rectangular surface, which makes an angle ϕ with the y-axis and has a length L , has the same total free energy F as the step on the square surface, with angle $\tilde{\phi}$ and length \tilde{L} . If the lattice spacings of the rectangular surface are pa and qa , the following relations hold:

$$\frac{\tilde{L}}{L} = \frac{\sin \phi}{p \sin \tilde{\phi}} \quad (4.1)$$

and

$$\tilde{\phi} = \arctan\left(\frac{q}{p} \tan(\phi)\right) \quad (4.2)$$

Therefore, the free energy on the rectangular surface becomes

$$f_{rect}(\epsilon_x, \epsilon_y, \phi, T) = \frac{F(\epsilon_x, \epsilon_y, \phi, T)}{L} = \frac{\tilde{L}}{L} f_{sq}(\epsilon_x, \epsilon_y, \tilde{\phi}, T) \quad (4.3)$$

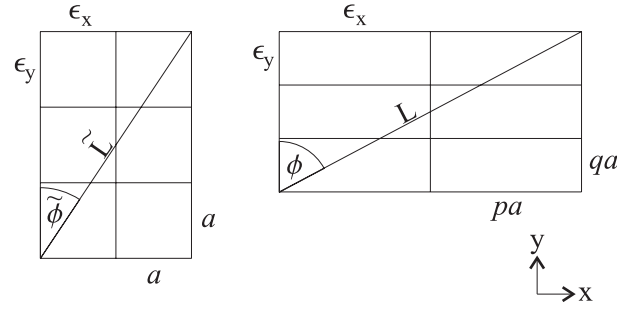


Figure 4.1: Steps on a square lattice, with lattice spacing a , and on a rectangular lattice, with lattice spacings pa and qa . The steps span the same numbers of step segments, in both the x -direction and the y -direction. If a step segment on the square lattice in the x -direction has the same energy ϵ_x as a step segment on the rectangular lattice in the x -direction, and the same holds for the y -direction, then the total step free energy F is equal for the two steps. The relations between the corresponding step lengths $L \leftrightarrow \tilde{L}$ and angles $\phi \leftrightarrow \tilde{\phi}$ are derived in the text.

$$= \frac{\sin(\phi)}{p \sin(\arctan(\frac{q}{p} \tan(\phi)))} f_{sq}(\epsilon_x, \epsilon_y, \arctan(\frac{q}{p} \tan(\phi)), T)$$

4.1.2 Energetics of a Missing-Row Surface

Figure 4.2a is a schematic representation of a piece of step on the Au(110)-surface. It is built up from three types of unit elements: (i) a single step segment along the

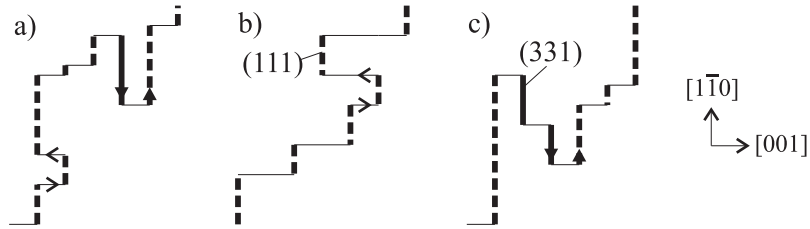


Figure 4.2: Schematic representation of step configurations on Au(110). a) A step configuration with fluctuations in both the $[001]$ - and the $[1\bar{1}0]$ -direction. Configurations with both types of fluctuations are considered in the two-dimensional Ising model (see section 4.1.4) b) A step configuration with fluctuations only in the $[001]$ -direction, as considered by the perpendicular fluctuation approximation of Carlon and van Beijeren [78] (see section 4.1.5). c) A step with fluctuations only in the $[1\bar{1}0]$ -direction, as considered in the alternative, parallel fluctuation approximation (see section 4.1.6).

$[001]$ -direction, with a length of the MRR period, i.e. two times the lattice constant

of Au of $a = 4.08 \text{ \AA}$, and a formation energy $E_{[001]}$; (ii) a single segment of a step along the $[1\bar{1}0]$ -direction of the (111)-type, with a length of the atomic spacing along this direction, of $a/\sqrt{2}$, and an energy $E_{[1\bar{1}0]}^{111}$; (iii) a single (331)-step segment, also with a length of $a/\sqrt{2}$, but with an energy $E_{[1\bar{1}0]}^{331}$.

The combination of a single (331)-step segment and a single (111)-step segment forms the lowest-energy excitation of a [001]-step. We will refer to such fluctuations as parallel fluctuations (bold arrows in fig. 4.2), because the extra step segments are parallel to the missing rows. Similarly, we define the combination of two [001]-step segments in opposite directions as a perpendicular fluctuation (thin arrows in fig. 4.2). In chapter 6 [90] we will see that the energies of (111)-and (331)-kinks are equal to within six permille, and that they are, to a very good approximation, equal to the energy of a [001]-step segment: $E_{[001]}$. With this information, we can express the formation energy of any step configuration as the sum of step segment formation energies of the three types, introduced above.

4.1.3 Separating Energy Contributions from Ground State and Fluctuations

We face a problem when trying to derive the free energy of a step on a missing row reconstructed surface f_{MRR} , starting from a model for the step free energy $f_{rect}(\epsilon_x, \epsilon_y, \phi, T)$ on an unreconstructed, rectangular surface. While on the unreconstructed surface there is just one type of step segment parallel to the MRs, on the reconstructed surface there exist two. The solution to this problem is not difficult, but has, to our knowledge, not been presented before.

Our method is to distinguish between two separate contributions to the free energy of a step on the simple rectangular lattice (see fig. 4.3), namely the ground state energy and the free energy due to fluctuations in the step position. Any configuration of a finite piece of step, which spans a distance L along direction ϕ , consists of at least $L|\sin \phi|/pa$ x-step segments and $L|\cos \phi|/qa$ y-step segments, where pa and qa are the lengths of step segments along x and y. Therefore, the ground state contribution to the step free energy per unit length is

$$e_{ground} = \frac{E_{ground}}{L} = \frac{\epsilon_x}{pa} |\sin \phi| + \frac{\epsilon_y}{qa} |\cos \phi| \quad (4.4)$$

If the ground state energy is subtracted from f_{rect} , the remaining part of the free energy is due to fluctuation.

$$f_{fluct} = f_{rect} - e_{ground} = f_{rect} - \frac{\epsilon_x}{pa} |\sin \phi| - \frac{\epsilon_y}{qa} |\cos \phi| \quad (4.5)$$

One part of the fluctuation free energy f_{fluct} accounts for the configurational entropy of the step segments of which the formation energy is already covered by e_{ground} . In addition, f_{fluct} contains the free energy related to the introduction of extra step

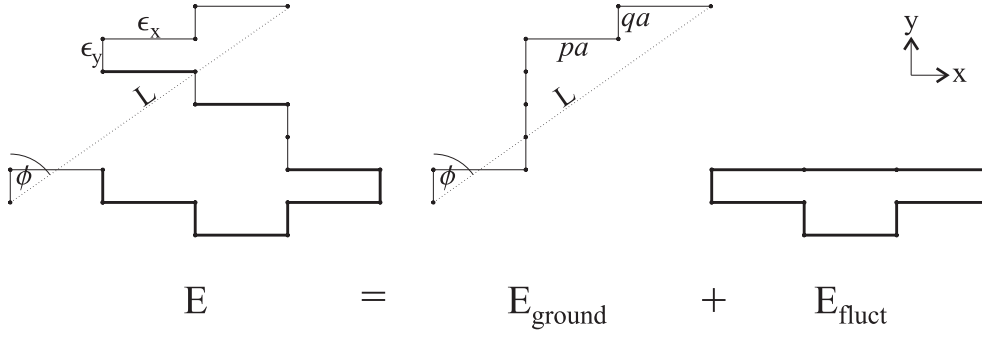


Figure 4.3: A step configuration with length L and angle ϕ on a rectangular lattice with lattice spacings pa in the x -direction and qa in the y -direction, and step segment energies ϵ_x and ϵ_y . The total energy E of the step configuration can be split into a ground state contribution E_{ground} and a fluctuation contribution E_{fluct} . The step segments that contribute to the ground state energy (thin lines) can be seen by looking from the left and from the top to the step configuration. The remaining step segments, that form the fluctuations, can be put into a closed loop, as there are as many step segments upwards as downwards, and as many to the left as to the right.

segments, i.e. of parallel and perpendicular fluctuations in the step configuration, as introduced in section 4.1.2. In these fluctuations, the step segments always come in pairs, i.e. $(111) + (331)$ or $2 \times [001]$. We can now rewrite eqs. 4.4 and 4.5 to describe the specific case of a missing-row reconstructed surface. We choose $\phi = 0$ for a (111) -step and consequently $\phi = \pi/2$ for a $[001]$ -step. Therefore, we associate ϵ_x with $E_{[001]}$ and ϵ_y with $E_{[1\bar{1}0]}^{111}$ in the ground state contribution (eq. 4.4). Since a fluctuation in the y -direction is a combination of one (111) - and one (331) -step, ϵ_y has to be replaced with $(E_{[1\bar{1}0]}^{111} + E_{[1\bar{1}0]}^{331})/2$ in the fluctuation term (eq.4.5), while ϵ_x still remains unchanged, $\epsilon_x = E_{[001]}$. With $p = 2$ and $q = 1/\sqrt{2}$, we find for the step free energy on a missing-row reconstructed surface:

$$\begin{aligned}
 & f_{MR}(E_{[1\bar{1}0]}^{111}, E_{[1\bar{1}0]}^{331}, E_{[001]}, \phi, T) \\
 &= e_{\text{ground}}(E_{[1\bar{1}0]}^{111}, E_{[001]}, \phi) + f_{\text{fluct}}(E_{[1\bar{1}0]}^{111}, E_{[1\bar{1}0]}^{331}, E_{[001]}, \phi, T) \\
 &= \left[\frac{E_{[001]}}{2a} |\sin \phi| + \frac{\sqrt{2} E_{[1\bar{1}0]}^{111}}{a} |\cos \phi| \right] \\
 &\quad + \left[f_{\text{rect}} \left((E_{[1\bar{1}0]}^{111} + E_{[1\bar{1}0]}^{331})/2, E_{[001]}, \phi, T \right) - \frac{E_{[001]}}{2a} |\sin \phi| \right. \\
 &\quad \quad \left. - \frac{E_{[1\bar{1}0]}^{111} + E_{[1\bar{1}0]}^{331}}{\sqrt{2}a} |\cos \phi| \right]
 \end{aligned}$$

$$= \frac{E_{[1\bar{1}0]}^{111} - E_{[1\bar{1}0]}^{331}}{\sqrt{2}a} |\cos \phi| + f_{rect}((E_{[1\bar{1}0]}^{111} + E_{[1\bar{1}0]}^{331})/2, E_{[001]}, \phi, T) \quad (4.6)$$

In the following three subsections (4.1.4, 4.1.6, 4.1.5) we will apply eq. 4.6 to three different choices for f_{rect} . The first model that we will treat is the two-dimensional anisotropic Ising model [76, 91], that considers both parallel and perpendicular fluctuations, and gives the exact step free energy for all temperatures and angles, as long as the energy can be calculated as a simple sum of step segment energies. The two-dimensional Ising model also takes into consideration step configurations with clusters of adatoms on the lower terrace and vacancy clusters inside the higher terrace. The second and third choices for f_{rect} are for two different applications of the anisotropic one-dimensional solid-on-solid model [75], that allows only fluctuations in a single direction. First we will study the case that only fluctuations perpendicular to the missing row direction are allowed, and then we will consider the one-dimensional solid-on-solid model with only fluctuations parallel to the MRs. In both one-dimensional solid-on solid models, configurations with adatom or vacancy clusters are forbidden. Results for the three models will be compared in section 4.2.

4.1.4 Two-Dimensional Ising Model

First, we calculate the step free energy on Au(110) using the two-dimensional anisotropic Ising model, in which both parallel and perpendicular fluctuations are allowed. Equation 3 of ref. [76] leads, in combination with eqs. 4.4 and eq. 4.6, to the step free energy

$$f_{Ising}(\phi) = \underbrace{\frac{1}{2\beta a} \alpha_1(\arctan(\frac{\tan \phi}{\sqrt{8}})) |\sin \phi| + \frac{\sqrt{2}}{\beta a} \alpha_2(\arctan(\frac{\tan \phi}{\sqrt{8}})) |\cos \phi|}_{f_{rect} \text{ in eq. 4.6}} + \frac{E_{[1\bar{1}0]}^{111} - E_{[1\bar{1}0]}^{331}}{\sqrt{2}a} |\cos \phi| \quad (4.7)$$

with

$$\alpha_1(\psi) = \text{arccosh} \left[\frac{(c^2 - n^2) \sin^2 \psi + m^2 \cos^2 \psi}{mc(\sin^2 \psi) + jm} \right] \quad (4.8)$$

$$\alpha_2(\psi) = \text{arccosh} \left[\frac{(c^2 - m^2) \cos^2 \psi + n^2 \sin^2 \psi}{nc(\cos^2 \psi) + jn} \right] \quad (4.9)$$

$$j = \sqrt{\left(\frac{c}{2} \sin 2\psi\right)^2 + \cos 2\psi(m^2 \cos^2 \psi - n^2 \sin^2 \psi)} \quad (4.10)$$

$$c = (1 + e^{-2\beta E_{[001]}})(1 + e^{-\beta(E_{[1\bar{1}0]}^{111} + E_{[1\bar{1}0]}^{331})}) \quad (4.11)$$

$$m = 2e^{-\beta E_{[001]}}(1 - e^{-\beta(E_{[1\bar{1}0]}^{111} + E_{[1\bar{1}0]}^{331})}) \quad (4.12)$$

$$n = 2e^{-\beta(E_{[1\bar{1}0]}^{111} + E_{[1\bar{1}0]}^{331})/2}(1 - e^{-2\beta E_{[001]}}) \quad (4.13)$$

and $\beta = 1/k_B T$. The factors $\sqrt{2}$ for the cosine, $1/2$ for the sine, and $1/\sqrt{8}$ for the tangent reflect the ratio between the lengths of step segments parallel and perpendicular to the missing rows.

4.1.5 Perpendicular Fluctuation Approximation

Next, we calculate the step free energy on Au(110) using a one-dimensional solid-on-solid model [75]. This model considers steps containing excursions in only one direction. Since we know that a (331)-step segment is higher in energy than a (111)-step segment, it seems logical to consider only step configurations consisting of (111)- and [001]-step segments, such as shown in fig. 4.2b. This approximation was used by Carlon and van Beijeren [78] for the calculation of the free energy of (111)-steps, probably because it avoided the difficulty introduced by the existence of two different step types along the $[1\bar{1}0]$ -direction. We will call this model the perpendicular fluctuation approximation, because the allowed fluctuations are all in the direction perpendicular to the missing rows. In this model, the expression for the free energy per unit length of an infinitely long (111)-step with an angle ϕ to the missing rows has been shown to be [75, 78]:

$$\begin{aligned} f_{\perp}(\phi) = & \underbrace{E_{[001]} \frac{|\sin \phi|}{2a} + E_{[1\bar{1}0]}^{111} \frac{\sqrt{2}|\cos \phi|}{a}}_{\epsilon_{ground}} + [\ln \bar{z}(\phi) - \beta E_{[001]}] \frac{|\sin \phi|}{2\beta a} \\ & + \left[\ln \left(\frac{2 \cosh(\beta E_{[001]}) - [\bar{z}(\phi) + 1/\bar{z}(\phi)]}{2 \sinh(\beta E_{[001]})} \right) \right] \frac{\sqrt{2}|\cos \phi|}{\beta a} \end{aligned} \quad (4.14)$$

where

$$\bar{z}(\phi) = \frac{\cosh(\beta E_{[1\bar{1}0]}^{111})\bar{t}(\phi) + \sqrt{1 + \sinh^2(\beta E_{[1\bar{1}0]}^{111})\bar{t}^2(\phi)}}{1 + \bar{t}(\phi)} \quad (4.15)$$

with

$$\bar{t}(\phi) = |\tan(\phi)|/2\sqrt{2} \quad (4.16)$$

The first two terms in eq. 4.14 represent the ground state energy of the step.

4.1.6 Parallel Fluctuation Approximation

By contrast with the assumption underlying the perpendicular fluctuation approximation, perpendicular fluctuations are never observed in STM images (at low and modest temperatures), and they are only expected to occur at high temperatures near the phase transition of the Au(110) surface. At lower temperatures, almost all fluctuations are parallel to the missing row (MR) direction [13, 67, 68], as illustrated in fig. 4.2c. The reason for this is that the formation energy of a [001]-step segment, perpendicular to the MRs, is high, $E_{[001]} = 200$ meV (see chapter 3 and [81]). The formation energy of a single perpendicular fluctuation is two times this amount, 400 meV. The formation energy of a parallel fluctuation is the sum of the formation energies $E_{[1\bar{1}0]}^{331}$ of a (331)-step segment and $E_{[1\bar{1}0]}^{111}$ of a (111)-step segment, which is as low as 19 meV [70]. Therefore, a model that considers only steps with parallel fluctuations should provide a much better approximation to the step free energy. We will call this the parallel fluctuation approximation.

The solid-on-solid model (e.g. equation 7 of ref. [76]), in combination with eqs. 4.4 and 4.6, immediately produces the step free energy per unit length in the parallel fluctuation approximation:

$$f_{\parallel}(\phi) = \frac{E_{[1\bar{1}0]}^{111} - E_{[1\bar{1}0]}^{331}}{\sqrt{2}a} |\cos \phi| + E_{[001]} \frac{|\sin \phi|}{2a} + \frac{\ln z(\phi) \sqrt{2} |\cos \phi|}{\beta a} + \ln \left(\frac{2 \cosh(\beta(E_{[1\bar{1}0]}^{331} + E_{[1\bar{1}0]}^{111}))/2) - [z(\phi) + 1/z(\phi)]}{2 \sinh(\beta(E_{[1\bar{1}0]}^{331} + E_{[1\bar{1}0]}^{111}))/2)} \right) \frac{|\sin \phi|}{2\beta a} \quad (4.17)$$

with

$$z(\phi) = \frac{\cosh(\beta E_{[001]}) t(\phi) + \sqrt{1 + \sinh^2(\beta E_{[001]}) t^2(\phi)}}{1 + t(\phi)} \quad (4.18)$$

and

$$t(\phi) = 2\sqrt{2} |\cot(\phi)| \quad (4.19)$$

This result can also be obtained from eq. 4.14 by an appropriate scale transformation and replacement of step segment energies for the ground state of the step and for the fluctuations. By separating the fluctuation term in eq. 4.14 we obtain

$$f_{\perp, fluct}(\phi) = \left[\ln \bar{z}(\phi) - \beta E_{[001]} \right] \frac{|\sin \phi|}{2\beta a} + \left[\ln \left(\frac{2 \cosh(\beta E_{[001]}) - [\bar{z}(\phi) + 1/\bar{z}(\phi)]}{2 \sinh(\beta E_{[001]})} \right) \right] \frac{\sqrt{2} |\cos \phi|}{\beta a} \quad (4.20)$$

Scaling and replacing the step segment energies leads to

$$f_{\parallel, fluct}(\phi) = -\frac{E_{[\bar{1}\bar{1}0]}^{111} + E_{[\bar{1}\bar{1}0]}^{331}}{\sqrt{2}a} |\cos \phi| + \frac{\ln z(\phi) \sqrt{2} |\cos \phi|}{\beta a} + \ln \left(\frac{2 \cosh(\beta(E_{[\bar{1}\bar{1}0]}^{331} + E_{[\bar{1}\bar{1}0]}^{111})/2) - [z(\phi) + 1/z(\phi)]}{2 \sinh(\beta(E_{[\bar{1}\bar{1}0]}^{331} + E_{[\bar{1}\bar{1}0]}^{111})/2)} \right) \frac{|\sin \phi|}{2\beta a} \quad (4.21)$$

Finally, by adding the ground state energy of

$$e_{ground}(E_{[\bar{1}\bar{1}0]}^{111}, E_{[001]}, \phi) = \frac{E_{[001]}}{2a} |\sin \phi| + \frac{\sqrt{2} E_{[\bar{1}\bar{1}0]}^{111}}{a} |\cos \phi| \quad (4.22)$$

we again obtain eq. 4.17.

4.2 Equilibrium Island Shape

The contour shape of vacancy and adatom islands on Au(110) with (111)-steps on both sides can be derived easily by applying the Wulff construction to the orientation dependent free energy of eqs. 4.7, 4.14 or 4.17. The result, fig. 4.4, has the peculiar, sharp-cornered, almond-like shape, which we observed in chapter 3 [81], and which was also predicted in [78] from the Wulff construction within the perpendicular fluctuation approximation (eq. 4.14).

In chapter 3, the energies of the different step segments $E_{[\bar{1}\bar{1}0]}^{331}$, $E_{[\bar{1}\bar{1}0]}^{111}$ and $E_{[001]}$ have been determined from fits of the Wulff construction, such as the one in fig. 4.4 to the observed shapes at a range of temperatures. In particular, the angle $2\Phi(E_{[\bar{1}\bar{1}0]}^{331}, E_{[\bar{1}\bar{1}0]}^{111}, E_{[001]}, T)$ of the sharp corner of the observed almonds (fig. 4.4) and the island aspect ratio $l/b(E_{[\bar{1}\bar{1}0]}^{331}, E_{[\bar{1}\bar{1}0]}^{111}, E_{[001]}, T)$, with l the length and b the width of the contour shape (fig. 4.4), were fitted. It was possible to obtain values for all three step segment energies, because the sum $E_{[\bar{1}\bar{1}0]}^{331} + E_{[\bar{1}\bar{1}0]}^{111} = 19 \pm 1$ meV had been measured independently in ref. [70]. The results for the step segment energies are $E_{[\bar{1}\bar{1}0]}^{111} = 3.7 \pm 0.5$ meV, $E_{[\bar{1}\bar{1}0]}^{331} = 15.3 \pm 1.1$ meV and $E_{[001]} = 200 \pm 60$ meV. These are the values used for all Wulff constructions in this chapter and in chapter 7.

Figure 4.5 compares f_{Ising} , f_{\parallel} , f_{\perp} and Monte Carlo simulation results (section 4.3) for the step free energy at $T = 600$ K. On the scale of the left panel, f_{Ising} (points) and f_{\parallel} (dotted line) coincide, while f_{\perp} (solid) is higher for almost all angles. As can be seen from the magnified insets, only for a small range of orientations around the $[\bar{1}\bar{1}0]$ step direction, f_{\perp} is lower than f_{\parallel} . The squares in the lower magnified inset represent free energy values obtained with the Ising model, whereas the circular points in the upper inset represent energy values obtained with Monte Carlo simulations (section 4.3).

Both solid-on-solid-approximations coincide with the exact Ising expression for the step free energy only at 0K, as there is no entropy in play. However, because

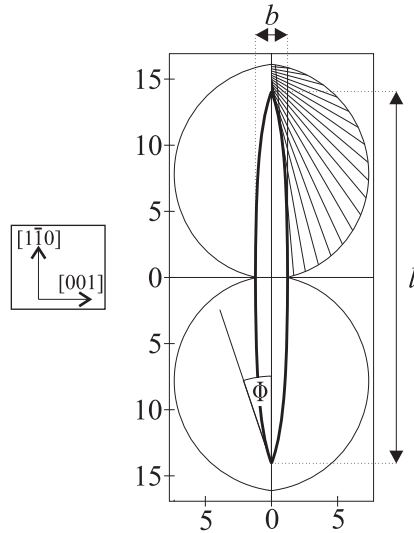


Figure 4.4: Wulff construction of the equilibrium shape of adatom and vacancy islands on Au(110) at $T = 400\text{K}$, calculated for the Ising model (eq. 4.7). The aspect ratio is defined as l/b and 2Φ is the sharp angle of the almond-shaped island. The energies are expressed in $\text{meV}/\text{\AA}$. The directions of the $[1\bar{1}0]$ and $[001]$ steps are indicated by the arrows.

both approximations do not consider *all* possible step configurations (fig. 4.2), they both overestimate all free energy values at all nonzero temperatures. This means, that for each (ϕ, T) combination, the *lowest* step free energy predicted by the two approximations is closest to the *true* step free energy of the Ising model.

The previous argument is not entirely correct, because there is, apart from the allowed directions of fluctuations, one additional difference between the Ising model and the solid-on-solid models: the Ising model includes the possibility of forming extra clusters of adatoms on the lower terrace, and clusters of vacancies inside the higher terrace, which is not permitted in the solid-on-solid models. When a step is introduced, the contribution to the free energy of these adatom and vacancy clusters is lowered. This increases the Ising step free energy slightly. The surprising consequence is, that the parallel fluctuation approximation is identical to the Ising result for the $[001]$ step orientation and the perpendicular approximation is exactly correct for both types of $[1\bar{1}0]$ steps. These identities hold for all temperatures [92]. However, for all other directions, the free energy of the Ising model is lower than the free energies of both solid-on-solid approximations.

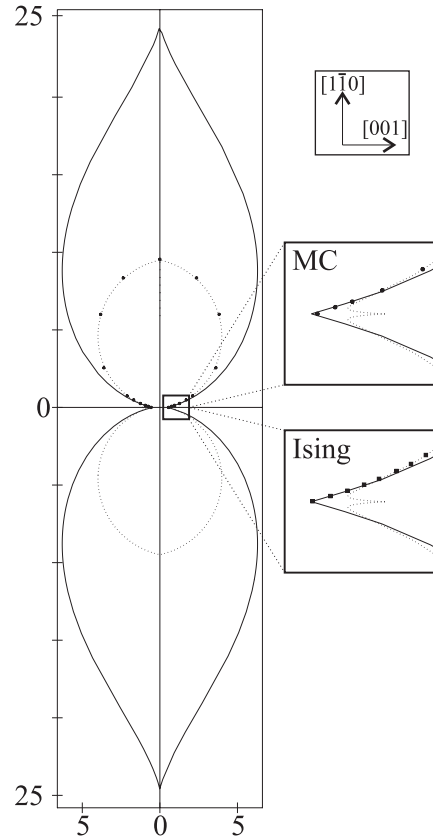


Figure 4.5: Comparison of f_{Ising} , f_{\perp} , f_{\parallel} , and MC simulations for almond-shaped islands on Au(110) at $T=600K$. The energies are expressed in $meV/\text{\AA}$. The directions of the $[1\bar{1}0]$ and $[001]$ steps are indicated by the arrows. On the scale of the left panel, f_{Ising} , f_{\parallel} (dotted line), and MC simulation (bigger dots) coincide, while f_{\perp} (solid) is higher for almost all angles. The range of angles for which f_{\perp} is lower than f_{\parallel} can be seen in the two magnified insets, in which the MC simulation energies are indicated with the circles in the upper inset, and the Ising energies with the squares in the lower inset. Of f_{\parallel} and f_{\perp} , the lower is always closest to the true free energy, f_{Ising} . The fact that most of the values obtained from the MC simulation are slightly higher is a consequence of the finite length of the steps in the simulation.

A step in the [001]- or $[1\bar{1}0]$ -direction can, to first approximation, only fluctuate in the direction perpendicular to the step. We have seen that f_{\parallel} , which was calculated by considering only parallel fluctuations, is a good approximation for the free energy of a [001]-step. The value of the free energy according to the perpendicular fluctuation approximation for a [001]-step is just the formation energy of a [001] step, which is clearly not a good approximation for high temperatures (see fig. 4.5), since the formation energy of a parallel fluctuation is relatively low. On the other hand, the perpendicular fluctuation approximation is exact for the $[1\bar{1}0]$ -direction. Similarly, for the $[1\bar{1}0]$ direction, the parallel fluctuation approximation always gives a value equal to the formation energy of a $[1\bar{1}0]$ -step.

When perpendicular fluctuations become important, the parallel fluctuation approximation fails. However, this is the case only at very high temperatures as a consequence of the high formation energy of perpendicular fluctuations. As can be seen from fig. 4.5, f_{\parallel} is indeed the better description of the step free energy for most step directions at all temperatures. Only for steps almost parallel to the $[1\bar{1}0]$ -direction, f_{\perp} yields a better approximation. As a consequence, the island shape predicted by the perpendicular approximation lies outside the one predicted by the parallel approximation, except for small portions on the $[1\bar{1}0]$ -sides of the shape that lie on the inside. This can be seen from the shapes at 600K, e.g. in the insets of in fig. 4.5. When the temperature is raised, these portions increase.

The figure also shows results of Monte Carlo (MC) calculations of the free energy (see 4.3). In the MC simulation, both parallel and perpendicular fluctuations were allowed. The difference between the model used for the MC calculations and the Ising model is, that the MC simulation did not allow for configurations with additional adatom clusters on the lower terrace or vacancy clusters in the higher terrace. Nevertheless, even for 600 K, the MC results coincide nicely with the free energy from the Ising model, which shows that, even at 600 K, such clusters have a negligible effect on the step free energies.

We have seen that there is only a small range around the $[1\bar{1}0]$ step direction, for which f_{\perp} provides the better approximation to f_{Ising} . It is exactly this range that determines the width b of the almond (see fig. 4.4) via the Wulff construction. It is less straightforward to see which portion of the free energy plot determines the length l of the almond. Via the Wulff construction, the end points of the almond shape correspond to the value of the free energy at the almond angle ϕ_0 (see fig. 4.4). For temperatures below 625 K, when ϕ_0 is at least a few degrees, $f_{\parallel}(\phi_0)$ is smaller than $f_{\perp}(\phi_0)$, and the length l , obtained from the Ising model, is described most accurately by f_{\parallel} . For very high temperatures (> 625 K) however, when the island width decreases drastically, the angle ϕ_0 also decreases and f_{\perp} , which is smaller than f_{\parallel} for small angles, describes the length of the islands most accurately. The temperature dependence of the almond shapes will be treated further in subsection 4.2.2.

4.2.1 Cusps in the Free Energy Plots

Under normal circumstances, a polar step free energy plot cannot contain cusps (discontinuity in slope) for $T > 0$ [93, 94, 95, 96]. However, in fig. 4.5 there are several cusps. For the $[1\bar{1}0]$ step direction, f_{\perp} shows the typical minimum (no cusp) for a step in a low-index-direction. By contrast, f_{\parallel} has a cusp-type maximum in this direction. The reason for this is, that in the parallel fluctuation model the $[1\bar{1}0]$ -step cannot make any fluctuations. Therefore $f_{\parallel}(\phi = 0)$ is not a function of temperature, and it is identical to the formation energy $\sqrt{2}E_{[1\bar{1}0]}^{111}/a$.

For the same reason f_{\perp} has a cusp-type maximum for the $[001]$ step direction, at a temperature independent value of $E_{[001]}/2a$. Also f_{\parallel} has a cusp-type maximum for the $[001]$ -step direction, but, unlike the previous cusps, this maximum is a function of temperature. At first sight this may seem impossible, because $[001]$ -steps *can* fluctuate in this model. The reason why there *is* a cusp-type maximum is that the almond shape is really formed by the combination of two half-island shapes, which intersect at the two crossing sites of the island with kinked, (111) -type steps. The cusp-like maxima for the $[001]$ -step direction of the polar step free energy plot are the points where the free energy curves for the two (111) -type steps intersect. We will discuss this peculiar situation in more detail in chapter 7. The exact free energy of the Ising model shows exactly the same shape as the parallel fluctuation model around this cusp.

4.2.2 Temperature Dependence of the Wulff Construction

The temperature dependence of the almond shape can be seen in fig. 4.6, together with the three models for the free energy. Thin lines are the free energy curves and thick lines the island contours. The dotted lines represent the parallel fluctuation approximation, and the solid lines correspond to the perpendicular fluctuation approximation. As in fig.4.5, the inner contour of the curves for the parallel and perpendicular fluctuation approximations coincides with the Ising model on this scale, both for the free energy curves and for the island shapes.

At zero temperature, the three models coincide, and the island shape is rectangular. Since the formation energy of perpendicular fluctuations is very high, the free energy of steps in the $[1\bar{1}0]$ -direction hardly changes when the temperature is raised. The parallel fluctuations however, set in at a much lower temperature, and therefore f_{Ising} and f_{\parallel} immediately begin to decrease for all nonzero ϕ ; As a consequence, the rectangle immediately changes into an almond and then becomes progressively shorter. As a result, the aspect ratio decreases somewhat. Above 500 K, the effect of $[001]$ -fluctuations becomes noticeable, and the width of the almonds decreases. The aspect ratio diverges when f_{Ising} (and f_{\perp}) becomes zero, for steps in the $[1\bar{1}0]$ -direction. This corresponds to a roughening transition of the reconstructed Au(110)-surface.

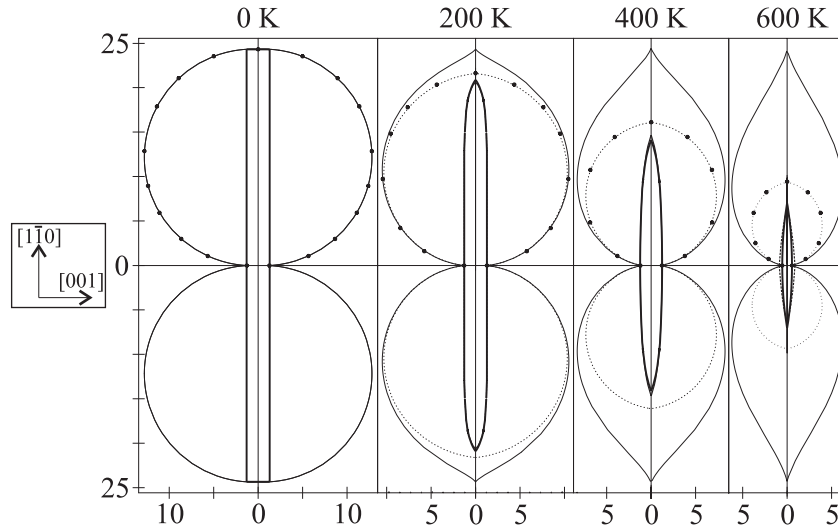


Figure 4.6: *Polar free energy plots for the Ising model and the parallel fluctuation approximation (thin dotted curve), the perpendicular fluctuation approximation (thin continuous curve), and from MC calculations (dots), of (111)-like steps on Au(110) for different temperatures, together with the equilibrium almond island shapes (thick curves). As the temperature rises, the aspect ratio initially decreases, then increases again, and finally diverges when $f(\phi = 0)$ decreases to zero. The energies are expressed in $\text{meV}/\text{\AA}$. The directions of the $[1\bar{1}0]$ and $[001]$ steps are indicated by the arrows.*

Figure 4.7 is a graph of the aspect ratio as a function of temperature, obtained from the Ising model. The vertical line is the asymptote at the roughening transition. Since the model does not consider the deconstruction transition (section 2.8.2 and chapter 5), these results cannot be trusted at temperatures close to and above the deconstruction temperature T_d , which is believed to lie between 650 K and 765 K [59, 63, 64, 82, 97]. For the same reason, the value of the roughening temperature of $T_R = 673\text{ K}$, obtained here from the Ising model, should only be considered as a coarse estimate of the true roughening temperature of Au(110), which is thought to be about 50 K above the deconstruction temperature [64].

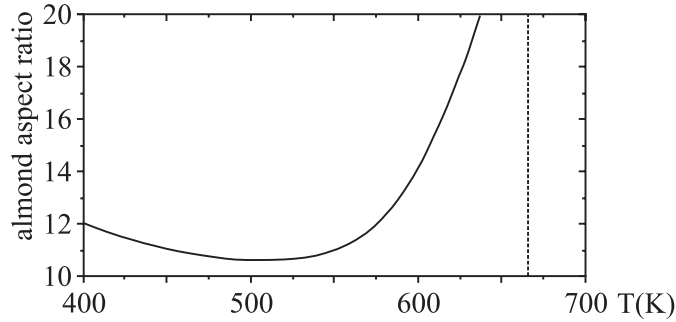


Figure 4.7: *Aspect ratio versus temperature for the almond shapes on Au(110). The aspect ratio first decreases, and then goes to infinity at the roughening transition.*

4.3 Summary

In summary, we have considered the theory of equilibrium shapes for (vacancy) islands on the (1x2) missing-row reconstructed Au(110) surface. We have calculated the step free energy exactly with the two-dimensional Ising model, where fluctuations of steps are allowed both parallel and perpendicular to the missing row direction, and we have considered two approximations to the step free energy, based on a one-dimensional solid-on-solid model. One model considers only step fluctuations parallel to the MRs, while the other allows only step fluctuations perpendicular to the MRs. Due to the low formation energy of parallel fluctuations, f_{\parallel} provides the best approximation to the step free energy for most step orientations. Only steps very close to the perfect MR orientation are better described by f_{\perp} .

The equilibrium shape of the almond-shaped islands is obtained by applying the Wulff construction to the orientation dependent step free energy. As a function of temperature, the aspect ratio of these islands first decreases, before it diverges at the roughening temperature.

Monte Carlo calculations of the step free energy were performed, in which both parallel and perpendicular fluctuations were allowed, like in the Ising model. At each temperature the MC results accurately reproduce the results of the Ising model, and follow the inner contour of the two energy curves, f_{\parallel} and f_{\perp} , obtained analytically for the parallel and perpendicular fluctuation approximations.

In chapter 7 we will return to these step free energy and equilibrium shape calculations. There, we will extend them to the special case of the metastable, asymmetric islands ('cigars'), observed in chapter 6.

Appendix: Monte Carlo Simulation

We have used a Monte Carlo (MC) simulation for calculating the step free energy as a function of temperature and orientation, allowing all steps to have excursions parallel and perpendicular to the MR-direction. An example of such a step is shown in fig. 4.2a. It consists of step segments in all four directions. In the simulations, such configurations were generated for long step sections, typically a few hundred lattice constants, for each orientation, according to the Metropolis algorithm [98]. To calculate the free energy of the step, it is enough to count the number of occurrences N_{E_i} of just one of the possible energy states E_i , for which the number of different configurations C_{E_i} is known. The total free energy F of the step is then

$$F = E_i + kT \ln(N_{E_i}) - kT \ln(C_{E_i}) - kT \ln(N_{tot}) \quad (4.23)$$

where N_{tot} is the total number of step configurations generated in the simulation. It is straightforward to calculate the total number of configurations with, e.g., r step segments to the right, zero step segments to the left, u step segments upward and d step segments downward. First choose p places ($1 \leq p \leq \min(d, r+1)$ if $d > 0$ and $u = 0$; $1 \leq p \leq \min(d, r)$ if $d > 0$ and $u > 0$; $p = 0$ if $d = 0$) before, between or after the r horizontal step segments where the step goes downward. These places can be chosen in $\binom{r+1}{p}$ ways. We have to distribute the d downward step segments over these p places, in such a way that on every place there is at least one downward step segment. There are $\binom{d-1}{p-1}$ possibilities to distribute them, except for the case $p = d = 0$. Finally, there are $r+1-p$ places left for the upward step segments, which gives $\binom{r-p+u}{u}$ possibilities, except for the case $r-p+1 = u = 0$. So the total number of the considered type of configurations is

$$C = \sum_{p=1}^{\min(d,r)} \binom{r+1}{p} \binom{d-1}{p-1} \binom{r-p+u}{u}, \quad \text{if } d > 0 \wedge u > 0 \quad (4.24)$$

C equals $\binom{r+u}{u}$ for $(d = 0 \wedge u > 0)$, $\binom{r+d}{d}$ for $(d > 0 \wedge u = 0)$, and 1 for $u = d = 0$. The simulation allows for both perpendicular and parallel fluctuations, but the step configurations which are counted all have a single fluctuation direction. It is now possible to predict which step formation energy will occur most frequently, and can best be counted during the simulation. The number of times that a configuration with energy E_i occurs during the simulation is proportional to

$$N_{E_i} \propto C_{E_i} e^{-E_i/kT}. \quad (4.25)$$

In this way it becomes possible to efficiently calculate the free energy of long step sections, of e.g. 600 lattice constants. This is important, because a step of finite length has a free energy per unit length, which is higher than that for an infinitely long step with the same overall orientation, which introduces a modest finite-size effect, as is visible in the lower inset of fig. 4.5.

Chapter 5

Domain Boundaries

Formation of domain boundaries at crossing and termination sites

In chapter 3 we have seen that networks of steps with crossing and termination sites provide the lowest energy means to connect the perfectly oriented parts of the Au(110)-surface at different heights. In this chapter we describe the observations of the spontaneous formation of domain boundaries in the missing-row reconstruction of Au(110). The domain boundaries nucleate at the two special sites on the surface: the termination and the crossing sites. We show that the length distribution of the domain boundaries is described already rather well by a simple theory, which accounts not only for the formation energy of the domain boundary, but also for the change in free energy of the steps in the vicinity of the boundary. However, the best fit is obtained by including also elastic step-step-interactions. The domain boundary formation on a perfect Au(110)-surface forms the onset of the deconstruction transition, in which the order of the missing-row reconstruction is destroyed.

5.1 Introduction

Since the exact solution of the order-disorder transition in the two-dimensional (2D) Ising model by Onsager [99], the number of experimental realisations of this transition has been very limited. The missing-row reconstructed (110) surfaces of Au and Pt (see e.g. figs. 2.6 a, b and 3.2a) have been proposed as candidates for such a transition, since their surface structure can occur in two different phases: either the odd or the even atom rows can be absent. At the temperature T_d , at which the free energy of domain boundaries between these phases vanishes (due to the entropy involved in their meandering) the MRR should undergo a 2D-Ising type order-disorder transition. This transition is called *deconstruction*. Campuzano et al. [59] were the first to observe the 2D-Ising character of this disordering on Au(110) with low-energy electron diffraction. On the other hand, surfaces with the MRR should also exhibit a roughening transition, in which they give up their long-range flatness. This transition, which is of the Kosterlitz-Thouless type [27], occurs at the temperature T_r for which the free energy of a step vanishes, due to the entropy involved in step meandering. Villain and Vilfan recognised the possible coupling of the two transitions [60], which they [61], Den Nijs [62], and Balents et al. [100] worked out theoretically. They showed that a surface with the MRR can undergo these transitions either separately - first deconstruction, and at higher temperature roughening - or as a single, combined transition, after which the surface is rough and deconstructed. The crucial parameter, determining whether or not the two transitions occur separately, is the ratio between the formation energies of a domain boundary and a step. X-ray diffraction measurements on Pt(110) show that this surface roughens and deconstructs at the same temperature [101]. For Au(110) the available experimental evidence suggests that roughening takes place at approximately 50 K [64] above the deconstruction temperature, for which the estimates range from 650 K to 765 K [59, 82, 64, 97, 63].

Here, we report STM measurements of the formation of thermally activated domain boundaries on Au(110) at temperatures well below the deconstruction transition. This formation is involved in the initial stage of the deconstruction. Although we have been successful in observing the roughening transition of Ag(115) [26, 102] with our home-built, high-speed STM setup [10], the high mobility of the Au(110) surface, even at temperatures well below T_d [9, 68, 70], has made direct STM observations of both the deconstruction and the roughening on this surface impossible. However, the low-temperature statistics of the domain boundaries allow us to derive the domain boundary formation energy. Combining this with the previously determined step formation energies [81, 103], we argue that Au(110) should indeed exhibit two separate phase transitions.

5.2 Observation

As discussed in chapter 3 and ref. [81], on misoriented parts of the Au(110) surface a network of crossing steps is formed. These networks ensure that all steps on the surface are of the close-packed, low-energy type (which we refer to as (111)-steps), while domain boundaries between different phases of the MRR are avoided completely.

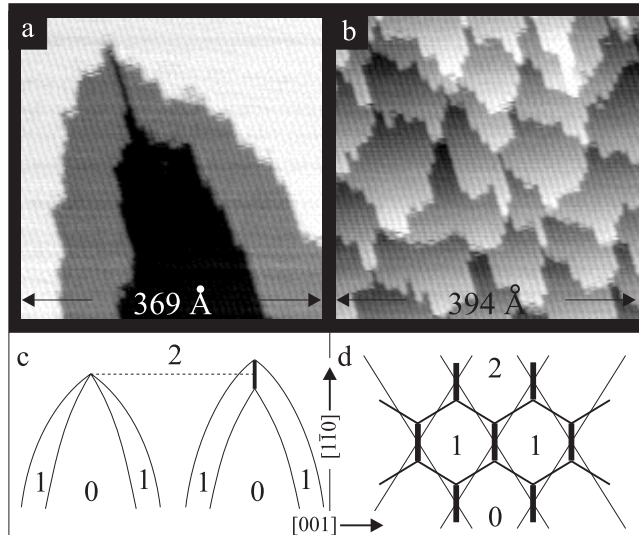


Figure 5.1: *Domain boundaries at the two special sites: (a) termination site and (b) crossing site. Sketches of the same sites (c) and (d), respectively; the thick lines indicate the domain boundaries and the numbers the terrace heights.*

Two special types of sites can be recognised in these networks, namely termination and crossing sites, see chapter 3 and ref. [81]. The termination sites are the locations where four steps meet and locally terminate (fig. 5.1a), while the crossing sites are the locations where two steps cross (fig. 5.1b). Sketches of these two sites are shown figs. 5.1 c and d, respectively; the numbers indicate the terrace heights. In both figures, the MRRs of the two neighbouring terraces at height 1 are out of phase with each other. By transforming from strict point contacts (see also fig. 3.3) into line segments, termination and crossing sites both provide natural birthplaces for domain boundaries. We have used STM to investigate the thermal generation of domain boundaries at these sites.

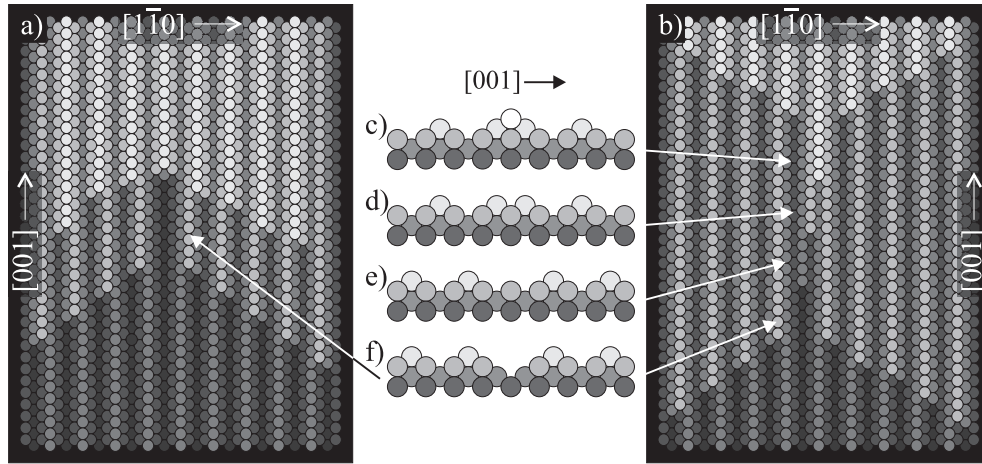


Figure 5.2: Schematic top view of the observed domain boundaries at a termination site (a) and a crossing site (b). The different structures are also shown in cross section view: (c) solid wall, (d) truncated solid wall, (e) truncated hollow wall, and (f) hollow wall.

Schematic top views of a termination site and a crossing site are shown in figs. 5.2 a, b. In total we observed four different types of domain boundaries, which are sketched in cross section in figs. 5.2 c-f. The *solid wall* (fig. 5.2c) and the *hollow wall* (fig. 5.2f) consist of small (111)-microfacets and can be expected to have low formation energies in analogy with the MRR surface itself. Truncating these structures by removing and adding an atom row, respectively, we obtain the other two configurations: the *truncated solid wall* (fig. 5.2d) and the *truncated hollow wall* (fig. 5.2e).

5.3 Domain Boundaries at Termination Sites

At the termination sites, we have exclusively observed hollow walls, at all temperaturesⁱ. The STM images in figs. 5.3 a and b show the length fluctuation of a hollow wall within 113 s at 343 K. The distribution of the lengths l of these walls was measured from 23, 28 and 38 STM images of a termination site at 343, 393, and 418 K, respectively. At each temperature, the shapes of the steps and the length of the domain boundary l fluctuated enough to represent the equilibrium statistics of the configuration.

In fig. 5.4 the distributions of the length l of the domain boundary, measured at 343 K (a), at 393 K (b) and at 418 K (c), are shown in semilogarithmic plots. When the formation energy of the 4-steps-and-domain-boundary configuration would increase with l according to $\Delta E = l \cdot E_{[1\bar{1}0]}^{hollow}$ ($E_{[1\bar{1}0]}^{hollow}$ is the hollow wall formation en-

ⁱWe will discuss this point later in section 5.5.

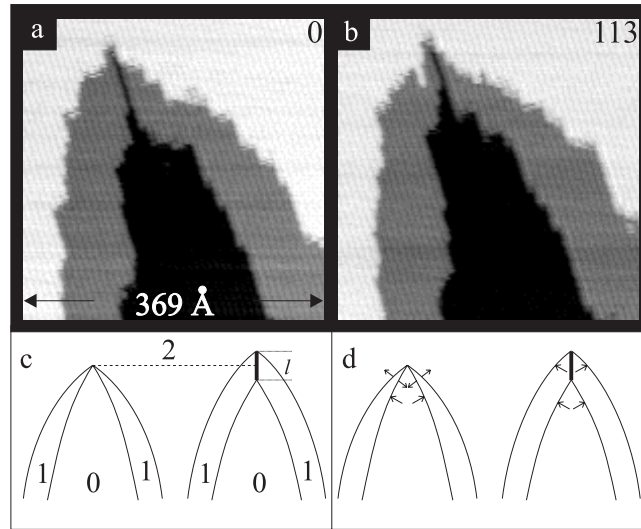


Figure 5.3: *Domain boundary (hollow wall) at a termination site: (a,b) STM images taken from a movie at $T = 343$ K. Notice the length change within a time of 113 s. (c,d) Schematic top views, illustrating the domain boundary formation (thick line). The numbers in (c) indicate the terrace heights and the arrows in (d) the step-step-interactions.*

ergy), the distribution should follow an exponential law $N \sim \exp(-l \cdot E_{[1\bar{1}0]}^{\text{hollow}} / k_B T)$, and the semilogarithmic plots of fig. 5.4 should be straight lines with a slope of $-\Delta E_{[1\bar{1}0]}^{\text{hollow}} / k_B T$. Instead, the distributions show a ‘maximum’ at each temperature,

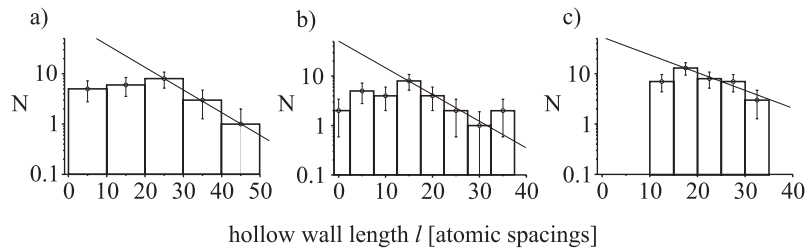


Figure 5.4: *Length distribution of the hollow wall at termination sites: (a) 343 K, (b) 393 K and (c) 418 K.*

at a length l between 15 and 25 atomic spacings (see fig. 5.4). This behavior cannot be explained on the basis of changes in length of the four steps; in order to make room for a domain boundary of length l , the outer steps become $l/2$ longer, while the inner ones become $l/2$ shorter, so that the total step length remains unchanged (see fig. 5.3c). Since the length changes $l/2$ are modest with respect to the total length of the steps, we can safely neglect the effect of changes in step entropy.

Elastic interactions between the four steps can result in a deviation from a straight line for small l (fig. 5.4). When two steps run strictly parallel, the interaction energy is proportional to $1/d^2$ [31] (see also section 2.5), if d represents the distance between the steps. The interaction between parallel steps that are both up or both down is repulsive, whereas up-down combinations can be either repulsive or attractive. As we will see later, almost all step combinations on Au(110) are repulsive (fig. 5.3d). This repulsion results in an energy penalty for configurations with small l . When l is large enough, the interactions within the left step pair and within the right pair have reduced to insignificant values. Furthermore, the effect of the interactions within the inner step pair and within the outer one cancel: one tends to increase and the other tends to decrease the domain boundary length by exactly the same amount. As a result, the step repulsion energy should vary insignificantly for larger l -values. Therefore, we expect the semi-logarithmic plots of fig. 5.4 to show straight-line behavior for large l . The values at small l should fall below the straight line, which is consistent with the experiment. Thus, we disregard the short domain boundaries in fig. 5.4, and obtain an estimate for the hollow-wall energy from a straight-line fit to the distributions for l -values above the maximum in the distribution. This yields energies of $E_{[1\bar{1}0]}^{hollow} = 3.1$ meV at 343 K, $E_{[1\bar{1}0]}^{hollow} = 4.2$ meV at 393 K and $E_{[1\bar{1}0]}^{hollow} = 2.9$ meV at 418 K, which we combine into $E_{[1\bar{1}0]}^{hollow} = 3.4 \pm 1.3$ meV. All energies are expressed per atomic spacing along the $[1\bar{1}0]$ -direction of 2.88 Å.

5.4 Domain Boundaries at Crossing Sites

We now turn to the domain boundaries formed at the crossing sites in the step networks (fig. 5.5). By contrast with the termination sites, we have observed all four boundary types at the crossing sites as introduced in fig. 5.2. When present, they always appear in a strict order, which is, from the lower to the higher terrace: hollow wall, truncated hollow wall, truncated solid wall and solid wall. Here, we concentrate on the most prominent sub-ensemble of domain boundary configurations, consisting of combinations of only a hollow wall and a solid wallⁱⁱ.

5.4.1 Simple Boltzmann Distribution

Figure 5.6 shows the distributions of the hollow wall length (a), the solid wall length (b) and the combined length (c) of the sub-ensemble of domain boundaries, introduced above. The data in fig. 5.6 were obtained from 587 observations of ~ 60 crossing sites at a temperature of 326 K. At low temperatures, in the totally *closed* network structure, i.e. the crossing points are still point contacts, short hollow and solid walls can always be recognised already. However, these should really be re-

ⁱⁱThe other two walls are only present in $\sim 10\%$ of all observations.

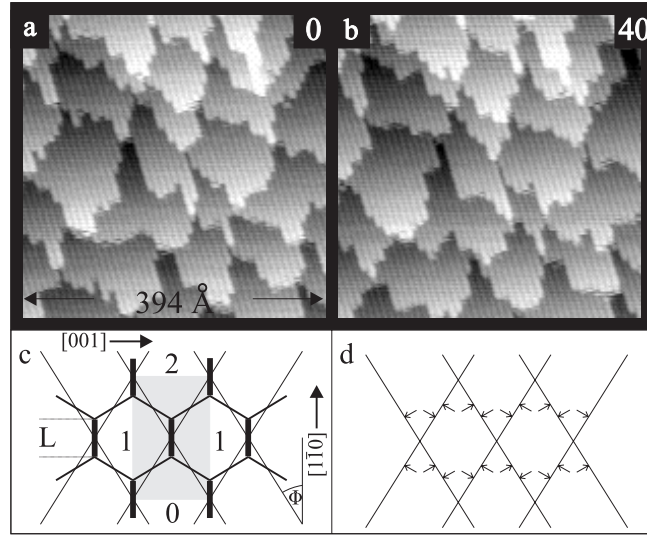


Figure 5.5: Domain boundaries, solid and hollow walls, at crossing sites: (a,b) STM images taken from a movie at $T = 326$ K. Notice the length fluctuations of the domain boundaries, taking place within a time of 40s. (c,d) Schematic top views, illustrating the domain boundary formation (thick lines). The numbers in (c) indicate the terrace heights and the arrows in (d) the elastic step-step-interactions.

garded as those parts of the ‘straight’, crossing steps, where the steps are at a short distance of only one MR period from each other. Therefore, the lengths in fig. 5.6 have all been corrected for this ‘finite size’ discretisation effect.

Again, the plots deviate from straight lines, showing that also these distributions are not simply exponential. In a first attempt to fit these data, we assume the hollow and solid walls to form completely independently from each other. If l_1 represents the length (expressed in atomic spacings) of the hollow wall and l_2 the length of the solid wall, the partition sum for this simplified system is given by ($\beta = 1/k_B T$):

$$Z = \sum'_{l_1} \sum'_{l_2} e^{-\beta[l_1 \cdot E_{[1\bar{1}0]}^{hollow} + l_2 \cdot E_{[1\bar{1}0]}^{solid}]} \quad (5.1)$$

The primes indicate the restriction on the lengths l_1 and l_2 , that their sum, L , should not exceed half the length of the unit cell, which is indicated by the gray rectangle in fig. 5.5c. At this length, the steps in the network are perfectly aligned along the $[001]$ -direction. Notice, that L depends on the distance, d , between the steps in the original, *closed* network, and therefore on the misorientation of the surface with respect to the (110) plane. Using $E_{[1\bar{1}0]}^{hollow}$ and $E_{[1\bar{1}0]}^{solid}$ as free parameters, and simultaneously fitting the three distributions in fig. 5.6, we obtain the dashed curves for $E_{[1\bar{1}0]}^{hollow} = 3.4 \pm 1.6$ meV and $E_{[1\bar{1}0]}^{solid} = 4.0 \pm 2.0$ meV. The normalised goodness of this combined fit

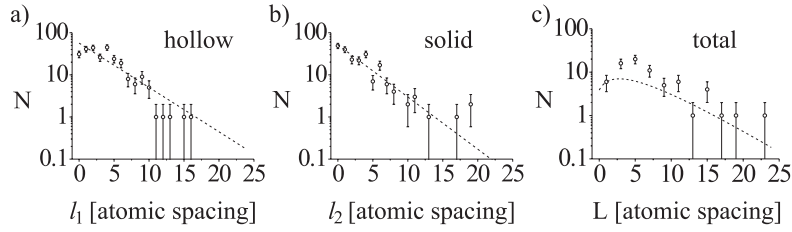


Figure 5.6: Semilogarithmic plots of the domain boundary length distributions measured at crossing sites at $T = 326$ K. The lengths of the hollow wall l_1 (a), the solid wall l_2 (b), and the combined domain boundary (hollow + solid) L (c) are expressed in atomic spacings (2.88 \AA). The three curves have been calculated according to the model of eq. 5.1 for independent hollow and solid wall distributions. Shown is the result of a simultaneous least-squares fit to all three distributions.

amounts to $\chi^2 = 2.58$.

5.4.2 Including the Free Energy Change of the Step Network

By treating the distributions of l_1 and l_2 as independent, eq. 5.1 has neglected the (free) energy contribution stemming from the modifications of the steps in the network, which are necessary to make room for the domain boundaries.ⁱⁱⁱ Before a domain boundary is introduced, the gray unit cell in fig. 5.5c contains four step segments (two crossing steps). When a domain boundary forms at the crossing site, these four step segments are shortened and their orientation angle Φ (see fig. 5.5c) increases. The step shortening lowers the total free energy, while the increase in Φ leads to an increase in the step free energy per unit length^{iv}. We use eq. 4.17 [103] to calculate the orientation-dependent step free energy.

The resulting change of the total free energy of the step network $\Delta F_{step}((l_1 + l_2), \Phi, d)$ ^v, leads to a correction factor on the partition sum, given by $e^{-\beta \Delta F_{step}}$:

$$Z = \sum_{l_1} \sum_{l_2} e^{-\beta [l_1 \cdot E_{[1\bar{1}0]}^{hollow} + l_2 \cdot E_{[1\bar{1}0]}^{solid}]} \cdot e^{-\beta [\Delta F_{step}]} \quad (5.2)$$

This correction factor introduces a coupling between the statistical ensembles of l_1 and l_2 . The dotted curves in figs. 5.7 represent the second fit to the length distributions of domain boundaries at the crossing sites, where we have included the correction factor for the modification of the step network. The best-fit energies are $E_{[1\bar{1}0]}^{hollow} = -0.2$

ⁱⁱⁱAn alternative way of making room for the domain boundaries is to rise the step density. Measurements by Hoogeman et al. [10], who observed the same region in a step network on Au(110) while changing the temperature from 294 K to 565 K, show no change in the density of steps.

^{iv}This is not entirely true for low temperatures and Φ close to $\pi/2$.

^vHere, d is the average distance between the steps in the network, prior to boundary formation. Note, that there are 2 domain boundaries per unit cell of the network.

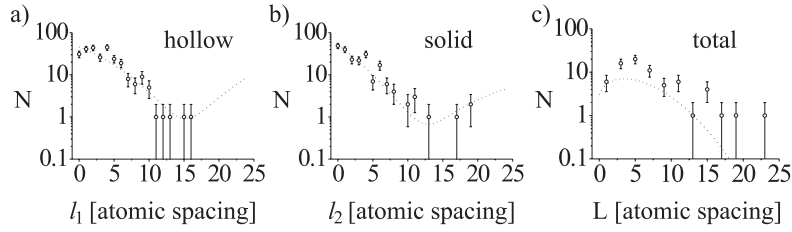


Figure 5.7: Same as fig. 5.6, but with simultaneous fits according to eq. 5.2, which also accounts for the change in free energy of the steps in the network, forced by the introduction of the domain boundary.

± 1.6 meV and $E_{[1\bar{1}0]}^{solid} = 1.4 \pm 2.0$ meV, and the combined goodness of fit is lowered significantly to $\chi^2 = 2.04$. The lowering of the two best-fit values for the domain boundary energies reflects the fact that the step network is at a minimum free energy before domain boundary formation. If the increase in step network free energy, necessarily accompanying domain boundary formation, is not taken into account, the domain boundary energies should indeed come out too high.

5.4.3 Including also Elastic Step-Step-Interactions

An even better fit can be obtained when also the changes in step interactions in the network structure are taken into account. For a full description of the energy change of the network structure, caused by the introduction of domain boundaries, we need to evaluate the elastic step-step-interaction energy^{vi} of two crossing steps. This energy has been derived by Vilfan [104] on the basis of continuum elasticity theory [30, 31, 34]. Figure 5.8 shows two steps crossing under an angle Θ . The total elastic step-step-interaction energy $E_{12}(\Theta)$ is calculated as a line integral along step 1 from $-\infty$ to ∞ . The integrand is proportional to $1/d^2$, where d now represents the shortest distance between step 1 and step 2 for each location on step 1. Since the continuum theory breaks down, if d becomes so small that it approaches atomic dimensions, Vilfan [104] has defined a circle with radius a at the crossing point of the steps and lumped the complete short-range interaction energy of this area into an orientation-independent vertex energy W . As a result he has obtained [104, 105].

$$E_{12}(\Theta) = \frac{4(1 - \sigma^2)}{\pi Y a} \frac{(\mathbf{f}_{\parallel}^2 \cos^2(\Theta) - \mathbf{f}_z^2 \cos(\Theta))}{\sin^2(\Theta)} + W \quad (5.3)$$

where \mathbf{f}_{\parallel} describes the local stretch term, \mathbf{f}_z the local torque term, Y the Young's modulus and σ the Poisson's ratio (see also equation 2.2). The natural choice for the vertex radius is the atomic spacing, $a = 2.88$ Å. Equation 5.3 reflects the same

^{vi}See also section 2.5.

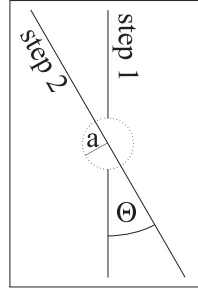


Figure 5.8: Two steps cross at an angle of Θ . The elastic step-step-interaction energy is calculated via simple integration of the familiar $1/d^2$ interaction. The contribution resulting from the area indicated by the circle (radius a), which is centered at the crossing point, is treated as a separate vertex energy W , to avoid the divergence of the continuum theory for small distances.

general behaviour as equation 2.2 for parallel steps. For steps of the same type the orientation-dependent term becomes proportional to

$$\mathbf{f}_{\parallel}^2 + \mathbf{f}_z^2 \quad \Theta \rightarrow \pi \quad (5.4)$$

and for steps of opposite type it becomes proportional to

$$\mathbf{f}_{\parallel}^2 - \mathbf{f}_z^2 \quad \Theta \rightarrow 0 \quad (5.5)$$

Note that, apart from the vertex energy, the ratio of \mathbf{f}_{\parallel} and \mathbf{f}_z determines at which angles $\Theta \leq \pi/2$ the interaction is attractive or repulsive. The interaction vanishes for $\Theta = \pi/2$, and is always repulsive for $\Theta > \pi/2$.

Imagine the initial (closed) network structure without any domain boundaries, as sketched in fig. 5.9a. Per unit cell ^{vii} of the network, two steps of finite length cross under an angle Θ . Since the elastic step-step-interaction energy reduces quickly when the distance between the steps is increased, we introduce only a modest error by calculating the energy for these finite-length steps with equation 5.3, which was deduced for infinity long steps.

Initially, before the network contains domain boundaries, we observe angles $\Theta_{start} < \pi/2$. The maximum angle is $\Theta = \pi$. At this angle, the network steps are perfectly straight and aligned along the [001]-direction. While the total domain boundary length increases from zero to its maximum length, Θ passes the special angle of $\pi/2$ at which the elastic step-step-interaction energy cancels. The ratio, $r = \frac{|\mathbf{f}_{\parallel}|}{|\mathbf{f}_z|}$, of the absolute values of the stretch and the torque terms determines at which angles the interaction energy (angle-dependent term in equation 5.3) switches

^{vii}The unit cell is indicated by the gray area.

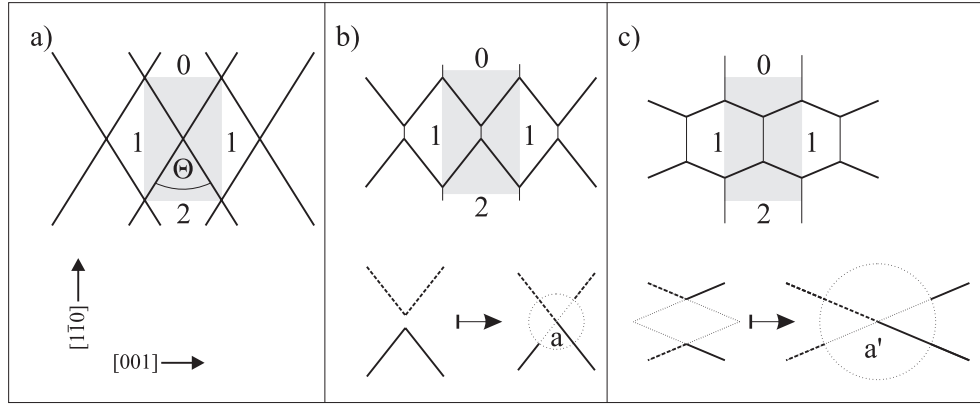


Figure 5.9: Step configurations of (a) the initial network; (b) the network with short domain boundaries; and (c) the network with long domain boundaries. The gray area represents the (constant) unit cell of the network. Terrace heights are indicated by numbers. The lower diagrams in (b) and (c) illustrate our approximation of the remaining elastic step-step-interactions.

sign:

$$r > 1 : \text{sign}(E_{12}(\Theta)) = \begin{cases} + & : & 0 < \Theta < \arccos \frac{1}{r^2} \\ - & : & \arccos \frac{1}{r^2} < \Theta < \pi/2 \\ + & : & \pi/2 < \Theta \end{cases}$$

$$r < 1 : \text{sign}(E_{12}(\Theta)) = \begin{cases} - & : & 0 < \Theta < \pi/2 \\ + & : & \pi/2 < \Theta \end{cases}$$

Since the step-step-interaction energy of the steps in the network with domain boundaries differs significantly for angles $\Theta > \pi/2$ and angles $\Theta < \pi/2$, we also divide our description into two parts.

For all $\Theta < \pi/2$ we approximate the interaction energy by the value for one crossing step pair without a domain boundary (lower image in fig. 5.9b). This overestimates the interaction strength, because the domain boundary increases the distance only between the parts of step 1 and 2 that run under the larger angle ($\pi - \Theta$) with respect to each other, i.e. between the left segments and between the right segments. However, we estimate the error to be small, since the domain boundary lengths are small and the interaction energy is strongly dominated by the step parts that run under the smaller angle Θ , i.e. the dotted step parts and the solid step parts in the lower diagram in fig. 5.9b.

If $\Theta > \pi/2$, the simple description of two crossing steps fails. This is because now the step parts that approach each other under the smaller angle (dotted step parts and solid step parts in the lower diagram of fig. 5.9c) are separated from one another

by the domain boundary length L . We approximate the interaction energy by that of two crossing steps, in combination with an increased effective vertex radius a' around the crossing point. Now the natural choice for the radius a' becomes a function of the total domain boundary length L :

$$a'(\Theta) = \frac{L}{2} \frac{1}{\cos(\Theta/2)} \quad (5.6)$$

We combine the optimal choices for the vertex radius for angles above and below $\pi/2$ in the following analytical form

$$a(\Theta) = -\frac{\left(1 + \frac{(\pi/2 - \Theta)}{|\pi/2 - \Theta|}\right)}{2} \cdot \left(\frac{L}{2 \cos(\Theta/2)} - 2.88 \text{\AA}\right) + \frac{L}{2 \cos(\Theta/2)} \quad (5.7)$$

The combination of equations 5.3 and 5.7 provides us with a single expression for the elastic step-step-interaction energy $E_{int}(\Theta)$ for *all angles*. Note, that we neglect (the variations in) both the vertex energies and the elastic *step-boundary interaction* energies.

We include the elastic step-step-interaction by multiplying each term of the partition sum with a second correction factor, $e^{-\beta \Delta E_{int}}$:

$$Z = \sum_{l_1}' \sum_{l_2}' e^{-\beta[l_1 \cdot E_{[1\bar{1}0]}^{hollow} + l_2 \cdot E_{[1\bar{1}0]}^{solid}]} \cdot e^{-\beta[\Delta F_{step} + \Delta E_{int}]} \quad (5.8)$$

Since the network angle Φ (see fig. 5.5c) and Θ are simply related by $\Theta = 2\Phi$, the step interaction energy E_{int} is a function of $(l_1 + l_2)$, Φ and d . This means that the step interaction in the network can either be attractive or repulsive for $0 < \Phi < \pi/2$ (see arrows in fig. 5.3d), and it is always repulsive for $\Phi > \pi/2$ (see, e.g., the configuration with domain walls in fig. 5.9c).

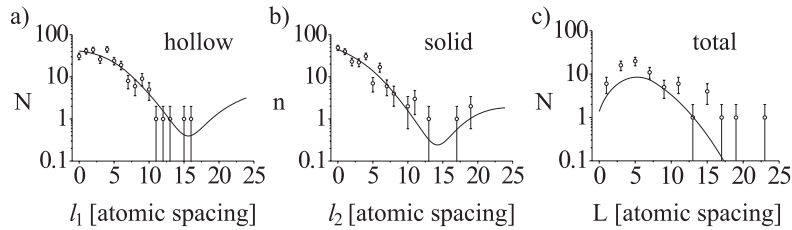


Figure 5.10: Same as fig. 5.7, but with simultaneous fits according to eq. 5.7, which also accounts for the changes in elastic interactions between the steps in the network.

When we include also the step interactions in our fit^{viii}, treating the ratio $f_{||}/f_z$ and f_z as additional fitting parameters, we obtain the solid curves in figs. 5.10 a-c,

^{viii}We use a Poisson's ratio and Young's modulus of $\sigma = 0.42$ and $Y = 0.499 \text{ eV/\AA}^3$, respectively [104].

for $E_{[1\bar{1}0]}^{hollow} = 0.4 \pm 1.6$ meV, $E_{[1\bar{1}0]}^{solid} = 1.5 \pm 2.0$ meV, $f_{||}/f_z = 3.4 \pm 0.4$, and $f_z = 0.31 \pm 0.04$ eV/Å. Inclusion of the step interactions has substantially improved the combined goodness of fit to $\chi^2 = 1.78$. Since our best-fit ratio $f_{||}/f_z$ is larger than unity, network steps on Au(110) repel for almost all angles^{ix}, as has been observed also for steps on Pt(110) [87]. This works in favour of the formation of domain boundaries, which explains why the domain boundary energies have to be increased again in order to obtain a good fit.

5.4.4 Overview of the Three Models

model	$E_{[1\bar{1}0]}^{hollow}$	$E_{[1\bar{1}0]}^{solid}$	χ^2
1	3.4 ± 1.6 meV	4.0 ± 2.0 meV	2.58
2	-0.2 ± 1.6 meV	1.4 ± 2.0 meV	2.04
3	0.4 ± 1.6 meV	1.5 ± 2.0 meV	1.78

Table 5.1: Domain boundary energies per atomic spacing (2.88 Å) for hollow and solid walls, obtained from simultaneous fits to the measured distributions in fig. 5.11 for the three models discussed: (1) independent distributions of hollow and solid walls (eq. 5.1), (2) including the change in free energy of step network (eq. 5.2), and (3) also including step-step interactions (eq. 5.7). The values of the goodness of fit (normalised χ^2) show that the third model produces a significantly better fit than the first and the second.

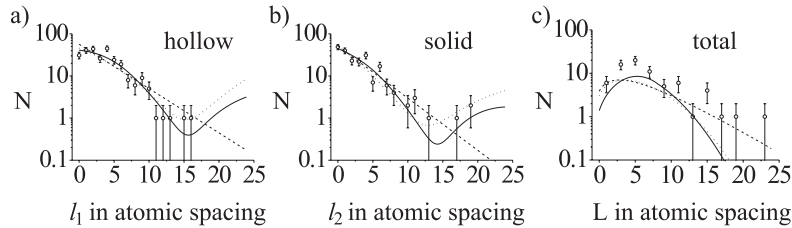


Figure 5.11: Semilogarithmic plots of the measured domain boundary length distributions measured at crossing sites at $T = 326$ K. The lengths of the hollow wall l_1 (a), the solid wall l_2 (b) and the combined domain boundary (hollow + solid) L (c) are expressed in atomic spacings (2.88 Å). The curves are the simultaneous least-square fits to the three distributions for: (dashed) independent distributions of hollow and solid walls, (dotted) including the change in free energy of step network and (solid) also including the step-step-interactions. The best-fit wall energies for each fit are shown in table 5.1.

^{ix}The range of attraction is approximately $85^\circ < \Theta < 90^\circ$.

Table 5.1 gives an overview of the different hollow- and solid-wall formation energies, which are obtained from the fits by the three models, described in the previous sections. The first model assumes independent distributions of the solid and the hollow walls. The second model includes also the changes in free energy of the step network. This results in a coupling of the two distributions. In addition, the third model takes into account also the elastic step-step-interactions. Notice the significant reduction of the normalised χ^2 values, which describe the goodness of the fits. To compare the different models, fig. 5.11 shows all three fits together.

5.5 Why only Hollow Walls at Termination Sites?

Since we saw that all types of domain boundaries (most prominently the hollow and the solid wall) are formed at the crossing sites, the question presents itself why we observed only hollow walls at the termination sites. The answer is found in the structure: the two sites differ substantially in the MRR-phases of their terraces. Figure 5.12a

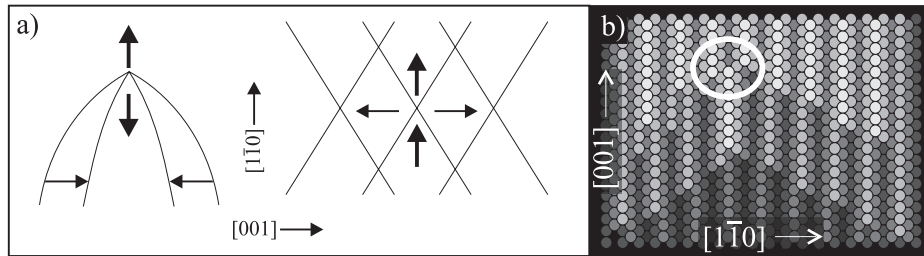


Figure 5.12: (a) Sketch of the MRR phases (denoted by the arrows) at a termination site and a crossing site. Note that the uppermost and the lowermost terrace are out of phase at a termination site and in phase at a crossing site. (b) Schematic top view of a termination site with a solid wall domain boundary. This wall is out of phase with the MRR of the topmost terrace (circle), which introduces a substantial energy penalty (see text).

shows a sketch of a termination and a crossing site. The arrows denote the phases of each level, as explained in section 3.1.2. Note, the uppermost and the lowermost terrace are out of phase with each other at the termination site, whereas they are in phase at the the crossing site. Figure 5.12b shows a ball model of a hypothetical solid wall at a termination site. Since the uppermost and the lowermost terraces are out of phase, the solid wall is also out of phase with the MRR of the uppermost terrace, see circle. This implies that the formation of a solid wall would introduce a little domain boundary along the [001]-direction. Since we expect the energy of this boundary, $E_{[001]}^{DB}$, to be comparable with the energy of a [001]-step segment (200 meV/MRR period), it is obvious that the thermal energy is too low to excite this structure at the temperatures of our observations.

5.6 Result and Consequences

We now have two independent values for the hollow wall energy: 3.4 ± 1.3 meV from the termination sites and 0.4 ± 1.6 meV from the crossing sites. We combine these two values into our final estimate for the hollow wall energy of $E_{[1\bar{1}0]}^{hollow} = 1.9 \pm 1.0$ meV.

Finally, we compare the wall energies, determined here, with the step energies on Au(110), $E_{[1\bar{1}0]}^{111} = 3.7 \pm 0.5$ meV and $E_{[001]} = 200 \pm 60$ meV, determined experimentally in chapter 3 (refs. [81, 90, 103]), in order to characterise the order-disorder transition behavior at elevated temperatures. In the theory of Den Nijs [62], the parameter governing the coupling of the two phase transitions, deconstruction and roughening, is the ratio R between the formation energies of a domain boundary and a step. If $R > 2$, the surface undergoes the two transitions simultaneously. If $R < 2$, there is a temperature window, in which the surface is deconstructed but not rough: the so-called disordered flat phase. For $1 < R < 2$, this temperature window is very narrow. From our measurements, we estimate $R = 0.5 \pm 0.3$, which is definitely lower than 2. This result is in agreement with the evidence that Au(110) exhibits two separate phase transitions [64]. However, substituting our energy values in the theory by Den Nijs [62], we obtain predictions for the two phase transition temperatures of $T_d = 51$ K and $T_r = 102$ K, which are off by approximately one order of magnitude from the experimental values. This was to be expected, since the model by Den Nijs describes only the generic aspects of the coupled phase transitions, and leaves out several of the structural details of the Au(110)-surface.

More accurate predictions for the phase transition temperatures are obtained by combining our energy values with the theory of Villain and Vilfan (VV) [61]. Although the treatment of the coupling between the two phase transitions is much more approximative in the VV theory, this theory does include all the important structures (e.g. various types of walls). Monte Carlo simulations for the same system [66] show that the approximations in the VV theory have relatively modest effects on the precise transition temperatures. Since the value of R is significantly lower than unity, the two transitions couple only very weakly, so that the VV theory may indeed be expected to provide a good approximation for the specific case of Au(110).

VV take into account domain boundaries and (111)-steps with their fluctuations, see fig. 5.13. Each fluctuation in a step or domain boundary position involves at least one interrupted atom row (circles in fig. 5.13) with an energy W_0 . In the VV theory, the transition temperatures critically depend both on the energy ratio of a hollow wall $E_{[1\bar{1}0]}^{hollow}$ and a row interruption W_0 and on the energy ratio of a (111)-step $E_{[1\bar{1}0]}^{111}$ and W_0 . In addition, VV assume that the hollow wall energy equals the solid wall energy. Since a step segment along the [001]-direction has two interrupted atom rows (fig. 3.4), we assume that W_0 equals $\frac{1}{2} \cdot E_{[001]} = 100$ meV. Figure 5.14(a) shows two phase diagrams, calculated by VV for the case of $E_{[1\bar{1}0]}^{hollow}/W_0 = E_{[1\bar{1}0]}^{solid}/W_0 = 0.01$,

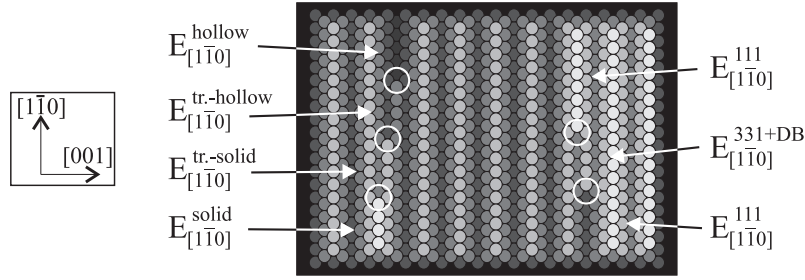


Figure 5.13: *Schematic top view of the structures and energies regarded in the theory of VV [61]. All four possible types of walls are considered. Fluctuations in a (111)-step are assumed to introduce an intermediate configuration with an energy $E_{[1\bar{1}0]}^{331+DB}$. Necessary for all fluctuations are the interrupted atom rows (circles), with an energy W_0 .*

which is of the same order of magnitude as our experimental ratios of $E_{[1\bar{1}0]}^{hollow}/W_0 = 0.019$ and $E_{[1\bar{1}0]}^{solid}/W_0 = 0.015$. The solid lines are obtained, if the excited state of a (111)-step, with an energy of $E_{[1\bar{1}0]}^{331+DB}$, and the two types of truncated walls are forbidden completely, i.e. if

$$E_{[1\bar{1}0]}^{331+DB} = E_{[1\bar{1}0]}^{tr.-hollow} = E_{[1\bar{1}0]}^{tr.-solid} = \infty.$$

The dashed lines are obtained for the specific choice that

$$E_{[1\bar{1}0]}^{331+DB} = 2E_{[1\bar{1}0]}^{111} \quad \wedge \quad E_{[1\bar{1}0]}^{tr.-hollow} = E_{[1\bar{1}0]}^{tr.-solid} = 3E_{[1\bar{1}0]}^{111}.$$

There are two observations, which indicate that the more appropriate choice of energies is the first one, with the intermediate structures forbidden. Firstly, we have never observed that the two atom rows of a single kink in a (111)-step split: so we never saw the excited intermediate state that is assumed by VV. This is also confirmed by Hoogeman et al. [70], who quantified the kink dynamics on Au(110) and saw that the maximum length of the excited state (with the energy $E_{[1\bar{1}0]}^{331+DB}$) is precisely one atomic spacing. Secondly, in only 7 of 576 crossing site observations there were more than 2 different domain boundaries present at the same time. We conclude that there has to be a substantial energy penalty for the unbinding of a kink into two single atom rows. Therefore, the transition temperatures should be described best by the case of forbidden intermediate structures. Using the VV theory [61], we calculate the phase diagram, figure 5.14b, for $E_{[1\bar{1}0]}^{111} = 3.7$ meV, $W_0 = 100$ meV, and forbidden intermediate structures as a function of the hollow or solid wall energy (assumed equal). Notice, that the VV theory breaks down closed to the ‘triple’-point, since it does not take into account the coupling of the transitions as is worked out in the theory of Den Nijs [62].

Table 5.2 lists the transition temperatures for three domain boundary energies, reflecting $E_{[1\bar{1}0]}^{hollow} = 1.9$ meV and its error margin.^x The deconstruction temperatures

^xWe neglect the error margin in $E_{[1\bar{1}0]}^{111}$ and W_0 .

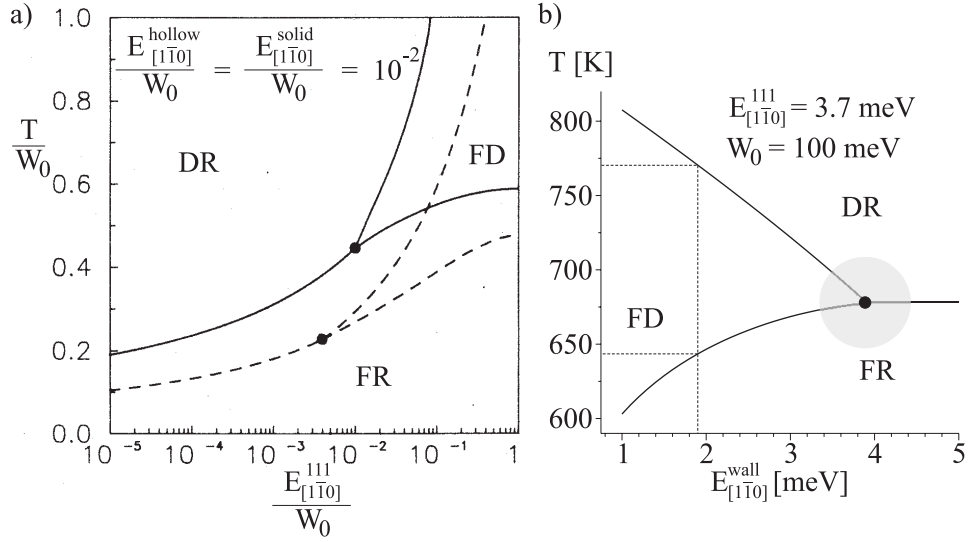


Figure 5.14: Phase diagrams of the VV theory. FR stands for the flat reconstructed phase, FD for the disordered flat phase, and DR for the disordered rough phase. (a) The solid lines are obtained if $E_{[1\bar{1}0]}^{331+DB} = E_{[1\bar{1}0]}^{tr.-hollow} = E_{[1\bar{1}0]}^{tr.-solid} = \infty$ and the dashed lines if $E_{[1\bar{1}0]}^{331+DB} = 2E_{[1\bar{1}0]}^{111}$ and $E_{[1\bar{1}0]}^{tr.-hollow} = E_{[1\bar{1}0]}^{tr.-solid} = 3E_{[1\bar{1}0]}^{111}$ (reprinted with permission [61]). (b) Calculated via the VV theory for the case of $E_{[1\bar{1}0]}^{111} = 3.7$ meV, $W_0 = 100$ meV and $E_{[1\bar{1}0]}^{331+DB} = E_{[1\bar{1}0]}^{tr.-hollow} = E_{[1\bar{1}0]}^{tr.-solid} = \infty$.

compare well with the experimental values, which fall in the range $650K \leq T_d \leq 765K$ [72]. However, it seems that our roughening temperatures slightly overestimate the typical difference of 50 K between T_d and T_r , reported in the literature [64].

$E_{[1\bar{1}0]}^{hollow}$	T_d	T_r
0.9 meV	596 K	812 K
1.9 meV	643 K	770 K
2.9 meV	667 K	726 K

Table 5.2: Phase transition temperatures, calculated via the VV theory [61], for $E_{[1\bar{1}0]}^{111} = 3.7$ meV and $W_0 = 100$ meV and three wall energies, reflecting $E_{[1\bar{1}0]}^{hollow} = 1.9$ meV and its error margin, see also fig. 5.14b.

Despite the fact that we have observed the formation of domain boundaries at crossing and termination sites, we emphasise that this *does not* represent the initial stage of deconstruction on the ideal Au(110)-surface, without the step networks. In fact, even for a misoriented surface, which develops domain boundaries, such as

found here, we expect the width of the half-order diffraction spots in the LEED-pattern to remain unchanged during the transformation of both the crossing and the termination sites from point to line contacts.

The diffraction spots should lose their sharpness only at temperatures close to the transition temperature for the perfectly oriented Au(110)-surface. Due to the structure of the network, areas with different phases of the MRR are located directly next to each other. Before and after the formation of the domain boundaries at the termination and the crossing sites, these average areas are not reduced by the boundary formation. The ‘real’ deconstruction transition introduces extra domain boundaries within the initially single-phase regions of the MRR. In chapter 8 we artificially create a structure that exactly does this: solid and hollow walls are introduced within the single-phase regions of the MRR. Nevertheless, the domain boundaries that are formed in the networks at the termination and crossing sites might serve as nucleation centers for new domain boundary loops at elevated temperatures.

5.7 Summary

In summary, STM observations of the Au(110) surface show the spontaneous formation of domain boundaries at temperatures well below the deconstruction transition temperature. We observed each of the four possible types of domain boundaries, namely the hollow wall, the solid wall, the truncated hollow wall, and the truncated solid wall. However, at termination sites only hollow walls were formed and at the crossing sites mainly hollow and solid walls were formed. The fact that the termination sites form exclusively hollow walls was shown to be a direct consequence of the atomic geometry of the termination site. The preference for solid and hollow walls over the corresponding truncated structures is indicative for a relatively high formation energy of the truncated hollow and the truncated solid wall. The length distributions of domain boundaries at the termination sites were fitted by a simple exponential, from which a first estimate of $E_{[1\bar{1}0]}^{hollow}$ was obtained. The length distribution of the domain boundaries at the crossing sites were described by a model that includes both the change in free energy of the step network and the elastic step-step-interactions. From the fits we obtained the energies of a hollow and a solid wall to be $E_{[1\bar{1}0]}^{hollow} = 1.9 \pm 1.0$ meV and $E_{[1\bar{1}0]}^{solid} = 1.5 \pm 2.0$ meV, respectively. By applying the theory of Villain and Vilfan [61] to our experimentally determined hollow wall energy, (111)-step energy, and [001]-step energy (which equals the kink energy in a (111)-step; see chapter 6), we estimate the deconstruction and roughening transition temperatures to be $596K \leq T_d \leq 667K$ and $812K \geq T_r \geq 726K$, respectively. Both of these values are in the range of published experimental transition temperatures [59, 63, 64, 82, 97]. From the energies determined in this chapter, we conclude that the Au(110)-surface should undergo two separate phase transitions, first deconstruction and then roughening.

Chapter 6

(A)symmetric ‘Cigars’

Symmetric shape of vacancy islands

The almond-like equilibrium shape of vacancy and adatom islands on Au(110) was already introduced in chapter 3. This shape results from the avoidance of both the higher-energy (331)-steps and the domain boundaries. In contrast with this, we show in this chapter that the removal of 0.2 monolayers (ML) of a clean, well-ordered surface at room temperature leads to the formation of vacancy islands with two different types of steps along the $[1\bar{1}0]$ -direction: a (111)-step on one side and a (331)-step on the other side. We consider the consequences of this broken mirror symmetry. In the Wulff construction, the ratio of any two step free energies is equal to the ratio of the distances of corresponding steps on the island contour to the origin of the polar plot of the step free energy (Wulff diagram). Since there is a difference in formation energy between the (111)- and the (331)-step, the origin of the polar plot does not coincide with the center of (missing) mass of the vacancy island. Applying the Wulff construction to an asymmetric step free energy plot, one expects to obtain an asymmetric island shape. However, we show that a shape asymmetry cannot occur as a result of the difference in the step free energies. On the other hand, asymmetry can be caused by a difference in formation energy between kinks in the (111)-steps and kinks in the (331)-steps. We employ the kink statistics in the observed vacancy islands to show that these kink energies are virtually identical and come to the surprising consequence that the islands have a two-fold symmetric shape, in spite of their structure with only one-fold symmetry.

6.1 Vacancy Islands with Broken Mirror Symmetry

In chapters 3 and 4 we have seen that the equilibrium shape of vacancy and adatom islands is completely determined by the orientation dependence of the step free energy via the Wulff construction (see also section 2.3) [23, 24, 74, 106]. Since the origin of the polar plot of the step free energy (Wulff point) coincides with the center of mass of the island, the island shape itself reflects the symmetry of the underlying crystal. For example, the quasi-hexagonal islands with A- and B-type steps on (111) f.c.c. surfaces exhibit the threefold symmetry of both the f.c.c. crystal and the (111)-surface [21]. The macroscopic almond-like equilibrium shape (chapter 3) of islands on Au(110) reflects the two-fold symmetry of the crystal and the surface. Both have two mirror planes, namely (001) and $(1\bar{1}0)$ (see also fig 2.6a).

However, we have obtained vacancy islands with only one-fold mirror symmetry after mild sputteringⁱ of a clean, well-ordered Au(110)-surface (appendix A) at room temperature. These 1 ML deep vacancy islands have an average width of 40 Å and an average length of 100 Å. We find that *all* vacancy islands have a MRR in their interior (figs. 6.1 a,b). This even holds for the narrowest islands, which have a width of a single MRR period (8.2 Å). As a consequence of the internal MRR, the vacancy

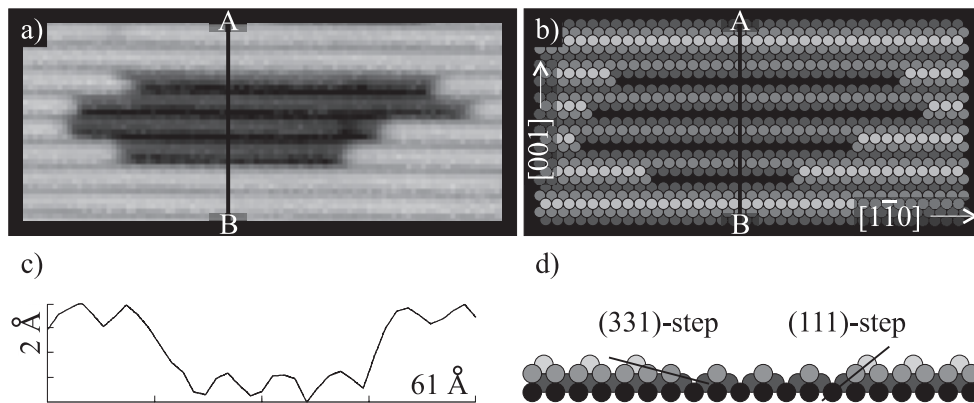


Figure 6.1: (a) *STM-image of a vacancy island; the internal MRR is visible.* (b) *Schematic top view of a vacancy island with a width of 4 MRR periods.* (c) *Line scan along A-B in panel a; the (331)- and the (111)-step can be easily distinguished, due to their different slopes. The rows in the interior are placed asymmetrically with respect to its surroundings.* (d) *Schematic cross-section along A-B in panel b.*

islands have a broken internal mirror symmetry: one of the steps along the MR-direction has to be a (111)-step (lower step in fig. 6.1 a,b), while the opposite one has to be a (331)-step (upper step in fig. 6.1 a,b). This asymmetry, which is schematically

ⁱWe removed 0.2 ML with 600 eV Ar⁺ ions.

indicated in the cross section of fig. 6.1d, can clearly be recognised in the line scan of fig. 6.1c (notice the different slopes of the two steps and the asymmetric placement of the MRR in the island with respect to its surroundings).

In ref. [107], Günther et al. mention the formation of missing row reconstructed adislands by gold deposition on Au(110) at 298 K. We expect these islands to exhibit the same broken mirror symmetry as our vacancy islands.

6.2 Asymmetric Equilibrium Shape?

Having verified that the vacancy islands have a contour with a structure that has only a single symmetry plane, we now turn to the symmetry of the island shape. The equilibrium shape of an island is related to the step free energy via the Wulff construction, as discussed in section 2.3 and chapter 4. In this construction, the free energy ratio of two steps, which are present in the island shape, is equal to the distance ratio of these steps from the origin of the polar free energy plot (Wulff point). As a consequence of the large difference in formation energy between the (111)- and (331)-steps, on opposite sides of the vacancy islands, $E_{[\bar{1}\bar{1}0]}^{111} = 3.7 \pm 0.5 \text{ meV/atomic spacing}$ and $E_{[\bar{1}\bar{1}0]}^{331} = 15.3 \text{ meV/atomic spacing}$ (see chapter 3.1.3), the center of missing mass of the vacancy island *no longer* coincides with the origin of the polar plot. Therefore, it seems natural to expect that also the average perimeter of the vacancy islands exhibits only one-fold mirror symmetry, and that it is asymmetric along the [001]-direction (cross section A→B in fig. 6.1). However, as we will see in section 6.3, STM observations show that the average shape of these vacancy islands is completely symmetric!

6.2.1 Asymmetry due to Difference in Step Energies?

Since a (331)-step segment has a higher formation energy than a (111)-step segment there is a higher driving force for reducing the (331)-step length than for reducing the (111)-step length. Let L denote the total length of an island along the $[\bar{1}\bar{1}0]$ -direction,

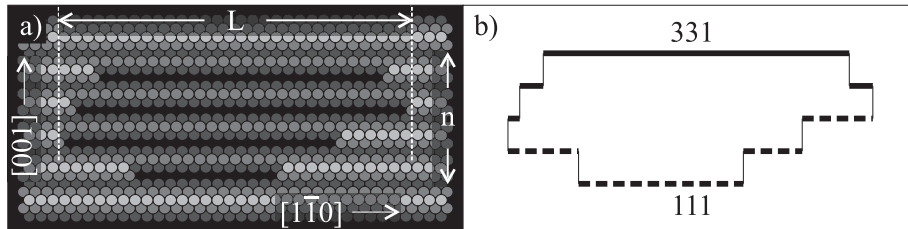


Figure 6.2: Schematic top views of a vacancy island with a length of L atomic spacings and a width of $n = 4$ missing MRR periods. (a) atomic model (b) line model; the thick lines denote (331)-steps and the dashed lines the (111)-steps.

measured in atom spacings (see fig. 6.2a). The island contains precisely L (331)-step segments as well as L (111)-step segments. Thus, it is impossible to reduce the length of the higher-energy (331)-step *without* shortening the (111)-step length by exactly the same amount. As a consequence, the average island contour *will not become asymmetric* due to a difference in the step formation energies $E_{[1\bar{1}0]}^{111}$ and $E_{[1\bar{1}0]}^{331}$!

6.2.2 Asymmetry due to Difference in Kink Energies?

Since there are two types of steps, there are also two different types of kinks: (331)-kinks and (111)-kinks, with energies denoted by E_K^{331} and E_K^{111} . If E_K^{331} were lower

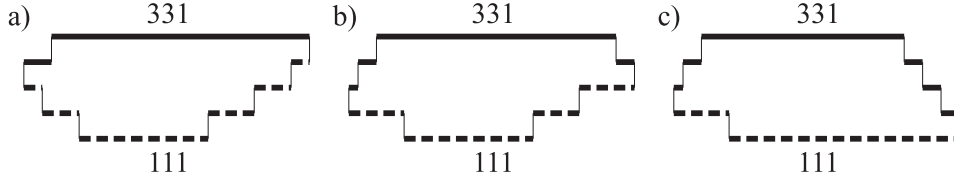


Figure 6.3: Schematic top views of characteristic examples of vacancy islands in the case of different kink energies: (a) $E_K^{331} > E_K^{111}$ (b) $E_K^{331} \simeq E_K^{111}$ (c) $E_K^{331} < E_K^{111}$

than E_K^{111} , the vacancy islands would contain, on average, more (331)-kinks than (111)-kinks, and vice versa (see fig. 6.3). Differences in kink densities at the two steps will make one side of the island more rounded and the other more straight. The kink energies, therefore, *do* provide a possibility for an asymmetric contour.

6.3 Determination of the Kink Energies

In this section we analyse a large number of STM observations of vacancy islands on Au(110) in order to quantify the difference in energy between (111)- and (331)-kinks, and, thus, the asymmetry of the islands.

To derive an expression for the total energy of a vacancy island we approach the kink energy as described in [80]. The idea is to split the energy of each kink E_K^{hkl} into two contributions $E_K^{hkl} = E_{[001]} + C_K^{hkl}$ (see fig. 6.4), where $E_{[001]} = 200 \pm 60$ meV/MRR period (see section 3.1.3) represents the energy of the short [001]-oriented step segment perpendicular to the (111)- or (331)-step, which forms part of every kink, and C_K^{hkl} is the combined energy of the kink’s two corners (convex and concave). If n represents the width of the island in units of the MRR period (see fig. 6.2a) the formation energy of the complete vacancy island can be written as

$$E = L \cdot (E_{[1\bar{1}0]}^{111} + E_{[1\bar{1}0]}^{331}) + 2nE_{[001]} + aC_K^{111} + bC_K^{331} \quad (6.1)$$

where a and b denote the numbers of (111)- and (331)-kinks and $a+b \leq 2n-2$.

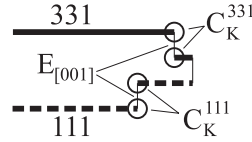


Figure 6.4: Schematic top view of a (331)- and a (111)-kink illustrating the corner and step segment energies.

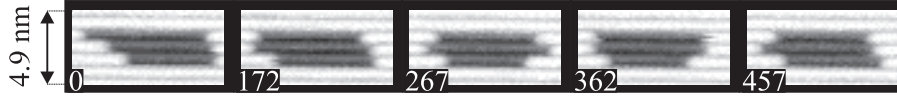


Figure 6.5: STM images taken from a movie at room temperature; the time in sec. is indicated at each image.

Figure 6.5 shows a sequence of STM pictures of a vacancy island with $n = 3$. These images have been taken from a movie measured at room temperature. The total area of the vacancy island stays, on average, constant. The individual missing atom rows fluctuate both in relative position and in length. Although we observe these position and length fluctuations, none of the islands fluctuated in width at $T < 343 \text{ K}$ ⁱⁱ. This is probably due to the high activation barrier for removing an atom from an intact atom row, which would be necessary to initiate the next missing row. Nevertheless, the combination of the observed position and length fluctuations allows each island to ‘play’ with the number of (111)-kinks, a , and (331)-kinks, b . We have counted the numbers of kinks in 56 STM-images, taken at room temperature, and each containing 9 vacancy islands. In total, we obtained: $a = 716$ (111)-kinks and $b = 722$ (331)-kinks.

If we assume that each observed kink in an island could have been either a (331)-kink or a (111)-kink, the ratio of their abundances is expected to be equal to the ratio of their Boltzmann weights:

$$\frac{a}{b} = e^{-\Delta E_K/k_B T} = e^{-\Delta C_K/k_B T} \quad (6.2)$$

where k_B is the Boltzmann constant and T the temperature. Since the observed ratio is so close to unity, we estimate that

$$\begin{aligned} \Delta E_K &= |E_K^{111} - E_K^{331}| = |(E_{[001]} + C_K^{111}) - (E_{[001]} + C_K^{331})| \quad (6.3) \\ &= |\Delta C_K| \leq 0.2^{+1.0}_{-0.2} \text{ meV} \leq 1.2 \text{ meV} \end{aligned}$$

We set this result into perspective by comparing it with the total kink energies, E_K^{111} and E_K^{331} . Since $E_{[001]} = 200 \text{ meV}$ per MRR period we conclude that the kink energies are equal within an uncertainty of $\pm 0.6 \%$.

ⁱⁱIn a few cases, we observed an island decreasing its width, but this was always irreversible.

We can come to the same conclusions by reviewing a measurement published earlier by Hoogeman et al. [70]. They measured the probability distribution of the distance l between two neighbouring kinks in a (111)-step. Three different types of configuration can be distinguished for these kink pairs. These are shown with their corresponding energies in fig. 6.6. In the first type of configuration, the piece of step between the kinks is of the (111)-type. In the intermediate, second type, the two kinks are perfectly aligned. In the third type of configurations, the kinks form an ‘overhang’ or ‘parallel fluctuation’ (see chapter 4), and enclose a (331)-type section. Figure 6.7

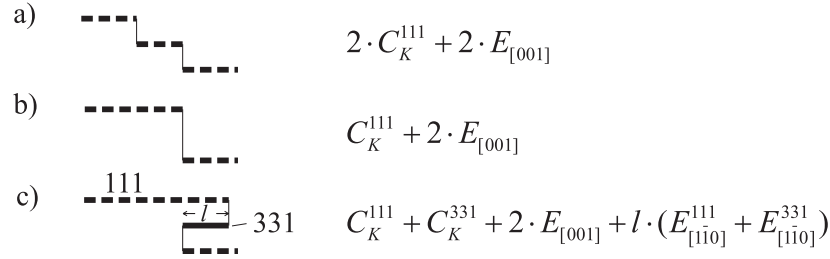


Figure 6.6: *Three different kink-pair configurations in a (111)-step: (a) $l < 0$, kink pair with no overhang; (b) $l = 0$, kink of double width; (c) $l > 0$, kink pair with overhang length l . The corresponding energies are indicated to the right of each configuration.*

shows the frequency distribution of l , where positive l -values correspond to the third type of configuration, i.e. overhangs. The distribution shows a plateau for negative l and an exponential decrease for positive l (note the semi-log. scale). The fact that the frequency is independent of l directly shows that all configurations of the first type (no overhang) have the same formation energy, as expected from our simple model of step and kink energies, and as illustrated in fig. 6.6a. The exponential decrease of the frequency for positive l shows that the formation energy of all configurations of the third type (with overhang) carry a positive contribution, proportional to l , again in good agreement with our model for the energetics of Au(110) (see fig. 6.6c). There are two important pieces of information left in fig. 6.7, which had not been recognised explicitly by Hoogeman et al. [70]. The fact that the straight-line fits for $l < 0$ and $l > 0$ intersect precisely at $l = 0$ is again direct evidence that the difference in kink energy, $|C_K^{331} - C_K^{111}|$, must be very small, since it implies that (cf. figs. 6.6 a,c):

$$2C_K^{111} + 2E_{[001]} = C_K^{111} + C_K^{331} + 2E_{[001]} \quad (6.4)$$

The fact that the observed frequency for $l = 0$ lies on both straight lines (for $l < 0$ and for $l > 0$), further shows that the corner energies are not only equal, but that they are both close to zero (cf. figs. 6.6 a,b):

$$2C_K^{111} + 2E_{[001]} = C_K^{111} + 2E_{[001]} \quad (6.5)$$

From this we obtain $C_K^{111} = C_K^{331} = 0 \pm 3.6 \text{ meV}$ ⁱⁱⁱ. It is probable that the MRR decouples the surface atom rows sufficiently to make the corner energies insignificantly low. This reduces both kink energies to the energy of a step segment perpendicular

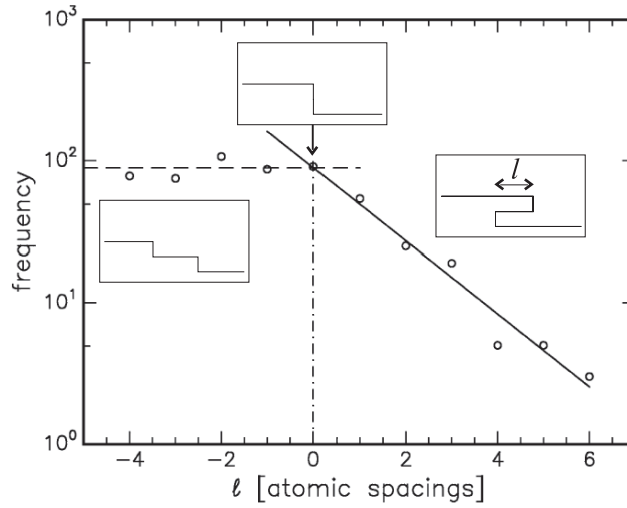


Figure 6.7: *Semi-log plot of the measured number of observations of distance l between two kinks in a (111)-step on Au(110), obtained from an STM movie of a kink pair at 380 K. (reprinted with permission from [70]).*

to the MR-direction: $E_K^{111} = E_K^{331} = E_{[001]} = 200 \pm 60 \text{ meV}$ (see subsection 3.1.3).

ⁱⁱⁱStatistical error margin of the data point at $l = 0$ in fig. 6.7.

6.4 Summary: Symmetric Averaged Island Shape!

As argued in section 6.2, a difference in the (111)- and (331)-step free energies will not cause an asymmetric island shape on Au(110). In principle, a difference in kink energies will make the equilibrium shape asymmetric. However, the measured kink statistics shows that the energies of (111)- and (331)-kinks are equal within 0.6%. Combining these two results we come to the unexpected conclusion that the average contour of vacancy islands with a broken internal symmetry on Au(110) is completely symmetric!

It is tempting to apply the *inverse* Wulff construction to the observed island shape, to derive the full orientation dependence of the step free energy. However, without prior knowledge of $E_{[1\bar{1}0]}^{111}$ and $E_{[1\bar{1}0]}^{331}$ the location of the Wulff point is unknown (since it does *not* coincide with the island centre) and this construction cannot be performed! In addition, the Wulff construction requires the average island shape to reflect thermodynamic equilibrium, which can be verified principally by observing fluctuations in the shape of individual islands. As illustrated by fig. 6.5, the individual missing rows of the islands fluctuated in length and position, but the islands did not fluctuate in width. The lack of width fluctuations does not necessarily imply that the vacancy islands could not reach thermal equilibrium, as they could still vary in length (area) and thereby in aspect ratio, via vacancy or adatom exchange with the terrace. Nevertheless, we will not draw further conclusions from the islands’ average shape.

6.5 Outlook

It is rather challenging to calculate the orientation dependent step free energy for a model of this particular case, which we will do in chapter 7. Applying the Wulff construction to the calculated orientation dependent step free energy verifies our result of a symmetric average contour of islands with a broken internal symmetry. Furthermore, we derive the general requirements for obtaining a 2-fold symmetric average island contour from a 1-fold symmetric step free energy plot, and show that the Au(110)-surface does, indeed, fulfill these requirements. In chapter 8 we will show that the vacancy islands observed here are metastable, and that they can transform in several ways to more symmetric, lower-energy configurations.

Our observations were possible as a result of the artificial creation of vacancy islands on this particular surface. We expect to find analogous shapes and structures for adatom and vacancy islands on other surfaces that exhibit a broken symmetry due to a MRR, for example, Pt(110) and Ir(110). Gas adsorption can induce or lift reconstructions on other metal surfaces, leading to several further possible realisations of islands with broken symmetry.

Chapter 7

Theory for the (A)symmetric 'Cigars'

Step free energy and Wulff construction

Vacancy islands on Au(110) with a broken internal symmetry were introduced in chapter 6: steps on opposite sides are of different types. We have seen that this symmetry breaking is not reflected in the average contour of these islands; the equilibrium shape was completely symmetric. In this chapter, we extend the step free energy calculations of chapter 4 for symmetric islands to the case of islands with broken symmetry. Applying the Wulff construction to the asymmetric polar diagram of the step free energy we indeed obtain a symmetric equilibrium shape. We formulate the general condition for obtaining a symmetric equilibrium shape on the basis of an asymmetric step free energy polar plot. In addition, we discuss the variations of the equilibrium shape as a function of temperature.

7.1 Symmetric Contour of the Asymmetric Islands

In chapter 3, we have seen that the formation energy of a (111)-step is more than four times as low as that of a (331)-step. Thus, in the polar free energy plot, the distance from the origin (Wulff point) to the (111)-step (free energy) will be shorter than the distance to the (331)-step (free energy). As a consequence, the Wulff plot cannot have mirror symmetry with respect to the $[1\bar{1}0]$ axis through the Wulff point.ⁱ If we apply the Wulff construction, we can never obtain an average island contour that is symmetric with respect to this axis, and one may therefore expect to find an asymmetric island shape.

When the step free energy is different for two different step orientations, the island shape usually reflects this, with the lower-energy step orientation represented more prominently than the other one. Therefore, we might expect to find more of the (111)-step than of the (331)-step in the vacancy islands on Au(110). However, since these two types of steps are located on opposite sides of the island, both steps simply must have the same length. This means that the islands cannot adopt an asymmetric contour as a consequence of the difference in the energies of (111)-steps and (331)-steps (from here on, we will use the word "symmetry" to indicate mirror symmetry with respect to the $[1\bar{1}0]$ -direction). The only way for the island to break its symmetry

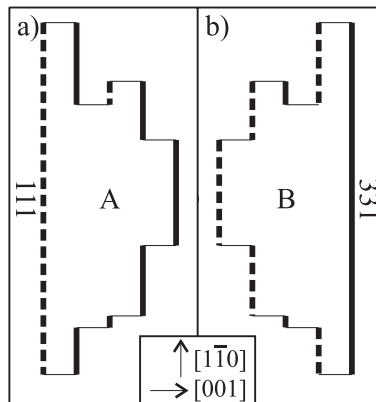


Figure 7.1: In each of the two mirrored vacancy islands in (a) and (b) the total length of (331)-step is identical to the total length of (111)-step. Therefore, the total energies of the $[1\bar{1}0]$ -oriented parts of the steps of islands A and B are equal. If the energies of the (331)- and (111)-kinks are equal, the two islands have the same total formation energy. In that case, every island shape will occur with the same frequency as its mirror image and the average island contour will be symmetric.

ⁱVan Beijeren and Nolden [77] have obtained the Wulff construction for the peculiar case that a range of step orientations has a negative step free energy. They found that in that case the Wulff point lies even outside the equilibrium shape.

is to have more kinks on one side of the island than on the other (fig. 7.1). This can happen as the consequence of a difference in kink energies. If, for example, the formation energy of a (331)-kink, E_K^{331} , were lower than that of a (111)-kink, E_K^{111} , each island would on average contain more (331)-kinks, making shapes like the one in fig. 7.1a more favorable than shapes like in fig. 7.1b. In this case, the average island shape would be more rounded on the (331)-side and straighter on the (111)-side.

In chapter 6 we have seen that the average island shape is symmetric [90]. Both types of kink appear with the same frequency. From the numbers of kinks counted in the STM-images, the two kink energies were calculated to be equal within 1.2 meV, which is six permille of the total kink energy. Of course, asymmetric island shapes like fig. 7.1a do occur, but their mirror images (fig. 7.1b) occur with precisely the same frequency, because the two shapes have the same formation energy. It is the *average* island shape, which is symmetric.

Still, the polar free energy plot is asymmetric! How can an *asymmetric* polar step free energy plot produce a *symmetric* island contour? This counterintuitive situation is illustrated in fig. 7.2. The Wulff construction in fig. 7.2 has some remarkable

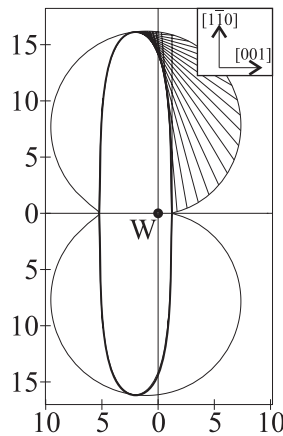


Figure 7.2: The symmetric contour of a vacancy island on the (1×2) MRR Au(110)-surface, obtained via the Wulff construction of an asymmetric polar free energy plot. The energies are expressed in $\text{meV}/\text{\AA}$. The directions of the $[1\bar{1}0]$ and $[001]$ steps are indicated by the arrows.

characteristics. The construction is very asymmetric: the Wulff point W lies at a large distance from the island centre. Yet, the island shape is perfectly symmetric. The polar free energy plot is also very asymmetric with respect to the Wulff point. For example, the minimum on the right is much deeper than the one on the left. At first sight, the polar energy plot may look symmetric with respect to a displaced origin, like the island shape, but this is not the case. The island contour and the polar free energy plot coincide in four points. The first two lie on the short axis of the polar plot. The other two points do not lie on the long axis of the plot, but a little distance

to the left of it. These two points coincide with the highest values of the step free energy.ⁱⁱ

Figure 7.3 demonstrates how the symmetry in the island contour arises. The cen-

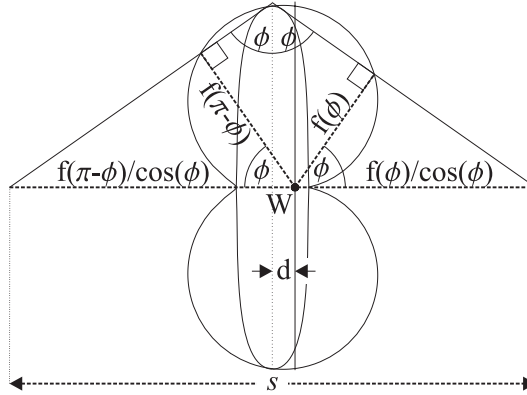


Figure 7.3: Condition on the step free energy to produce a symmetric island contour via the Wulff construction. As derived in the text, when the condition $f(\pi - \phi) = f(\phi) + 2d \cos(\phi)$ is satisfied for all angles ϕ , the shape of the island is mirror symmetric with respect to a symmetry axis at a distance d from the Wulff point W .

tre (symmetry point) of the island contour lies at a distance d from the Wulff point W . To find the condition for shape symmetry, we apply the inverse Wulff construction to the island shape. Let us select two points on the symmetric island contour: one arbitrary point and its mirror image with respect to the island’s symmetry axis. Through these two points lines are drawn tangential to the island. These two lines run under the same angle ϕ with respect to the symmetry axis, because of the required symmetry. Next, we draw two lines, perpendicular to the tangent lines, which both intersect the Wulff point. The indicated lengths along these perpendicular lines are proportional to the free energies $f(\phi)$ and $f(\pi - \phi)$ of steps with orientations represented by normal vectors at angles ϕ and $\pi - \phi$ with the horizontal axis. The complete polar step free energy plot is constructed by repeating this operation for all angles ϕ . The symmetry condition can now easily be formulated in terms of the width s indicated in fig. 7.3. On the one hand,

$$s = \{f(\pi - \phi) + f(\phi)\} / \cos(\phi) \quad (7.1)$$

ⁱⁱWhen the Wulff construction is applied, first, a line piece is drawn from the Wulff point to a point on the polar step free energy plot. From this point, a line is drawn perpendicular to the first one. The distance along this line between the point on the polar plot and the place where it touches the island contour, is proportional to the derivative of the step free energy with respect to the orientation angle of the step [75, 91]. The derivative is zero in the extrema of the step free energy, so the island contour and the polar plot coincide in these points.

while, on the other hand, the symmetry requires

$$s = 2\{d + f(\phi)/\cos(\phi)\} \quad (7.2)$$

If we combine eqs. 7.1 and 7.2, it follows that the Wulff construction produces a symmetric island with a distance d between the island center and the Wulff point, if for all angles ϕ

$$f(\pi - \phi) = f(\phi) + 2d \cos(\phi) \quad (7.3)$$

This may seem a very peculiar condition, but, as we show in the next section, it is relatively easily satisfied on Au(110) and similar surfaces.

7.2 Step Free Energy of Asymmetric Islands

We can easily extend the free energy equations (eqs. 4.6, 4.7, 4.14, and 4.17) that have been derived in chapter 4 for islands with (111)-type steps on both sides to the case of the islands observed in chapter 6. Since the latter islands have a (331)-step at one side and a (111)-step at the opposite side, the ground state energy part of eq. 4.6 has to be modified, which makes it depend also on $E_{[1\bar{1}0]}^{331}$:

$$\begin{aligned} & e_{ground}(E_{[1\bar{1}0]}^{111}, E_{[1\bar{1}0]}^{331}, E_{[001]}, \phi) \\ &= \frac{E_{[001]}}{2a} |\sin \phi| + \frac{E_{[1\bar{1}0]}^{111} - E_{[1\bar{1}0]}^{331}}{\sqrt{2}a} \cos \phi + \frac{E_{[1\bar{1}0]}^{111} + E_{[1\bar{1}0]}^{331}}{\sqrt{2}a} |\cos \phi| \quad (7.4) \end{aligned}$$

Notice that we choose $\phi = 0$ for a (111)-step and $\phi = \pi$ for a (331)-step. For $-\pi/2 < \phi < \pi/2$, the ground state configuration consists of only (111)-step segments and [001]-step segments. For these angles, we associate ϵ_x with $E_{[001]}$ and ϵ_y with $E_{[1\bar{1}0]}^{111}$ in the ground state energy (eq. 4.4). For $\pi/2 < \phi < 3\pi/2$ the ground state configuration consists of only (331)-step segments and [001]-step segments, so that we substitute ϵ_y with $E_{[1\bar{1}0]}^{331}$, while ϵ_x still stands for $E_{[001]}$ in eq. 4.4. The fluctuation contribution remains unchanged, with respect to that in eq. 4.6. As a result we find for the step free energy of asymmetric (vacancy) islands on the missing row reconstructed surface:

$$\begin{aligned}
& f_{MR}(E_{[1\bar{1}0]}^{111}, E_{[1\bar{1}0]}^{331}, E_{[001]}, \phi, T) \\
&= e_{ground}(E_{[1\bar{1}0]}^{111}, E_{[1\bar{1}0]}^{331}, E_{[001]}, \phi) + f_{fluct}(E_{[1\bar{1}0]}^{111}, E_{[1\bar{1}0]}^{331}, E_{[001]}, \phi, T) \\
&= \left(\frac{E_{[001]}}{2a} |\sin \phi| + \frac{E_{[1\bar{1}0]}^{111} - E_{[1\bar{1}0]}^{331}}{\sqrt{2}a} \cos \phi + \frac{E_{[1\bar{1}0]}^{111} + E_{[1\bar{1}0]}^{331}}{\sqrt{2}a} |\cos \phi| \right) \\
&\quad + \left(f_{rect}((E_{[1\bar{1}0]}^{111} + E_{[1\bar{1}0]}^{331})/2, E_{[001]}, \phi, T) - \frac{E_{[001]}}{2a} |\sin \phi| \right. \\
&\quad \quad \quad \left. - \frac{E_{[1\bar{1}0]}^{111} + E_{[1\bar{1}0]}^{331}}{\sqrt{2}a} |\cos \phi| \right) \\
&= \frac{E_{[1\bar{1}0]}^{111} - E_{[1\bar{1}0]}^{331}}{\sqrt{2}a} \cos \phi + f_{rect}((E_{[1\bar{1}0]}^{111} + E_{[1\bar{1}0]}^{331})/2, E_{[001]}, \phi, T) \quad (7.5)
\end{aligned}$$

The fluctuation term f_{fluct} represents the free energy per unit length involved in the variations in configuration for a step with average orientation ϕ . The precise definition can be found in chapter 4. The term f_{rect} is the free energy per unit length of a step with orientation ϕ on a rectangular lattice, in this case with the (effective) step segment energies $\frac{1}{2}(E_{[1\bar{1}0]}^{111} + E_{[1\bar{1}0]}^{331})$ along the $[1\bar{1}0]$ -direction and $E_{[001]}$ along the perpendicular $[001]$ -direction, as introduced in more detail in chapter 4. Since f_{rect} is, by definition, symmetric with respect to the $[1\bar{1}0]$ -orientation, i.e. $f_{rect}(\pi - \phi) = f_{rect}(\phi)$, it follows from eq. 7.5 in combination with eq. 7.3 that the Wulff construction on our model MRR-surface produces a symmetric island shape with a ‘distance’ $d = \frac{E_{[1\bar{1}0]}^{331} - E_{[1\bar{1}0]}^{111}}{\sqrt{2}a}$ between the island center and the Wulff point, irrespective of the specific model employed for f_{rect} .

In the next sections, we calculate the step free energy for the three models of f_{rect} , introduced before in chapter 4.

7.2.1 Two-Dimensional Ising Model

First, we calculate the step free energy on Au(110) using the two-dimensional anisotropic Ising model, in which both parallel and perpendicular fluctuations are allowed. In complete analogy with eq. 4.7, we combine eq. 7.5 with eq.3 of ref. [76] to obtain:

$$\begin{aligned}
f_{Ising}(\phi) = & \frac{1}{2\beta a} \alpha_1 (\arctan(\frac{\tan \phi}{\sqrt{8}})) |\sin \phi| + \frac{\sqrt{2}}{\beta a} \alpha_2 (\arctan(\frac{\tan \phi}{\sqrt{8}})) |\cos \phi| \\
& + \frac{E_{[1\bar{1}0]}^{111} - E_{[1\bar{1}0]}^{331}}{\sqrt{2}a} \cos \phi \quad (7.6)
\end{aligned}$$

The functions $\alpha_1, \alpha_2, j, c, m$ and n have been defined in chapter 4 (see eqs. 4.8- 4.13).

7.2.2 Perpendicular Fluctuation Approximation

By adding the ground state energy of the asymmetric case (eq. 7.4) to the perpendicular fluctuation term (eq. 4.20) we obtain the step free energy in the perpendicular fluctuation approximation

$$f_{\perp}(\phi) = \frac{E_{[1\bar{1}0]}^{111} - E_{[1\bar{1}0]}^{331}}{\sqrt{2}a} \cos(\phi) + \left[\ln \bar{z}(\phi) \right] \frac{|\sin \phi|}{2\beta a} \quad (7.7)$$

$$+ \left[\beta \frac{E_{[1\bar{1}0]}^{111} + E_{[1\bar{1}0]}^{331}}{2} + \ln \left(\frac{2 \cosh(\beta E_{[001]}) - [\bar{z}(\phi) + 1/\bar{z}(\phi)]}{2 \sinh(\beta E_{[001]})} \right) \right] \frac{\sqrt{2}|\cos \phi|}{\beta a}$$

Where the function $\bar{z}(\phi)$ has been defined in eqs. 4.15, 4.16.

7.2.3 Parallel Fluctuation Approximation

Finally, by adding the ground state energy of the asymmetric case (eq. 7.4) to the parallel fluctuation term (eq. 4.21) we obtain the step free energy in the parallel fluctuation approximation

$$f_{\parallel}(\phi) = \frac{E_{[1\bar{1}0]}^{111} - E_{[1\bar{1}0]}^{331}}{\sqrt{2}a} \cos \phi + E_{[001]} \frac{|\sin \phi|}{2a} + \frac{\ln z(\phi) \sqrt{2}|\cos \phi|}{\beta a}$$

$$+ \ln \left(\frac{2 \cosh(\beta(E_{[1\bar{1}0]}^{331} + E_{[1\bar{1}0]}^{111})/2) - [z(\phi) + 1/z(\phi)]}{2 \sinh(\beta(E_{[1\bar{1}0]}^{331} + E_{[1\bar{1}0]}^{111})/2)} \right) \frac{|\sin \phi|}{2\beta a} \quad (7.8)$$

7.3 Temperature Dependence of Asymmetric Islands

The temperature dependent contour of the vacancy islands can be seen in fig. 7.4, for each of the three approximations to the step free energy. The contour shapes of the islands in fig. 7.4 are, for all temperatures, totally symmetric with respect to the same symmetry axis at a distance $d = (E_{[1\bar{1}0]}^{331} - E_{[1\bar{1}0]}^{111})/\sqrt{2}a$ from the Wulff point. At 0K the island shape is rectangular. For any nonzero temperature, there are no straight steps, steps being rough at all finite temperatures. When the temperature is increased, the shape initially becomes shorter, while the width stays (nearly) constant. At 600K, also a change in the width can be seen. When the temperature is increased even further, the step free energy of the (111)-step becomes zero. At that temperature, the surface can create (111)-steps without raising its free energy. As a consequence, the surface goes through the so-called roughening transition (see section 2.4). If the other phase transition of Au(110), the deconstruction transition (see chapter 5), takes place at a lower temperature, separate from the roughening transition, the roughening transition takes place on a deconstructed surface, the so-called disordered flat phase [108]. The model, treated here, is only valid for the (1x2)-reconstructed Au(110) surface, i.e. not for the disordered flat phase. It should therefore be expected to yield bad estimates for the roughening temperature.

In the next chapter we will address the stability and evolution of the asymmetric vacancy islands, from which we will conclude that the asymmetric structures are metastable.

7.4 Summary

In summary, we have considered the theory of equilibrium shapes for asymmetric (vacancy) islands on the (1x2) missing-row reconstructed Au(110) surface. They have an asymmetric structure, with a (331)-type step on one side, and a (111)-type step on the other. Although the Wulff point does not coincide with the centre of the island, the island shape observed in experiments is symmetric, which shows that (331)- and (111)-kinks are equal in energy. We have shown that an asymmetric polar step free energy plot can indeed produce an island with a symmetry axis at a distance d from the Wulff point, if the free energy $f(\phi)$ satisfies $f(\pi - \phi) = f(\phi) + 2d \cos(\phi)$ for every angle ϕ .

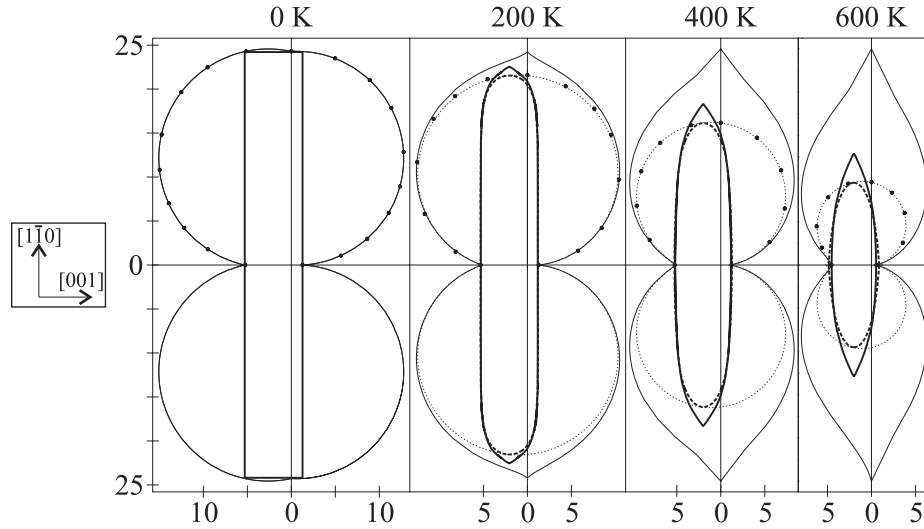


Figure 7.4: Wulff constructions for asymmetric islands, according to the Ising model and the parallel fluctuation approximation (dotted curves) and the perpendicular fluctuation approximation (solid curves), at different temperatures. The thin curves are the step free energies and the thick curves are the equilibrium island shapes. On this scale, the step free energy of the Ising model coincides with the combined inner contour of the free energy curves for the two solid-on-solid approximations. Similarly, the Ising island shape follows the inner contour of the two other island shapes. For all three models the shape is perfectly symmetric at all temperatures, although the left side is a (331)-type step and the right side a (111)-type step. The dots are the results of Monte Carlo calculations of the step free energy. The energies are indicated in $\text{meV}/\text{\AA}$. Step segment energies used in the calculations are: $E_{[\bar{1}\bar{1}0]}^{111} = 3.7\text{meV}$, $E_{[\bar{1}\bar{1}0]}^{331} = 15.3\text{meV}$ and $E_{[001]} = 200\text{meV}$, see chapter 3 [81]. The directions of the $[\bar{1}\bar{1}0]$ and $[001]$ steps are indicated by the arrows.

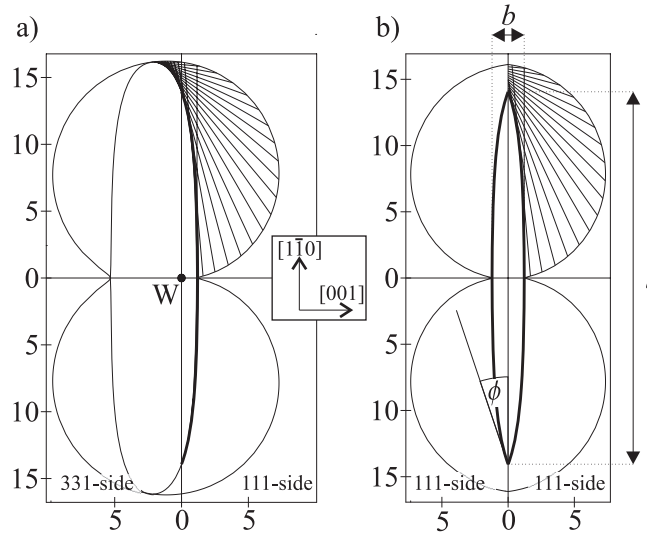


Figure 7.5: a) Wulff construction of an asymmetric vacancy island in Au(110) at $T=400\text{K}$, according to the Ising model. The stable equilibrium shape of islands on Au(110), with only (111)-type steps, can be obtained by mirroring the (111)-side (thick line) of the asymmetric Wulff construction in the (vertical) $[1\bar{1}0]$ -axis through the Wulff point. b) Wulff construction of the stable symmetric shape of adatom and vacancy islands for $T = 400\text{K}$ (see also chapter 4). The aspect ratio is defined as l/b and 2ϕ is the sharp angle of the almond-shaped island. The energies are expressed in $\text{meV}/\text{\AA}$. The directions of the $[1\bar{1}0]$ and $[001]$ steps are indicated by the arrows.

7.5 Relation between Asymmetric and Symmetric Islands

We close this chapter with a brief discussion of the relation between the symmetric island shapes, with (111)-type steps on both sides, and the asymmetric shapes, with a (331)-step on one of the two sides. Mathematically, the only difference between the step free energy expressions in this chapter for the asymmetric case and the expressions in chapter 4 for the symmetric islands is the replacement of factors $\cos(\phi)$ with $|\cos(\phi)|$. Graphically, this means that we can obtain the almond shape of the symmetric islands by mirroring the (111)-part (right side) of the step free energy plot and the island shape in the vertical, $[1\bar{1}0]$ -axis through the Wulff point. This is illustrated in fig. 7.5.

Chapter 8

Evolution of the (A)symmetric 'Cigars'

Vacancy islands can be formed on the Au(110)-surface with a broken internal mirror symmetry (chapter 6). In this chapter we will see that the coarsening of these islands proceeds via a variety of pathways. This unusual variety is a direct consequence of the broken symmetry. The different pathways involve rather different time scales for the coarsening. Most frequently, coarsening takes place in the form of coalescence. Often, two vacancy islands are observed to transform into a bound pair, which we identify as a new symmetric structure, which exclusively contains (111)-steps. Furthermore, we show that single vacancy islands with a width of one MRR period tend to spontaneously split themselves up into two 'vacancy lines', forming a symmetric line-pair. From the thermal fluctuations of the lines in such a pair, we determine the formation energy of this particular structure, and find that this is the lowest-energy vacancy configuration.

8.1 Observations

In chapter 6 we have seen that the removal of a submonolayer amount of Au, e.g. 0.2 MLⁱ, from a clean, well-ordered Au(110)-surface leads to the formation of vacancy islands with a depth of precisely 1 ML and a broken internal symmetry. The reason for the lack of symmetry is that all vacancy islands on Au(110) adopt a MRR in their interior, which makes one side a (111)-step and the opposite side a (331)-step. Here, we focus on the coarsening of these asymmetric islands.

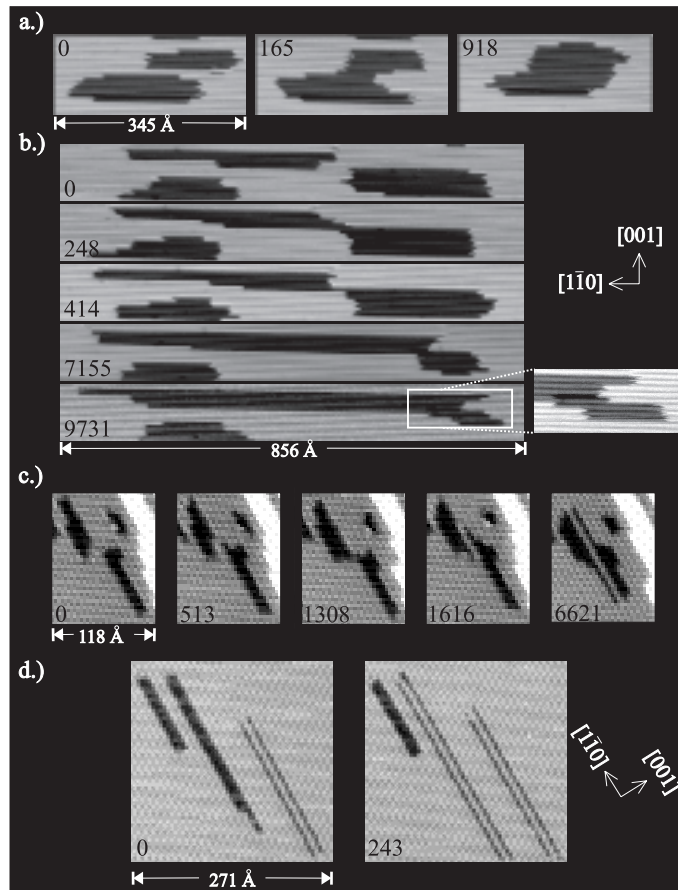


Figure 8.1: Coarsening sequences of vacancy islands. The time in seconds is indicated in each panel. (a) Normal coalescence; $T=343\text{K}$. (b) Slow coalescence; $T=343\text{K}$. (c) ‘Bound-pair’ formation; $T=293\text{K}$. (d) Transformation to a ‘bound line pair’; $T=343\text{K}$.

As mentioned in section 2.7, the evolution of surfaces with adatom and vacancy islands usually proceeds via either Ostwald ripening or coalescence dynamics. In

ⁱWe have sputtered the surface with 600 eV Ar^+ -ions.

both cases, the energetic driving force is simply the reduction in total step length. In contrast, the vacancy islands on Au(110) were found to exhibit a rich variety of evolution mechanisms, all active at the same temperatures. Apart from size fluctuations and Ostwald ripening effects, which led to the occasional disappearance of small islands, we have observed three different pathways for coalescence and one pathway, which involves a structural transformation of individual vacancy islands. These four pathways can be seen in the sequences of fig. 8.1, which are selected images taken from longer STM-movies at the indicated temperatures. We observe:

- i. Normal Coalescence:** Two islands reduce the total step length by fusing together to a more compact shape (fig. 8.1a).
- ii. Slow Coalescence:** Similar to (i), but one order of magnitude slower (fig. 8.1b). Note that the length scales in figs. 8.1 a and b are equal.
- iii. ‘Bound-Pair’ Formation:** Instead of fusing together, two vacancy islands form a bound-pair, in which they maintain a small distance along the [001]-direction with respect to one another (fig. 8.1c).
- iv. Transformation of a single Vacancy Island:** A single vacancy island transforms into two parallel ‘vacancy lines’ (fig. 8.2d). These lines are strongly correlated in position and length. We will refer to this structure as a ‘bound line pair’.

In a total of more than 10 STM-movies, each following typically 100 vacancy islands over 10 hours we observed less than 3 events of each of these four types of vacancy island evolution in real time. We have not found other coarsening phenomena at the full range of investigated temperatures from 293 K to 400 K.

The unusual variety in coalescence pathways (i-iii) results from the two configurations in which the asymmetric vacancy islands on Au(110) occur. The interior MRR of a vacancy island can be adopted in two ways, namely by removing either the *odd* or the *even* atom rows. This leads to a possible MRR phase problem of two encountering vacancy islands. If their internal MRRs are in phase, the (111)-steps appear on the same side of both vacancy islands. When the islands are out of phase, the (111)-step of one island appears on the same side as the (331)-step of the other island and *vice versa*. This leads to three essentially different configurations of two islands encountering each other.

In fig. 8.2a the internal MRRs of the two vacancy islands are in phase. In all cases where the configuration was of this type, we observed normal, i.e. rapid coalescence (pathway i), as is illustrated by fig. 8.1a. If the MRRs of the two vacancy islands were out of phase (figs. 8.2 b,c), we always observed either slow coalescence, pathway ii (fig. 8.1b), or bound-pair formation, pathway iii (fig. 8.1c). We never observed that one of the two vacancy islands switched the phase of its interior MRR in order to come into registry with the other island at temperatures below 400 K, but we did observe this switching twice at 412 K.

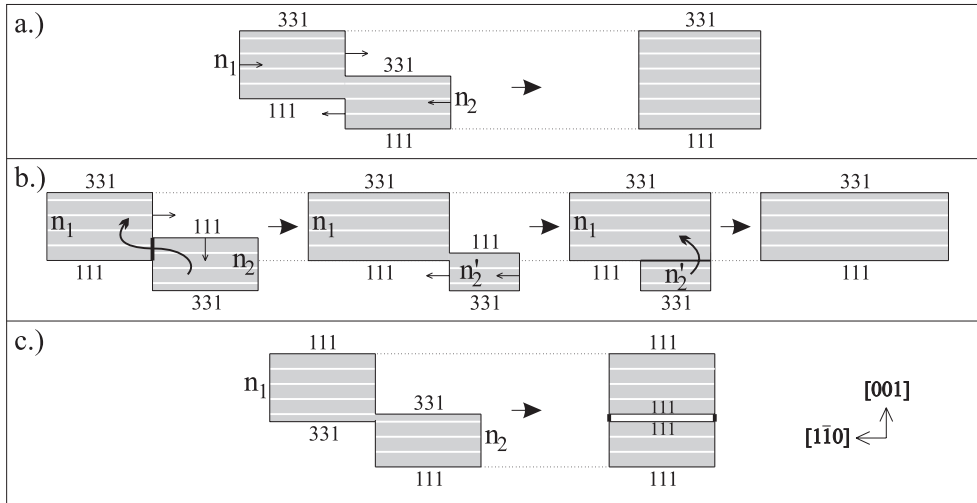


Figure 8.2: Three different configurations for the encounter of two vacancy islands: (a) matching MRRs leading to ‘normal’ coalescence (pathway i); (b,c) MRRs out of phase. In configuration (b) the outer steps are of the high-energy (331) type resulting in slow coalescence (pathway ii), while in (c) the outer steps are of the (111) type, which leads to ‘bound-pair’ formation (pathway iii). The widths of the islands along [001] are indicated by n_1 , n_2 , and n'_2 , all expressed in MRR periods of 8.16 \AA .

8.2 Microscopic Mechanisms and Resulting Time Scales

In general, the coalescence of vacancy islands is dominated by adatom and/or vacancy diffusion (see section 2.7). Due to the anisotropy of the Au(110) surface, and in particular the MRR, we have to distinguish two diffusion directions for Au atoms or vacancies on Au(110). The fast diffusion is along the $[1\bar{1}0]$ -direction and is called in-channel diffusion (see section 2.8.4). By analogy, one defines cross-channel diffusion as motion along the [001]-direction, which is expected to be a slow diffusion process. Cross-channel diffusion can take place by the hopping of atoms over the atom rows of the MRR. Another cross-channel diffusion mechanism is atom exchange. Instead of jumping over the atom row, the diffusing atom pushes another atom out of this row and simultaneously takes over the empty position. This process is called cross-channel-exchange and is calculated to be almost as fast as the cross-channel diffusion (compare the diffusion barriers in table 2.2).

8.2.1 Normal Coalescence

In the configuration of fig. 8.2a the two vacancy islands are in phase. Once the islands are connected, this connection rapidly widens. The islands slide together along the $[1\bar{1}0]$ -direction, which is indicated by the small arrows in fig. 8.2a. Note that the total

width of the structure along the $[001]$ -direction remains unchanged in this process.

For each atomic spacing the islands slide together along $[1\bar{1}0]$, they lower the energy byⁱⁱ

$$\left(E_{[1\bar{1}0]}^{111} + E_{[1\bar{1}0]}^{331}\right) = 19meV \quad (8.1)$$

This value is a measure of the high driving force for this coalescence. The process is fast, since it mainly requires in-channel diffusion, which should be the fastest diffusion on Au(110).

8.2.2 Slow Coalescence

Figure 8.2b shows the starting configuration for the slow coalescence. Since the two islands are out of phase, a domain boundary forms over the entire length, over which the islands are in contact (see thick line between the islands in fig. 8.2b). We observe that the domain boundary remains located at the narrow neck connecting the two islands during their coalescence, probably because this minimises the total domain boundary energy. In the sequence of images in fig. 8.1b one can see two different orientations of the interconnecting domain boundary. Initially, the domain boundary is oriented along the $[001]$ -direction, whereas it runs along the $[1\bar{1}0]$ -direction in a later stage (sketched schematically in fig. 8.2b).

Figure 8.3 shows a ball model that divides this coalescence into four stages, of which one can recognise three in fig. 8.1b, namely a, b, and d. The intermediate configuration of fig. 8.3c is useful for bookkeeping of energies (see below); we cannot tell whether it actually occurs between stages b and d. The two vacancy islands

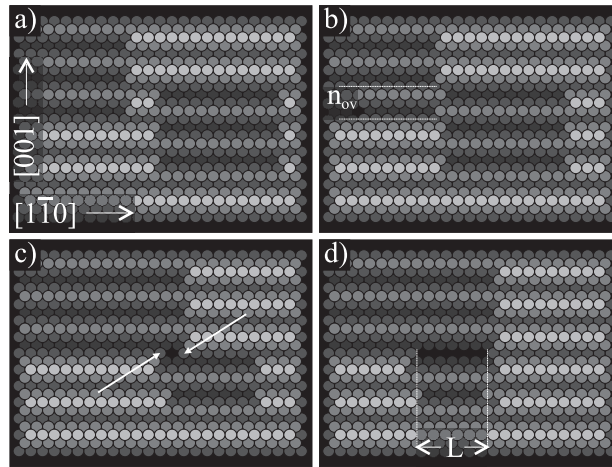


Figure 8.3: *Schematic model of different stages of the slow coalescence of two vacancy islands with non-matching MRRs, in the geometry of fig. 8.2b.*

ⁱⁱsee table 2.2

are still separated in fig. 8.3a. During their encounter they form a domain boundary, which is initially oriented along the [001]-direction and extends over the whole overlap width n_{ov} ⁱⁱⁱ (see fig. 8.3b). However, in a later stage, the domain boundary is rotated 90 degrees, forming a hollow-wall along the $[1\bar{1}0]$ -direction with length L ^{iv} (see figs. 8.3 c,d). The hollow wall can be recognised easily in the zoomed-in STM-picture of fig. 8.1b.

Before discussing the time dependence of this coalescence, we focus on the energy differences between the four configurations of fig. 8.3. The energy changes are listed in table 8.1 together with the changes in the total number of interrupted atom rows. The encounter of the islands reduces the number of interrupted atom rows by

stage	change in no. of ‘broken’ rows	energy change ΔE
a→b	$2n_{ov} = (18 - 16) = 2$	$n_{ov} \cdot (E_{[001]}^{DB} - 2E_{[001]})$
b→c	$16 - 16 = 0$	$2E_{[001]}^{DB-point} - n_{ov}E_{[001]}^{DB}$
c→d	$16 - 16 = 0$	$L \cdot (E_{[1\bar{1}0]}^{hollow} - 2E_{[1\bar{1}0]}^{111})$

Table 8.1: Changes in the number of interrupted atom rows and in total energy for the transformations between the four stages of the slow coalescence in fig. 8.3.

2 per unit of overlap width n_{ov} . This results in an energy change of

$$\Delta E_{a \rightarrow b} = n_{ov} (E_{[001]}^{DB} - 2E_{[001]}) \quad (8.2)$$

The clear preference for islands to stay in touch in this configuration (fig. 8.1b) demonstrates that $E_{[001]}^{DB} < 2E_{[001]} = 400 \pm 120$ meV per MRR period (see chapter 3 for the determination of $E_{[001]}$). Figure 8.3c shows the starting situation for the introduction of the hollow-wall domain boundary. Although the total number of interrupted atom rows is the same for configurations b and c, two of these interruptions (indicated by the arrows in fig. 8.3c) have acquired a different character in the latter configuration. They form the end points of the tiny hollow wall along $[1\bar{1}0]$, and can be regarded as ‘point domain boundaries’ along the [001]-direction, each with an energy of $E_{[001]}^{DB-point}$. Therefore we obtain

$$\Delta E_{b \rightarrow c} = 2E_{[001]}^{DB-point} - n_{ov}E_{[001]}^{DB} \quad (8.3)$$

for the energy difference between figs. 8.3b and c. Notice that the total (331)- and (111)-step lengths remain the same during this transformation (see also fig. 8.2b). As

ⁱⁱⁱ n_{ov} is expressed in units of the MRR period: 8.16 Å.

^{iv} L is expressed in atomic spacings: 2.88 Å.

we already have seen in chapter 5, the hollow-wall domain boundary energy is 1.9 ± 1.0 meV, which is lower than 2 times the (111)-step formation energy of $2 \cdot E_{[1\bar{1}0]}^{111} = 7.4 \pm 1.0$ meV. Therefore, from fig. 8.3c to fig. 8.3d, the islands further lower their combined energy by sliding together along $[1\bar{1}0]$ and replacing two (111)-step segments with one hollow wall domain boundary segment per atomic spacing.

$$\Delta E_{c \rightarrow d} = L \cdot (E_{[1\bar{1}0]}^{hollow} - 2 \cdot E_{[1\bar{1}0]}^{111}) < 0 \quad (8.4)$$

Lattice relaxation may lower the energy even further.

There are several potential reasons for the dramatic difference between the coalescence time scales for the situations of figs. 8.2a and b. From the position of the narrow neck in fig. 8.1b, one sees that the slow coalescence takes place by motion of the domain boundary (in this case from left to right), which moves hand in hand with the transport of Au vacancies between the islands (indicated by the curly arrow in fig. 8.2b). This increases the length of one of the two islands at the expense of the other (see fig. 8.4a). Let us first consider the geometry in which the domain boundary is directed along $[001]$. The amount by which the total energy changes on average when a single Au vacancy is moved over the boundary, in other words the driving force for the motion of the boundary, depends on the widths n_1 and n_2 of the two islands. If L_1 and L_2 denote the lengths of the islands along the $[1\bar{1}0]$ -direction measured in atomic spacings, mass conservation requires $\Delta L_1 \cdot n_1 = -\Delta L_2 \cdot n_2$. In the case of $n_1 = n_2$, the length changes are equal, $\Delta L_1 = -\Delta L_2$, and there is no change in total energy. As a consequence, the boundary performs an unbiased random walk. When the widths are not equal, e.g. $n_1 > n_2$ as depicted in fig. 8.4, the reduction in

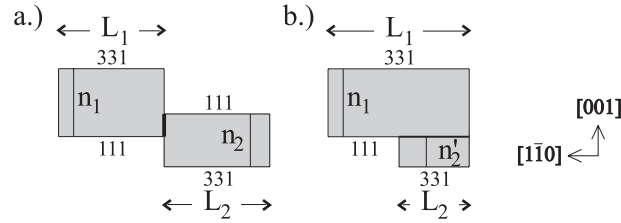


Figure 8.4: Schematic representation of two of the four stages occurring during the slow coalescence (compare figs. 8.3 b and d).

energy is proportional to $\Delta L_2 + \Delta L_1 = \Delta L_2 - \frac{n_2}{n_1} \Delta L_2$ when an area of $n_2 \Delta L_2$ is exchanged (see fig. 8.4a). Therefore the average reduction in energy per unit area^v exchanged between the islands equals

$$\frac{\Delta L_2 \left(\frac{n_1 - n_2}{n_1} \right) (E_{[1\bar{1}0]}^{111} + E_{[1\bar{1}0]}^{331})}{n_2 \Delta L_2} = \frac{n_1 - n_2}{n_1 n_2} (E_{[1\bar{1}0]}^{111} + E_{[1\bar{1}0]}^{331}) \quad (8.5)$$

^vOne unit area 'equals' two vacancies.

For differences $n_1 - n_2$ that are not too large, this leads to a much lower driving force than that of $E_{[1\bar{1}0]}^{111} + E_{[1\bar{1}0]}^{331}$ for the matching phase vacancy islands in fig. 8.2a (eq. 8.1).

Once the islands have rotated their domain boundary (see fig. 8.3c), the energy lowering per atom spacing for sliding together (from fig. 8.3c to 8.3d) is

$$2E_{[1\bar{1}0]}^{111} - E_{[1\bar{1}0]}^{hollow} \simeq 5.5meV \ll E_{[1\bar{1}0]}^{111} + E_{[1\bar{1}0]}^{331} = 19meV \quad (8.6)$$

This, again, is a much smaller driving force than in the case of normal coalescence. Once the islands have completely slid together as in fig. 8.4b, they may be able to further lower their total energy by transporting Au vacancies from the one island to the other. The average change in energy per unit area exchanged between the islands equals

$$-\frac{n_1 - n_2'}{n_1 n_2'} E_{[1\bar{1}0]}^{331} + \frac{n_1 + n_2'}{n_1 n_2'} E_{[1\bar{1}0]}^{111} - \frac{1}{n_2'} E_{[1\bar{1}0]}^{hollow} \quad (8.7)$$

Whether or not this energy change is negative, thereby driving the growth of the wider island at the expense of the narrower one, depends on the width ratio n_1/n_2' .

Kinetic limitations may further contribute to the slow coalescence times. The coalescence of islands with different phases involves substantial diffusion along the [001]-direction (cross-channel), which is known to be slow (see table 2.2). In addition, all transport between the non-matching islands only proceeds via the narrow neck. Finally, the domain boundary might act as an extra diffusion barrier for Au atoms between the connected vacancy islands, thereby slowing down the coalescence for out of phase vacancy islands even further.

8.3 Bound-Pair Formation

It is easy to see why the geometry of fig. 8.2c leads to the bound-pair formation. Figure 8.5a shows an atomic model of two vacancy islands before the pairing. Again, the MRRs are out of phase. But this time, the two islands can replace their two (331)-steps by two (111)-steps plus two short [001] domain boundaries at either end of the middle part of the island pair; compare fig. 8.5a with fig. 8.5b. The rearrangement of the two (331)-steps into two (111)-steps is illustrated in cross section in fig. 8.6. At the vertical lines, additional MRR periods can be inserted to obtain vacancy islands with larger widths. Notice that the MRRs on both sides of the vacancy island pair in fig. 8.6b remain in phase with each other, whereas the atom row (dashed) between the two islands is out of phase. This introduces a short domain boundary at each side of the island pair. For a proper estimate of the energy lowering accompanying the pairing process, one has to keep track of the total number of missing atom rows, with respect to the perfect MRR. These values are indicated next to each configuration in fig. 8.6. We estimate that, once initiated, the bound-pair formation process lowers the

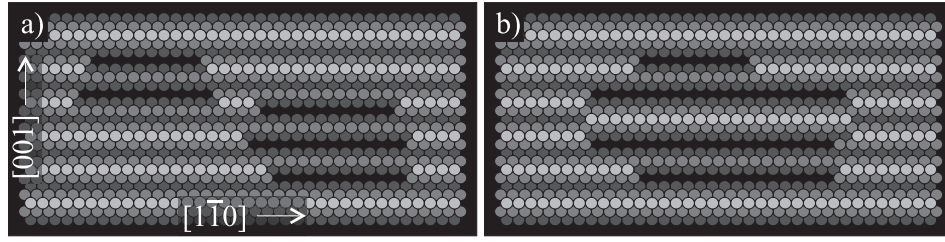


Figure 8.5: Atomic models showing the pairing of vacancy islands: (a) two vacancy islands before pairing; the outer steps are (111)-steps; (b) the vacancy pair; notice that the central atom row is out of phase with the MRR of the terrace.

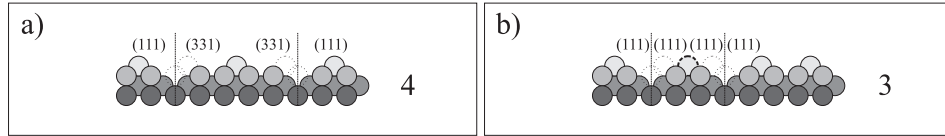


Figure 8.6: Atomic cross section models showing (a) the step configuration of two islands with two (331)- and two (111)-steps, before the pairing, and (b) the configuration with four (111)-steps after the pairing. At the vertical lines one can insert MRR unit cells to obtain vacancy islands with larger widths. The numbers to the right represent the number of missing atom rows in comparison with the flat MR reconstructed terrace.

energy of the configuration by

$$\begin{aligned}
 & 2(E_{[1\bar{1}0]}^{111} + E_{[1\bar{1}0]}^{331}) - \frac{2(n_1 + n_2)}{2(n_1 + n_2) - 1} \cdot 4E_{[1\bar{1}0]}^{111} \quad (8.8) \\
 & = 2(E_{[1\bar{1}0]}^{331} - E_{[1\bar{1}0]}^{111}) - \frac{4E_{[1\bar{1}0]}^{111}}{2(n_1 + n_2) - 1}
 \end{aligned}$$

per transformed atomic spacing. The second term in the last expression accounts for the difference in the number of missing atoms in both configurations, which is correlated to the island widths n_1 and n_2 . The smallest energy lowering occurs in the special case of $n_1 = n_2 = 1$ and is estimated to be 8.3 ± 2.8 meV per transformed atom spacing. In section 8.4, we provide evidence that the true energy lowering is even higher than this estimate, since lattice relaxations lower the total energy of the configuration in fig. 8.5b substantially with respect to $4 \cdot E_{[1\bar{1}0]}^{111}$, per atomic spacing.

8.4 ‘Bound Line Pairs’

Let us now turn to the last observed form of evolution: the transformation of individual vacancy islands into ‘bound line pairs’ (fig. 8.1d). A schematic top view of such

a ‘bound line pair’ is shown in fig. 8.7a. Figure 8.7b represents the cross sectional view along line b in fig. 8.7a. Such a ‘bound line pair’ can be regarded as 4 individual (111)-steps. Since we observe that vacancy islands with a width of 2 MRR periods

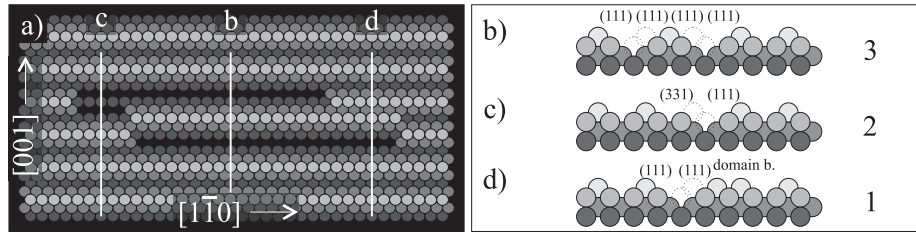


Figure 8.7: (a) Schematic model of a ‘bound line pair’ with two possible fluctuation structures. Cross sections at the position of the lines in a: (b) ‘bound line pair’; (c) asymmetric fluctuation; (d) symmetric fluctuation. The numbers to the right represent the number of missing atom rows in comparison with the flat MR reconstructed terrace.

spontaneously transform into ‘bound line pairs’ (fig. 8.1d), we can conclude that the formation energy of the ‘bound line pair’ obeys

$$E_{blp} < \frac{3}{4}(E_{[1\bar{1}0]}^{111} + E_{[1\bar{1}0]}^{331}) = 14.3 \pm 0.8 \text{ meV} \quad (8.9)$$

per atomic spacing. The factor 3/4 takes the difference of missing atoms for the two structures into account (see also fig. 8.6). Since the upper estimate $E_{blp} \leq 14.3 \text{ meV}$ is comparable to $4E_{[1\bar{1}0]}^{111} = 14.8 \pm 2.0 \text{ meV}$, one might expect the ‘bound line pairs’ to transform spontaneously into shorter, more compact island pairs. However, we have never observed such a transformation. This implies that E_{blp} is significantly lower than 14.3 meV. We propose that lattice relaxation lowers the energy of the ‘bound line pair’ substantially.

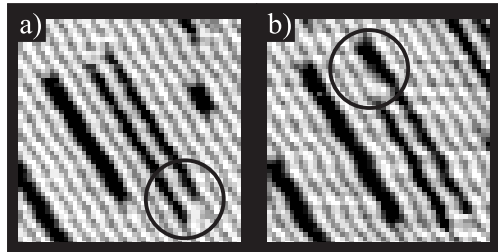


Figure 8.8: (a) ‘Bound line pair’ with an overhang (circle) in the form of a symmetric ‘vacancy line’ plus a truncated-solid-wall (cf. fig. 8.7 a,d). (b) The same ‘bound line pair’, 50 min. later, with an overhang on the other side (circle) in the form of a single asymmetric ‘vacancy line’ (cf. fig. 8.7a,c).

We can obtain a more accurate value for the energy of a 'bound line pair' from the statistics of shape fluctuations of these pairs. In order to optimise the statistics, we needed a large number of observations. Using a low ion dose (≤ 0.05 ML at room temperature) for the preparation of the vacancy islands, followed by mild annealing ($T = 343$ K; ~ 1 min.), we have been able to obtain relatively high densities of 'bound line pairs'. We have found that the relative positions and lengths of the two lines in such a pair fluctuate, which can be seen in figs. 8.8 a,b, and which is schematically sketched in fig. 8.7a. Each fluctuation involves one of the two lines sticking out into the flat terrace. This can be realised in two different ways. The most abundant fluctuation is an overhang of one of the two lines in the form of a symmetric 'vacancy line' ((111)-steps on both sides) accompanied by a truncated solid-wall (see the right part of the 'bound line pair' in fig. 8.7a, the cross section in fig. 8.7d and the STM image in fig. 8.8a). Less frequently, we observe overhangs in the form of a single, asymmetric 'vacancy line': a (111)-step plus a (331)-step (see left part of the 'bound line pair' in fig. 8.7a, the cross section in fig. 8.7b and the STM image in fig. 8.8b). Mixed overhangs were never observed: within one overhang, we only observed one structure. Therefore, we simply can measure the length of each of the overhangs, independently of whether it occurred at one side of the 'bound line pair', or the other side.

To determine the formation energies of the two types of overhangs, we measured the probability distributions of the overhang lengths, which are shown on a semi-logarithmic scale in fig. 8.9. The lengths L correspond to the total overhang length,

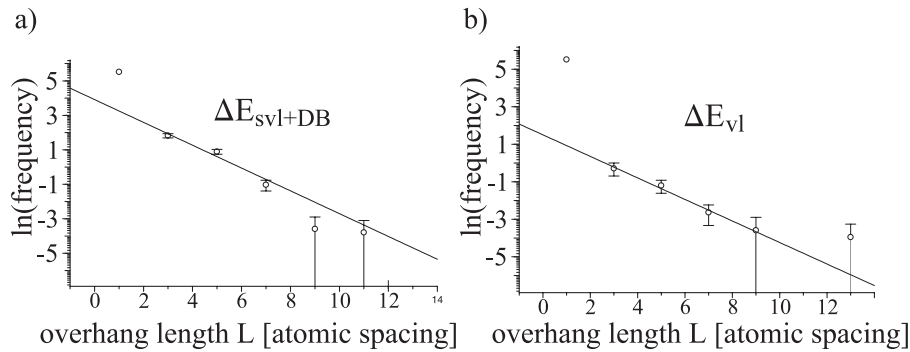


Figure 8.9: *Semi-logarithmic plots of the length distributions of the two types of overhangs at room temperature: (a) symmetric 'vacancy line' plus truncated solid-wall; (b) asymmetric 'vacancy line'. The frequencies have been corrected for the number of possible configurations, in which each total length can occur (see text).*

i.e. the sum of the overhangs at both ends of the 'vacancy line' pair.

The frequency for each length L in fig. 8.9 has been divided by the number of possible configurations for this total overhang length, which is simply $4 \cdot L$. This makes

every ‘corrected’ frequency proportional to $\exp(-L\Delta E/k_B T)$, where ΔE is the appropriate energy, as indicated in fig. 8.9. To deduce the number of possible configurations for any given total overhang length, we first consider the case of an overhang length of $L = 1$ (see fig. 8.10). If the overhang is located at the upper side of the ‘bound line pair’, one has two possibilities, the overhang being either on the left line or on the right line. The same is the case, if the overhang is located at the lower side of the ‘bound line pair’. This leads to four configurations with $L = 1$. The case of $L = 2$ has one additional, intermediate type configuration, where one atomic spacing of overhang is located at the upper side and the other at the lower side of the ‘bound line pair’. This contributes four extra configurations, since each part of the combined overhang can occur on the right and on the left line of the ‘bound line pair’. Continuing this way of counting, one obtains $4 \cdot L$ for the number of possible configurations for any L . As already mentioned, dividing the frequency at each L by the number

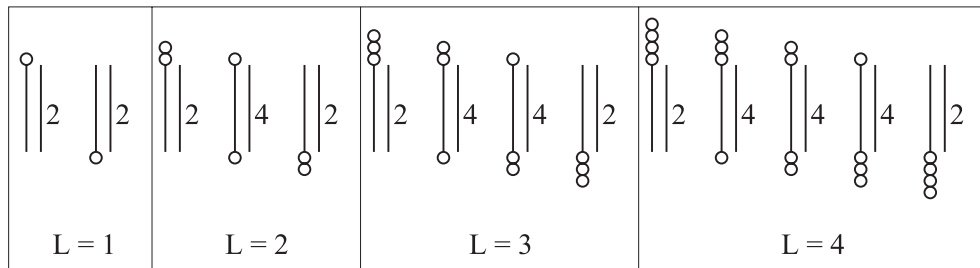


Figure 8.10: Numbers of configurations with total overhang lengths of $L = 1, 2, 3$ and 4 atomic spacings.

of configurations $4L$ makes the numbers in fig. 8.9 directly reflect the Boltzmann weight of each overhang length. The high values at $L = 1$ are an artifact: overhangs of lengths 0 and 1 could hardly be distinguished in our STM images. The fact that the points for higher L fall on a straight line, shows that the overhang energy increases linearly with the overhang length.

In order to extract formation energy values for the differences between the ‘bound line pair’ and the two overhang structures from the slopes of the distributions in fig. 8.9, we again have to account for the number of missing Au atoms per atomic spacing in each of the configurations. In comparison with the perfect MRR, the number of missing atoms per atomic spacing is 3 for a ‘bound line pair’, 2 for an asymmetric ‘vacancy line’, and 1 for a symmetric ‘vacancy line’ with an accompanying truncated solid-wall (fig. 8.7 b,c and d). Thus, we find

$$E_{svl+DB} = 1/3 E_{blp} + \Delta E_{svl+DB} \quad (8.10)$$

$$E_{vl} = 2/3 E_{blp} + \Delta E_{vl} \quad (8.11)$$

where E_{vl} and E_{svl+DB} are the formation energies of an (asymmetric) ‘vacancy line’ and of a symmetric ‘vacancy line’ plus truncated solid-wall, respectively. The energy

differences $\Delta E_{vl} = 15.0 \pm 3.0$ meV and $\Delta E_{svl+DB} = 16.8 \pm 2.5$ meV per atomic spacing have been obtained from the slopes of the two linear fits in fig. 8.9. We approximate the energy per atomic spacing of an (asymmetric) ‘vacancy line’ by^{vi}

$$E_{vl} \simeq E_{[1\bar{1}0]}^{111} + E_{[1\bar{1}0]}^{331} = 19.0 \pm 1.0 \text{ meV} \quad (8.12)$$

Combining this with eq. 8.11 we find

$$E_{blp} = 6.0 \pm 3.4 \text{ meV} \quad (8.13)$$

for the energy of a ‘bound line pair’. This is substantially lower than both the upper estimate of eq. 8.9 and the energy naively associated with the ‘bound line pair’ of $4E_{[1\bar{1}0]}^{111} = 14.8 \pm 2.0$ meV. This suggests that the ‘bound line pair’ structure undergoes a significant relaxation with respect to the simple four-step configuration. From the combination of equations 8.10 and 8.13 we find

$$E_{svl+DB} = 18.8 \pm 2.7 \text{ meV} \quad (8.14)$$

In addition, with the approximation of

$$E_{svl+DB} \simeq 2E_{[1\bar{1}0]}^{111} + E_{[1\bar{1}0]}^{tr.-solid} \quad (8.15)$$

we obtain the following rough estimate for the domain boundary energy (truncated solid-wall)

$$E_{[1\bar{1}0]}^{tr.-solid} \sim 11.4 \pm 2.9 \text{ meV} \quad (8.16)$$

8.4.1 Length Constraints on the ‘Bound Line Pairs’

We can formulate two constraints on the length of a ‘bound line pair’. The first is based on the fact that the total energy for sufficiently long bound-line pairs can be lowered, if *one* of its lines is widened by one period of the MRR, so that the island pair gets more compact. The second constraint is based on the fact that two *single* hollow walls cost less energy than a ‘bound line pair’.

First, let us estimate the maximum size of a vacancy island that should still transform into a ‘bound line pair’. Per unit of length, a ‘bound line pair’ has a deficit of 3 atoms with respect to the perfect MRR and costs $E_{blp} = 6.0$ meV. Above a certain total number of missing Au atoms, this structure is higher in formation energy than a shorter ‘bound island pair’, where *one* of the ‘vacancy lines’ is replaced by a narrow island with a width of two MRR periods (see fig. 8.6b and imagine *one* additional period of the MRR at the position of one of the two vertical lines). Per unit of length,

^{vi}This approximation is equivalent to the assumption that the formation energy of an asymmetric vacancy island is equal to that of an (asymmetric) adatom row (chapter 3 and table 2.2).

this modified structure lacks 5 atoms and we assume that it costs still 6 meV^{vii}. Due to the additional MRR period, an extra amount of energy, $2 \cdot E_{[001]} = 400$ meV, has to be ‘paid’ for the two new [001]-step segments at the sides of the wider island. If N denotes the total number of missing Au atoms, we obtain

$$\frac{N}{3}E_{blp} < \frac{N}{5}E_{blp} + 2E_{[001]} \quad (8.17)$$

as the criterion for the ‘bound line pair’ to be more stable. From this we get $N \leq 500$. In other words, the ‘bound line pair’ represents the structure with the lowest energy of all vacancy island configurations with numbers of missing Au atoms up to 500. This implies that the maximum observed length of a ‘bound line pair’ should be $500/3 \cdot 2.88 \text{ \AA} = 480 \text{ \AA}$. Figure 8.11a shows one of the longest observed ‘bound

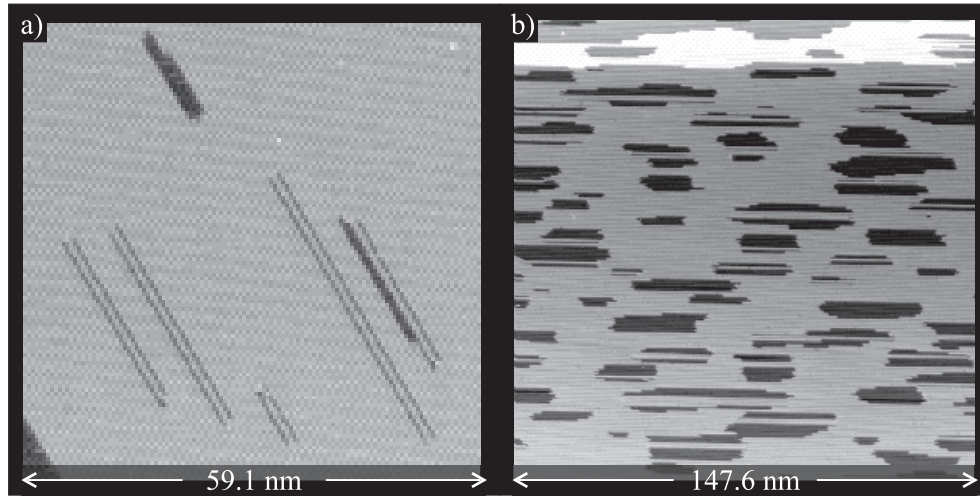


Figure 8.11: *STM images, taken at $T = 343$ K, during the evolution of a damaged Au(110)-surface: (a) containing a low density of vacancy islands, and (b) containing a high density of vacancy islands.*

line pairs’, which had a length of 397 \AA . The image represents a typical situation after the annealing of a Au(110)-surface containing a low density of vacancy islands. On the other hand, if vacancy islands contain more than $N = 500$ missing Au atoms, more compact bound-pairs form the lowest energy configurations (fig. 8.11b). They can be created by the annealing of a Au(110)-surface containing a high density of sputtering-induced vacancy islands.

We now turn to the second constraint. The energy of a ‘bound line pair’ is higher than two times the hollow-wall energy

$$E_{blp} = 6.0 \text{ meV} > 2 \cdot E_{[110]}^{hollow} = 3.8 \text{ meV} \quad (8.18)$$

^{vii}The energy of this structure is, in fact, expected to be a little higher than 6 meV.

Let us assume that when we widen the solid wall in a ‘bound line pair’ by one additional period of the MRR, the energy of this new structure equals that of two individual hollow walls. According to eq. 8.18, this should lower the energy. However, in analogy to the situation described above, the extra distance between the vacancy lines introduces two extra pieces of [001]-domain boundary, one at each end, which gives a positive contribution to the energy. Combining these two effects, we see that only for sufficiently long ‘bound line pairs’ the total energy can be lowered also by splitting the bound pair of vacancy lines into a more open structure. We obtain the following condition

$$\frac{N}{3} \cdot E_{blp} < \frac{N}{3} \cdot 2 \cdot E_{[1\bar{1}0]}^{hollow} + 2 \cdot E_{[001]}^{DB} \simeq \frac{N}{3} \cdot 2 \cdot E_{[1\bar{1}0]}^{hollow} + 2 \cdot E_{[001]} \quad (8.19)$$

where we assume that the [001] domain boundary energy can be approximated by that of a [001]-step segment, of 200 meV. Solving this equation, we find that ‘bound line pairs’ with 550 missing Au atoms should widen up. However, as we saw from eq. 8.17, for similar island sizes, we should expect the ‘bound line pairs’ to form more compact ‘bound island pair’ structures. At high temperatures, close to the deconstruction transition, the unbinding of ‘bound line pairs’ may play a role in the formation of antiphase domains in the MRR structure.

8.5 One-Dimensional Diffusion

A detailed understanding of the dominating diffusion processes on Au(110) can be obtained from the analysis of the position and length fluctuations of asymmetric vacancy lines, i.e. of vacancy islands with a width of $n = 1$, such as the vacancy line left of the ‘bound line pair’ in fig. 8.8a. When a Au atom is released from one end of the island and attaches at the other end, the island moves as a whole. As a result of many of these events, the vacancy island performs a strictly one-dimensional random walk along the $[1\bar{1}0]$ -direction. There are two possible forms of diffusion behaviour: attachment limited and diffusion limited (see section 2.7). Both are reflected in the variation of the island’s diffusion constant as a function of its length.

In the case of pure diffusion limitation, the atoms perform a free random walk inside the vacancy island. As a consequence, if an atom is emitted from one end, it has a higher probability of being caught by the same end than of reaching the other end of the island. This problem is well known as the *Classical Ruin Problem* [109] and the solution, the success rate of atoms traveling from one end to the other, is given by $1/L$ ^{viii}. Short islands should, therefore, show a higher diffusion constant than longer ones. We expect the diffusion constant to be linearly dependent on the reciprocal length of the vacancy island.

^{viii} L has to be expressed in atomic spacings along the $[1\bar{1}0]$ -direction. The frequency at which atoms are emitted at the two ends is supposed to be independent of L .

If the diffusion is attachment limited, the diffusing atoms inside the vacancy island face an additional barrier when attaching to one of the ends. In the case of extreme attachment limited diffusion, we expect the diffusion constant to be completely independent of the island length.

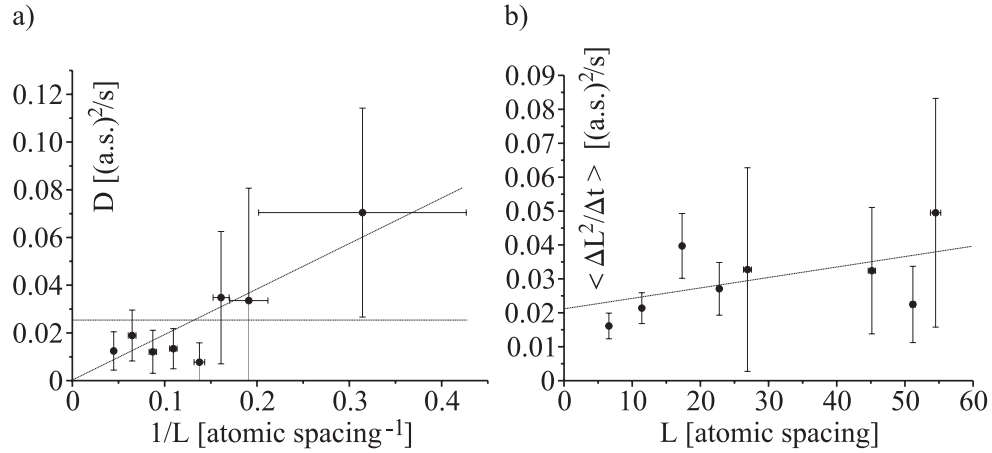


Figure 8.12: (a) Vacancy island diffusion constant as a function of the reciprocal length of the islands. (b) Variation of the mean-square length fluctuation per unit with the island length. The data have been obtained from STM-movies of single (asymmetric) vacancy lines taken at room temperature.

Figure 8.12a shows preliminary results for the diffusion constant. The error margins of the data are such that both fits (no dependence and linear dependence on the reciprocal island length) are consistent with the data, although the proportional line provides a slightly better fit. For the intermediate case of a ‘modest’ attachment barrier, we should expect D to be proportional to $1/L$ for small $1/L$ -values and to level off to a constant value for large $1/L$. Clearly, the statistics of the measurements need to be improved to interpret the data at this level.

From the length fluctuations of vacancy islands, we can obtain further information. Disregarding single vacancy diffusion [39], we recognise two different pathways for atom exchange between an island and the flat terrace. In the first case, atoms can reach or leave the vacancy island via the long sides ((331)-step and (111)-step), by cross-channel diffusion or exchange. The resulting fluctuation is expected to depend on the vacancy island length. The longer the islands are, the higher their fluctuation should be: $\langle \frac{(\Delta L)^2}{\Delta t} \rangle \sim L$. The other possibility is that atoms climb in and out at the end points of an island. There, they have to overcome a possible Ehrlich-Schwöbel barrier [36, 37, 38]. Since each island has exactly two end points, the resulting fluctuation should be length independent. If both pathways are active, i.e. the long sides and the end points, the plot of the mean-square length fluctuation versus island length should be a straight line, which does not go through the origin. The

slope should be a measure for the exchange rate at the long sides, and the offset at zero length a measure of the exchange rate at the two end points. Figure 8.12b shows the preliminary results of the fluctuation measurements. Within the larger error margins the plot is consistent with a straight line with an offset for $L = 0$. Measuring the slope and the offset at different temperatures, enables to extract the energy barriers (Ehrlich-Schwöbel barrier) involved.

The diffusion measurements presented here were preliminary. Obviously, we need more experimental data to obtain appropriate statistics.

8.6 Summary

We have seen that the coarsening of vacancy islands with broken internal symmetry proceeds via an unusual variety of pathways. We even observed the spontaneous splitting of single vacancy islands into bound pairs of islands or ‘bound line pairs’. The reason for this variety is based on the two different configurations of vacancy islands, which can adopt different phases of their internal MRR with either the *odd* or the *even* atom rows being absent. This leads to coalescence events, where the islands are either in-phase or out-of-phase. Normal coalescence is observed for the in-phase case. The out-of-phase situation takes place either via slow coalescence or via bound-pair formation. The slow-down effect can be attributed to reduced energetic driving forces, unfavourable diffusion directions and additional diffusion barriers. The pairing of two vacancy islands into a bound pair is due to the energy lowering in the transformation of two (331)-steps into two (111)-steps. The transformation of asymmetric vacancy islands into two strongly correlated ‘vacancy lines’ indicates a low formation energy of the latter structure. From the fluctuation of the single lines in such a pair with respect to one another, we determine the ‘bound line pair’ formation energy to be

$$E_{blp} = 6.0 \pm 3.4 meV \quad (8.20)$$

Since the energy of four (111)-steps, which form a ‘bound line pair’, is much higher than E_{blp}

$$E_{blp} = 6.0 \pm 3.4 meV \ll 4E_{[1\bar{1}0]}^{111} = 14.8 \pm 2.0 meV \quad (8.21)$$

we conclude that lattice relaxation must play an important role in the ‘bound line pair’ structure. The low value of the formation energy of ‘bound line pairs’ further implies that this peculiar structure forms the lowest energy configuration for vacancy islands of less than approximately 500 missing atoms. Vacancy islands with more missing Au atoms form bound-pairs of more compact islands. In both situations, all (331)-steps are effectively cancelled. The same observations further show that the asymmetric vacancy islands, containing a (331)- and a (111)-step, have been merely metastable.

In comparison with usual coalescence, where the total step length is reduced, both the bound pairs and the 'bound line pairs' introduce additional step length. In some cases, e.g. during 'bound line pair' formation, the total step length is even increased. This might play a role in catalysis, where gas adsorption can force and break the symmetry of a clean or pre-adsorbed surface.

With our new knowledge of the vacancy island structures and energies, we can speculate on the atomic structure that appears in the early stages of the deconstruction transition. This structure has to introduce disorder in the perfectly periodic MRR of a flat terrace. A 'bound line pair' would perfectly fulfill this condition. Once the temperature allows the splitting of such a 'bound line pair' into a structure with two hollow walls, we expect the surface to spontaneously generate almond-like patches in the flat terrace, in which the MRR is out of phase with the surrounding surface. The almond-like equilibrium shape of these antiphase domains can be predicted by the symmetric Wulff construction of chapter 4, with the (111)-step segment energy replaced by the hollow-wall energy.

Appendix A: Sample Preparation and Tunneling Conditions

In this work, two Au(110) samples were used. They were purchased from Surface Preparation Laboratory [110], where they were spark cut from a 5N purity single crystal ingot of Au. After spark erosion, the specimens were oriented by Laue X-ray diffraction to within 0.1° and mechanically polished in this orientation. The samples were cleaned *in situ* (in the ultrahigh vacuum setup) by cycles of Ar^+ (600 eV) ion bombardment (sputtering dose equivalent to 15 monolayers) at room temperature and annealing for 10 min at 773 K. After the first few sputter and annealing cycles a repolishing step was necessary in order to get rid of pinning and faceting due to segregation of bulk contamination. The annealing temperature was carefully chosen to be just above the reported deconstruction temperature, in order to reach sufficient mass transport perpendicular to the MRR-direction. The cleanliness of the sample was checked with Auger Electron Spectroscopy (AES) in the first stages of preparation. Later, the density of adsorbates was lower than the detection limit of the AES, and LEED was used to characterise the condition (flatness and quality of the MRR) of the sample. The sharpness of the (1x2)-spots provided an excellent measure for the mean terrace width. This protocol produced flat Au(110)-surfaces with an average terrace width up to 3000 Å along the [001]- and up to 10000 Å along the $[\bar{1}\bar{1}0]$ -direction.

Where not explicitly mentioned, all STM measurements were acquired at a sample voltage of -0.7 V and tunneling currents below 0.1 nA. Under these conditions no influence of the W tip on the Au surface was observed. In all small-scale images, the MRR was routinely resolved. In some high-resolution images, the atomic structure within the individual atomic rows could be recognised vaguely.

Summary

In this thesis scanning tunnelling microscopy observations were presented for a clean metal surface: Au(110). Due to its missing row reconstruction, Au(110) can occur in two different ‘phases’. In contrast to usual surfaces, we observed a variety of different step and island structures, all appearing on the Au(110)-surface, and all resulting directly or indirectly from the missing-row reconstruction. We used statistical mechanics to interpret the experimental data, and obtained detailed information on the dynamics and the energetics of these structures. Equipped with this knowledge, we could explain the observed structures, their shapes, their unusual variety, their relation to each other, and their temporal evolution behaviour. The high mobility of Au atoms made it impossible for us to observe the phase transitions, known as deconstruction and roughening in real space with the STM. However, based on the energetics, measured at low temperatures, we could make predictions about these two transitions.

In chapter 1 a new STM-design is presented that combines the advantages in stability and thermal drift compensation of the present microscope with the positioning freedom, which is offered by the so-called ‘Beetle’-type STM. A new architecture of the UHV-system will allow future STM measurements with better resolution, and with more versatility with respect to crystal preparation and imaging conditions.

In chapter 3 we observed an unusual, symmetric, equilibrium shape of islands on Au(110): almond-like with two sharp corners. We found that the ‘cheapest’ way to connect these islands is by means of a step network structure (*fish-scale-pattern*), which avoids the formation of both domain boundaries and high-energy steps. The network consists of ‘termination’ and ‘crossing’ sites, which allow the surface to accommodate any slope and slope variation. The dynamic behaviour of the almond-shaped islands revealed not only an unusual time dependence but showed also that each level in a multilayer island structure cannot be described independently of all other levels in the structure. Although the peculiar almond shape was predicted by an earlier theoretical treatment of Au(110), the energy values obtained by applying this theory to our data were outside the range for which the theory was valid. In chapter 4 we formulated a more appropriate approximation, as well as an exact free energy expression, and showed that the equilibrium shape should indeed be similar to that of an almond.

Chapter 5 described the formation of domain boundaries at locations of ‘termination’ and ‘crossing’ sites in the network structures at relatively low temperatures. By making use of the free energy description deduced in chapter 4, we derived the formation energy of two of the four possible types of domain boundaries. The combination of our experimentally obtained energies with theory allows us to predict the transition temperatures. These temperature values are in reasonable agreement with experimental observations. Although we observed these domain boundaries, we cannot explain the deconstruction transition on the basis of the domain boundary formation observed here. Instead, this transition requires the formation and introduction of antiphase domains into the well-ordered, missing-row reconstructed surface. In chapter 8 we observed an artificially created different structure, which exactly fulfills the antiphase domain condition. Close to the transition temperature we expect this structure to nucleate at the domain boundaries.

In chapter 6 we succeed, in the creation of vacancy islands on Au(110) with only one-fold internal symmetry (one mirror plane), in contrast with the two-fold symmetry of the surface itself (two perpendicular mirror planes). Along one direction, two oppositely located steps differ in structure and therefore also in energy; in particular, the energy of the expensive step is about four times as high as the energy of the opposite one. One naturally expects that avoiding the high-energy step would make the island shape asymmetric. However, the observed island shapes were totally symmetric. In chapter 7 we extended our free energy description of chapter 4 to the case of the asymmetric islands and deduced the condition for a symmetric contour of a crystal with asymmetric internal structure. This condition is indeed fulfilled on the Au(110)-surface. A popular method to determine the (free) energy ratios of steps or facets is to measure the ratios of their distances to the center of the island or crystal. The two-dimensional islands, observed here, are the first example for the failure of this concept. Analysing the outer contour of these vacancy islands, one would come to the incorrect result that the step energies of the two oppositely located steps are equal! Symmetrically shaped crystals do not necessarily exhibit a symmetric internal structure.

We further observed in chapter 8 that the vacancy islands on Au(110) evolve in time via a variety of pathways. This stands in contradiction to usual observation and is found to be a consequence of the broken structural symmetry. The time evolution of vacancy islands on surfaces occurs via diffusion; an island can move as a whole as atoms are transported from one step edge to another. The total energy of two encountering islands is lowered, if they fuse together and form a new, larger island. This is because of the reduction in total step length. In contrast with this, we found that vacancy islands on Au(110) group in pairs. Sometimes the total step length is even increased during this pairing process. This unusual behavior is a consequence of a structural reconfiguration. The pairing allows two higher-energy steps (one for each island) to transform into two ‘cheaper’ steps. But this transformation keeps the two islands from fusing together to form a compact structure. Before reaching the

state of a pair, the islands exhibited an unusual variety of island-island encounters, which was again a consequence of the broken structural symmetry of the islands.

We found that the lowest-energy vacancy pair, a so-called *bound line pair* allows the surface to introduce antiphase domains in the otherwise perfectly, missing-row reconstructed, flat terrace. Therefore, we speculate that this particular structure plays an important role in the deconstruction transition. Based on the energies involved, we expect also these antiphase domains to adopt an almond-like shape.

In table 8.2 all energy values obtained for Au(110) are summarised. Comparing

structure or parameter	energy or temperature	ref.	method
single atom row	$E_{[1\bar{1}0]}^{331} + E_{[1\bar{1}0]}^{111} = 19 \text{ meV}^i$	[70]	STM
(111)-step	$E_{[1\bar{1}0]}^{111} = 1.8 \text{ meV}^i$	[71]	EAM
(111)-step	$E_{[1\bar{1}0]}^{111} = 3.7 \pm 0.5 \text{ meV}^i$	thesis	STM
(331)-step	$E_{[1\bar{1}0]}^{331} = 9.5 \text{ meV}^i$	[71]	EAM
(331)-step	$E_{[1\bar{1}0]}^{331} = 15.3 \pm 1.5 \text{ meV}^i$	thesis	STM
[001]-step	$E_{[001]} = 200 \pm 60 \text{ meV}^{ii}$	thesis	STM
hollow wall	$E_{[1\bar{1}0]}^{\text{hollow}} = 1.9 \pm 1.0 \text{ meV}^i$	thesis	STM
solid wall	$E_{[1\bar{1}0]}^{\text{solid}} = 1.5 \pm 2.0 \text{ meV}^i$	thesis	STM
tr. solid wall	$E_{[1\bar{1}0]}^{\text{tr.-solid}} = 11.4 \pm 2.9 \text{ meV}^i$	thesis	STM
bound line pair	$E_{blp} = 6.0 \pm 3.4 \text{ meV}^i$	thesis	STM
deconstruction	$T_d \simeq [650, 765] \text{ K}$	[72]	LEED
deconstruction	$T_d \simeq [596, 667] \text{ K}$	thesis	STM+theo.
roughening	$T_r \simeq [700, 815] \text{ K}$	[64]	LEED
roughening	$T_r \simeq [726, 812] \text{ K}$	thesis	STM+theo.

Table 8.2: *Characteristic quantities for Au(110). ‘Thesis’ stands for values obtained in this thesis, and EAM for Embedded Atom Model calculation. The energies are counted (i): per atomic spacing along the $[1\bar{1}0]$ -direction, and (ii): per MRR period along the $[001]$ -direction.*

our experimentally obtained values with those from theory or from other experiments, we find that all values stand in reasonable agreement.

This thesis clearly demonstrates the power of the STM: atomic scale objects and structures can be studied and their energetics and dynamics can be quantified. In our case, this enables detailed predictions about phase transitions (deconstruction and roughening) as well as the important structures, which are expected to be involved, even though the high atom mobility prevents us from studying these transitions directly. The quantitative information obtained on the atomic scale with the

STM allows one to interpret and predict all aspects of the surface morphology and its temperature dependence.

Samenvatting voor de leek

De afgelopen vier jaar heb ik onderzoek verricht aan de atomaire verschijningsvormen van metaaloppervlakken.

De afstand tussen twee buuratomen in een metaal is zeer klein: ongeveer 0.3 nanometer. Hoe klein dit is, wordt geïllustreerd door het volgende gedachtenexperiment: in een meter passen duizend millimeter; als men deze millimeter in duizend even grote stukken deelt, krijgt men micrometers; deelt men nu deze micrometer opnieuw in duizend even grote stukken, dan krijgt men nanometers; de afstand tussen twee metaalatomen is ongeveer gelijk aan eenderde van een nanometer.

Aangezien de atomaire afstanden met lichtmicroscopie niet te onderscheiden zijn, is er op deze schaal een alternatieve vorm van beeldvorming nodig. Om atomaire structuren te bekijken, heb ik met een speciale microscoop gewerkt, een zogenaamde ‘rastertunnelmicroscop’. De afbeelding wordt met behulp van een heel scherp metaalen naaldje verkregen, dat in het ideale geval zo scherp is, dat er zich maar één atoom aan het eind van de naald bevindt. Deze naald wordt op gecontroleerde manier uiterst dicht bij het te onderzoeken metaaloppervlak gebracht (circa drie atoomafstanden). Hoewel het naaldje en het oppervlak elkaar niet raken, loopt er toch een elektronenstroom wanneer er een spanning tussen het naaldje en het metaaloppervlak wordt aangelegd. Dit effect noemt men ook wel ‘tunneleffect’, omdat elektronen van het ene metaal naar het andere metaal ‘tunnelen’ (overspringen). De stroomsterkte is extreem gevoelig voor de afstand tussen de twee metalen. Bij beweging van het naaldje langs het metaaloppervlak daalt, vanwege de toegenomen afstand, de tunnelstroom telkens wanneer het naaldje zich tussen twee atomen bevindt en stijgt deze wanneer het naaldje boven een atoom staat. Zo wordt het mogelijk atomen ‘zichtbaar’ te maken. In de praktijk wordt meestal de hoogte van het naaldje voortdurend aangepast, om de stroom constant te houden. In dit geval ‘tast’ het naaldje het oppervlak af.

Dit proefschrift beschrijft experimenten die op een speciaal georiënteerd oppervlak van een goudkristal zijn uitgevoerd. Een kristal kenmerkt zich door zijn perfecte periodiciteit. Alle atomen bevinden zich op volstrekt regelmatige posities. Vereenvoudigd zijn de atomen met kogels te vergelijken. Als we voldoende kogels in een bak gooien om de bodem helemaal te bedekken, dan ordenen de kogels zich in een regelmatige laag met een hexagonale structuur. Bij toevoeging van de volgende

verzameling kogels vormt zich een tweede hexagonale laag boven op de eerste. Als we een onvolledige laag toevoegen, en deze zo compact mogelijk samen brengen, vormt zich een tweedimensionaal eiland. De rand van een dergelijk eiland noemt men 'stap'. Omdat de atomen van de rand bindingspartners missen, moet men voor het creëren van een stap op een kristaloppervlak (potentiële) energie betalen.

Laten wij ons nu richten op een enkel atoom (kogel) op een metaaloppervlak. Atomen trillen voortdurend ten opzichte van hun evenwichtsposities. Hoe hoger de temperatuur is, des te sterker is deze trilbeweging. Als de temperatuur voldoende hoog is, springt het atoom daardoor vaak naar een nieuwe evenwichtspositie. Op deze manier voert het atoom een 'dronkenmans-wandeling' uit over het oppervlak, totdat het een stap ontmoet, waar het dan meestal vaster gebonden wordt. Bij voldoende hoge temperatuur kan het atoom zich langs de stap bewegen. Bij nog hogere temperatuur is het ook mogelijk dat atomen weer van de stappen loskomen. Zo kunnen eilanden en stappen op een oppervlak met elkaar atomen uitwisselen. Metaaloppervlakken zijn daarom in het algemeen niet statisch.

Bij voldoende mobiliteit (voldoende hoge temperatuur) zal de algemene structuur van het oppervlak, alsmede die van de eilanden, de vorm met laagste energie aannemen. Dit is de drijfveer voor het ontstaan van tweedimensionaal compacte eilanden op een oppervlak, want daardoor wordt de totale staplengte zo klein mogelijk gehouden. Door het metaaloppervlak met snelle gasdeeltjes te beschadigen, kunnen we het oppervlak opzettelijk in een ongeordende toestand met hoge energie brengen. De atomen zullen dan in hun beweging de toestand met de laagste energie herstellen. De in dit proefschrift beschreven experimenten zijn er deels op gericht om het herstelproces van een oppervlak via deze atomaire beweging gade te slaan.

Tot mijn grote verrassing heb ik op het goudoppervlak een verscheidenheid aan eilandstructuren en een verscheidenheid aan herstelprocessen waargenomen. Door zorgvuldig de structuren te tellen die tijdens het herstelproces optreden, konden de energieën van de stappen op het goudoppervlak worden bepaald. De combinatie van deze stapenergieën met deels zelf ontwikkelde theoretische modellen resulteert in een bijna volledige beschrijving van dit oppervlak, waarmee alle waargenomen structuren kunnen worden verklaard.

Tenslotte rest nog de belangrijke vraag: Wat is het nut van dit werk? Het hier beschreven onderzoek is van uitsluitend fundamenteel karakter. Echter wordt dit type kennis in toenemende mate belangrijk voor toepassing in vakgebieden zoals katalyse, micro-elektronica, kristalgroei en wrijving, waar een steeds grotere graad van verfijning wordt vereist en in de nabije toekomst het niveau wordt bereikt van technologie op de atomaire schaal: nanotechnologie.

Nawoord

Het tot stand komen van een proefschrift is te vergelijken met het oprichten van een bouwwerk. Er moeten precies op de juiste plek en op het juiste tijdstip heel veel stenen op elkaar gezet worden. De inspanningen van Siebe van Albada, Koen Schoots en Dennis Quist, drie extra bouwvakkers in de vorm van drie studenten, die onder mijn directe begeleiding hebben meegewerkt, waren onmisbaar. Sommige delen van dit proefschrift zullen ze dan ook bekend voorkomen.

Maar behalve het directe werk, is er ook heel belangrijk werk achter de schermen nodig. Zo moeten b.v. de juiste discussies gevoerd, stenen uitgezocht, ingekocht, de logistiek verzorgd en langs dat gebouw omhoog naar hun plek getransporteerd worden. Deze directe of indirecte, wetenschappelijke of niet-wetenschappelijke bijdragen zijn alle op hun manier heel belangrijk geweest. Zo krijgt dan ieder ‘steentje’ ook zijn plek in dit proefschrift:

Marcelo Ackermann, Wim Barsingerhorn, Mark Brongersma, Wim Brouwer, Barry Cats-Houdijk, Ille Cerjak, Jürgen Chrost, Bert Crama, Ewie de Kuyper, Steven de Vries, Martin Dienwiebel, Jos Disselhorst, Helen Fraser, Arjen Geluk, Dick Glas-tra van Loon, Jenny Heimberg, Bas Hendriksen, Marcel Hesselberth, Mischa Hoogeman, Willem Jan Huisman, Martin Jak, Marcel Janson, Dionne Klein, Mark Klik, Chris Konstapel, René Koper, Fred Kranenburg, Arie Kuijt, Ruud Kuyvenhoven, Pradeep Namboodiri, Henk Neerings Riet Nieuwenhuijzen, Ben Okhuysen, Tjerk Oosterkamp, Matthew Osbourn, Joost Peters, Peter Rasmussen, Bernd Riedmüller, Fred Robbers, Jaap Sanders, Gregg Siegal, Amalia Stamouli, Matthys Suijlen, Hans ter Horst, Dana Tomuta, Marc van de Burg, Jan van der Elsen, Jan van der Linden, Jan van Elst, Raoul van Gastel, Martin van Hecke, Ellie van Rijsewijk-Salman, Graziëlla van Velzen, Gertjan Verhoeven, Jan Verhoeven, Willem Versluijs, Ton Vijftigschild, Frank Waalboer, Paul Wessels, Jan Zandvliet, Hans Zeijlemaker, Michel Zwanenburg, Ruud Zweistra.

Omdat de effectiviteit van werken duidelijk is gecorreleerd met de persoonlijke omgeving, ben ik alle vrienden en kennissen erkentelijk, die eraan hebben bijgedragen dat ik mij hier in Nederland echt thuis voel.

Als laatste, maar zeker niet minste, wil ik mijn vriendin Audrey, haar ouders, Annette en Pierre, en mijn familie, Thilo, Anna-Mina, Kerstin, Pogo, Frieda, Gerlinde en Ernst, bedanken voor alle steun en belangstelling.

Curriculum Vitae

Marcel Joachim Rost

born in Garmisch-Partenkirchen (Germany) on October 30, 1968

After finishing my secondary education at the Gymnasium Thusneldastrasse, Köln-Deutz (Germany), I joined the Rheinisch-Friederich-Wilhelms University, Bonn (Germany) in 1990 as a first-year physics student. During the time of my diploma project I was employed at the Forschungszentrum Jülich (Germany) and worked in the research group of Prof. Dr. G. Comsa under direct supervision of Priv. Doz. Dr. Th. Michely at the IGV (Institut für Grenzflächenforschung und Vakuumphysik). The work concerned a vibrational analysis of an STM, which led to the design and construction of an improved microscope. The capability of this new STM was demonstrated by studies on the energetics, reconstruction and homoepitaxial deposition of Ir(111). The continuation of this work as a research assistant, after graduation in 1996, resulted in a patent with the title: 'micro manipulator'. In March 1997 I began working as a Ph.D. student in the group of Prof. dr. J. W. M. Frenken at the FOM Institute for Atomic and Molecular Physics (AMOLF), Amsterdam (The Netherlands). In 1998 the group moved to the Kamerlingh Onnes Laboratory at the University of Leiden (The Netherlands). This thesis presents part of the work, which has been performed during my Ph.D. time. Additional work on grain growth in polycrystalline gold, is currently under preparation for publication. During my Ph.D. period I supervised three undergraduate students, Siebe van Albada, Koen Schoots, and Dennis Quist, which resulted in two publications and one student award at a meeting of the Dutch Vacuum Society. In Leiden, I have assisted also in practical training of second-year students, and I have constructed a new student experiment. During the period of my Ph.D. research, I have been employed by 'Nederlandse Organisatie voor Wetenschappelijk Onderzoek' (NWO).

Bibliography

- [1] R. Young, J. Ward and F. Scire; *Rev. Sci. Instr.* **43**, 999 (1972)
- [2] G. Binnig, H. Rohrer, Ch. Gerber and E. Weibel; *Phys. Rev. Lett.* **49**, 57 (1982)
- [3] G. Binnig and H. Rohrer; *IBM J. Res. Develop.* **30**, 4 (1986)
- [4] C.J. Chen; *Introduction to Scanning Tunneling Microscopy*, Oxford University Press, New York (1993)
- [5] K. Besocke; *Surf. Sci.* **181**, 145 (1987)
- [6] J. Frohn, J.F. Wolf, K. Besocke and M. Teske; *Rev. Sci. Instr.* **60**, 1200 (1989)
- [7] M.J. Rost; Diplomarbeit, Rheinischischen-Friedrich-Wilhelms-Universität Bonn (1996)
- [8] T. Michely, M. Rost and M. Kaiser; *Micro manipulator for moving flat objects in any direction and scanning probe microscope for research of huge immobile objects at any location.*, Patent PT. 0.1899 Forschungszentrum Juelich
- [9] L. Kuipers, R.W.M. Loos, H. Neerings, J. ter Horst, G.J. Ruwiel, A.P. de Jongh and J.W.M. Frenken; *Rev. Sci. Instr.* **66**, 4557 (1995)
- [10] M.S. Hoogeman, D. Glastra van Loon, R.W.M. Loos, H.G. Ficke, E. de Haas, J.J. van der Linden, H. Zijlemaker, L. Kuipers, M.F. Chang, M.A.J. Klik and J.W.M. Frenken; *Rev. Sci. Instr.* **69**, 2072 (1998)
- [11] T. Michely, M. Kaiser and M. J. Rost; *Rev. Sci. Instr.* **71**, 4461 (2000)
- [12] S. Behler, M.K. Rose, D.F. Ogletree and Miquel Salmeron; *Rev. Sci. Instr.* **68**, 124 (1996)
- [13] L. Kuipers, M.S. Hoogeman and J.W.M. Frenken; *Phys. Rev. B* **52**, 11387 (1995)
- [14] E. de Haas, W. Barsingerhorn and J.F. van der Veen; *Rev. Sci. Instr.* **67**, 1930 (1996)
- [15] W. Kossel; *Nachr. Ges. Wis. Göttingen* 135 (1927)
- [16] G. Wulff; *Z. Krist.* **34**, 449 (1901)
- [17] C. Herring; *Phys. Rev.* **82**, 87 (1951)
- [18] P. Stolze; *J. Phys. Condens. Mat.* **6**, 9495 (1994)
- [19] L.D. Landau and E.M. Lifshitz; *Statistical Mechanics* Vol.I, (Pergamon, Oxford) (1980)
- [20] A.F. Andreev; *Zh. Eksp. Teor. Fiz.* **80**, 2042 (1981) [*Sov. Phys. JETP* **53**, 1063 (1981)]
- [21] T. Michely and G. Comsa; *Surf. Sci.* **256**, 217 (1991)
- [22] M.J. Rost, T. Michely and G. Comsa; *Phys. Rev. B* **57**, 1992 (1998)
- [23] H.P. Bonzel and A. Emundts; *Phys. Rev. Lett.* **84**, 5804 (2000)
- [24] G. Schulze Icking-Konert, M. Giesen and H. Ibach; *Phys. Rev. Lett.* **83**, 3880 (1999)
- [25] S.T. Chui and J.D. Weeks; *Phys. Rev. B* **14**, 4978 (1976)
- [26] M.S. Hoogeman, M.A.J. Klik, D.C. Schlößer, L. Kuipers and J.W.M. Frenken; *Surf. Sci.* **448**, 142 (2000)
- [27] J.M. Kosterlitz and D.J. Thouless; *J. Phys. C* **6**, 1181 (1973)

- [28] S. Balibar and B. Castaing; Surf. Sci. Rep. **5**, 87 (1985)
- [29] E. Luijten, H. van Beijeren and H.W.J. Blöte; Phys. Rev. Lett. **73**, 456 (1994)
- [30] P. Nozières; in: Solids Far From Equilibrium, Ed. C. Godrèche (Cambridge Univ. Press, 1992) p.1
- [31] J. Lapujoulade; Surf. Sci. Rep. **20**, 191 (1994)
- [32] L.D. Landau and E.M. Lifschitz; Theory Of Elasticity, Vol. 7, (Pergamon Press, 1959)
- [33] K.H. Lau and W. Kohn; Surf. Sci. **65**, 607 (1977)
- [34] V.I. Marchenko and A.Ya. Parashin; Sov. Phys. JETP **52**, 129 (1980)
- [35] L.E. Shilkrot and D.J. Srolovitz; Phys. Rev. B **53**, 11120 (1996)
- [36] G. Ehrlich and F.G. Hudda; J. Chem. Phys. **44**, 1039 (1966)
- [37] R. Schwoebel; J. Appl. Phys. **37**, 3682 (1966)
- [38] R. Schwoebel; J. Appl. Phys. **40**, 614 (1969)
- [39] R. van Gastel, E. Somfai, S.B. van Albada, W. van Saarloos and J.W.M. Frenken; Phys. Rev. Lett. **86**, 1562 (2001)
- [40] J.B. Hannon, C. Klüncker, M. Giesen, H. Ibach, N.C. Bartelt and J.C. Hamilton; Phys. Rev. Lett. **79**, 2506 (1997)
- [41] T. Flores, S. Junghans and M. Wuttig; Surf. Sci. **371**, 1 (1997)
- [42] T. Klas, R. Fink, R. Platzer, J. Voigt, R. Wesche and G. Schatz; Europhys. Lett. **7**, 151 (1988)
- [43] W. Ostwald; Z. Phys. Chem. (Leipzig) **34**, 495 (1900)
- [44] D.C. Schlößer, K. Morgenstern, L.K. Verhij, G. Rosenfeld, F. Besenbacher and G. Comsa; Surf. Sci. **465**, 19 (2000)
- [45] M. Eßer, K. Morgenstern, G. Rosenfeld and G. Comsa; Surf. Sci. **404**, 341 (1998)
- [46] W.W. Pai, A.K. Swan, Z. Zhang and J.W. Wendelken; Phys. Rev. Lett. **79**, 3210 (1997)
- [47] J.-M. Wen, J.W. Evans, M.C. Bartelt, J.W. Burnett and P.A. Thiel; Phys. Rev. Lett. **76**, 652 (1996)
- [48] G. Rosenfeld, K.Morgenstern, M. Eßer and G. Comsa; Appl. Phys. **69**, 489 (1999)
- [49] G. Rosenfeld, K.Morgenstern and G. Comsa; in *Surface Diffusion: Atomistic and Collective Processes*, edited by M.C. Tringides (Plenum Press, New York, 1997) p. 361
- [50] K. Morgenstern, G. Rosenfeld and G. Comsa; Phys. Rev. Lett. **76**, 2113 (1996)
- [51] M.Z. Allmang, L.C. Feldman and M.H. Grabow; Surf. Sci. Rep. **16** 377 (1992)
- [52] K. Morgenstern, G. Rosenfeld, E. Lægsgaard, F. Besenbacher and G. Comsa; Phys. Rev. Lett. **80**, 556 (1998)
- [53] The STM image was kindly provided by R. van Gastel. The Cu(001)-surface was imaged in the early stages of sputter-cleaning and annealing.
- [54] J.R. Noonan and H.L. Davis; J. Vac. Sci. Technol. **16**, 587 (1978)
- [55] W. Moritz and D. Wolf; Surf. Sci. **88**, L29 (1979)
- [56] M. Garofalo, E. Tosatti and F. Ercolessi; Surf. Sci. **188**, 321 (1987)
- [57] D. Wolf, H. Jagodzinski and W. Moritz; Surf. Sci. **77**, 283 (1978)
- [58] P. Bak; Solid State Commun. **32**, 581 (1979)
- [59] J.C. Campuzano, M.S. Foster, G. Jennings, R.F. Willis and W. Unertl; Phys. Rev. Lett. **54**, 2684 (1985)
- [60] J. Villain and I. Vilfan; Surf. Sci. **199**, 165 (1988)
- [61] I. Vilfan and J. Villain; Surf. Sci. **257**, 368 (1991)
- [62] M. den Nijs; Phys. Rev. Lett. **66**, 907 (1991)

- [63] J. Sprösser, B. Salanon and J. Lapujoulade; *Europhys. Lett.* **16**, 283 (1991)
- [64] U. Romahn, P. von Blanckenhagen, C. Kroll and W. Göpel; *Phys. Rev. B* **47**, 12840 (1993), *and references therein*
- [65] G. Mazzeo, G. Jug, A.C. Levi and E. Tossati; *Surf. Sci.* **273**, 237 (1992)
- [66] L. Barbier, B. Salanon and J. Sprösser; *Surf. Rev. and Lett.* **1**, 75 (1994)
- [67] M. Sturmat, R. Koch and K.H. Rieder; *Phys. Rev. Lett.* **77**, 5071 (1996)
- [68] M.J. Rost and J.W.M. Frenken; *Phys. Rev. Lett.* **87**, 039603 (2001)
- [69] T.R. Linderoth, S. Horch, L.Petersen, S. Helveg, E. Lægsgaard, I. Stensgaard and F. Besenbacher; *Phys. Rev. Lett.* **82**, 1494 (1999)
- [70] M.S. Hoogeman, L. Kuipers, D.C. Schlößer and J.W.M. Frenken; *Surf. Sci.* **447**, 25 (2000)
- [71] L.D. Roelofs, S.M. Foiles, M.S. Daw and M.I. Baskes; *Surf. Sci.* **234**, 63 (1990)
- [72] range of reported T_d values: see e.g. [55, 59, 82]
- [73] F. Montalenti and R. Ferrando; *Surf. Sci.* **433**, 445 (1999)
- [74] See e.g. C. Herring in *Structure and Properties of Solid Surfaces*, edited by R. Gomer and C.S. Smith (University of Chicago Press, Chicago, 1953), p. 5; I.V. Markov, *Crystal Growth for Beginners* (World Scientific, Singapore, 1995) p. 1-41
- [75] W.K. Burton, N. Cabrera and F.C. Frank; *Trans. R. Soc. A* **243**, 299 (1951)
- [76] J.E. Avron, H. van Beijeren, L.S. Schulman and R.K.P. Zia; *J. Phys. A: Math. Gen.* **15**, L81 (1982)
- [77] H. van Beijeren and I. Nolden; in *Structure and Dynamics of Surfaces II*, edited by W. Schommers, P. v. Blanckenhagen, *Topics in Current Physics 2*, Springer, (1986) p. 259
- [78] E. Carlon and H. van Beijeren; *Phys. Rev. Lett.* **76**, 4191 (1996)
- [79] J.K.Gimzewski, R. Berndt and R.R. Schlitter; *Phys. Rev. B* **45**, 6844 (1992)
- [80] B.S. Swartzentruber, Y.-W. Mo, R. Kariotis, M.G. Lagally and M.B. Webb; *Phys. Rev. Lett.* **65**, 1913 (1990)
- [81] M.J. Rost, R. van Gastel and J.W.M. Frenken; *Phys. Rev. Lett.* **84**, 1966 (2000)
- [82] E.G. McRae, T.M. Buck, R.A. Malic and G.H. Wheatley; *Phys. Rev. B* **36**, 2341 (1987)
- [83] K. Morgenstern, E. Lægsgaard, I. Stensgaard and F. Besenbacher; *Phys. Rev. Lett.* **83**, 1613 (1999)
- [84] P. Hanesch and E. Bertel; *Phys. Rev. Lett.* **79**, 1523 (1997)
- [85] J. Tersoff; *Phys. Rev. Lett.* **80**, 2018 (1998)
- [86] E. Bertel, K. Swamy and P. Hanesch; *Phys. Rev. Lett.* **80**, 2019 (1998)
- [87] K. Swamy, E. Bertel and I. Vilfan; *Surf. Sci.* **425**, L369 (1999)
- [88] T. Gritsch, D. Coulman, R.J. Behm and G. Ertl; *Phys. Rev. Lett.* **63**, 1086 (1989)
- [89] L. Österlund, P.B. Rasmussen, P. Thostrup, E. Lægsgaard, I. Stensgaard and F. Besenbacher; *Phys. Rev. Lett.* **86**, 460 (2001)
- [90] M.J. Rost, S.B. van Albada and J.W.M. Frenken; *Phys. Rev. Lett.* **86**, 5938 (2001)
- [91] C. Rottman and M. Wortis; *Phys. Rev. B* **24**, 6274 (1981)
- [92] R.K.P. Zia and J.E. Avron; *Phys. Rev. B* **25**, 2042 (1985)
- [93] G. Gallavotti; *Commun. Math. Phys.* **27**, 103 (1972)
- [94] D.B. Abraham and P. Reed; *Phys. Rev. Lett.* **33**, 377 (1974)
- [95] D.B. Abraham and P. Reed; *Commun. Math. Phys.* **49**, 35 (1976)
- [96] M. Aizenmann; *Commun. Math. Phys.* **73**, 83 (1980)

- [97] D.T. Keane, P.A. Bancel, J.L. Jordan-Sweet, G.A. Held, A. Mak and R.J. Birgeneau; *Surf. Sci.* **250**, 8 (1991)
- [98] M. Newman and G. Barkema; *Monte Carlo Methods in Statistical Physics* (Oxford University Press) (1999)
- [99] L. Onsager, *Phys. Rev.* **65**, 117 (1944)
- [100] L. Balents and Mehran Kardar; *Phys. Rev. B* **46**, 16031 (1992)
- [101] I.K. Robinson, E. Vlieg and K. Kern; *Phys. Rev. Lett.* **63**, 2578 (1989)
- [102] M.S. Hoogeman, M.A.J. Klik, D.C. Schlößer, L. Kuipers and J.W.M. Frenken; *Phys. Rev. Lett.* **82**, 1728 (1999)
- [103] S.B. van Albada, M.J. Rost and J.W.M. Frenken; *Phys. Rev. B* submitted
- [104] I. Vilfan; *Surf. Sci.* **350**, 329 (1996)
- [105] private communication with I. Vilfan: the term $\frac{1}{\sin(\Theta)}$ in ref. [104] has to be $\frac{1}{\sin^2(\Theta)}$
- [106] D.C. Schlößer, L.K. Verhij, G. Rosenfeld and G. Comsa; *Phys. Rev. Lett.* **82**, 3843 (1999)
- [107] S. Günther, A. Hitzke and R.J. Behm; *Surf. Sci. and Lett.* **4**, 1103 (1997)
- [108] K. Rommelse and M. den Nijs; *Phys. Rev. Lett.* **59**, 2578 (1987)
- [109] W. Feller, *An introduction to probability theory and its applications*, 3rd ed. (Wiley & Sons, New York) Vol.I (1968)
- [110] R.J.I.M. Koper: <http://www.surface-prep-lab.com>